UNIVERSIDADE
BEIRA INTERIOR

Development of a minicircular DNA vaccine against COVID-19

Cathy Lopes Ventura

Dissertação para obtenção do Grau de Mestre em
Ciências Biomédicas
2º ciclo de estudos

Orientadora: Profª. Doutora Ângela Maria Almeida de Sousa
Coorientadora: Profª. Doutora Diana Rita Barata Costa

outubro de 2022

Declaração de Integridade

Eu, Cathy Lopes Ventura, que abaixo assino, estudante com o número de inscrição M10877 de/o Ciências Biomédicas da Faculdade Ciências da Saúde, declaro ter desenvolvido o presente trabalho e elaborado o presente texto em total consonância com o **Código de Integridades da Universidade da Beira Interior**.

Mais concretamente afirmo não ter incorrido em qualquer das variedades de Fraude Académica, e que aqui declaro conhecer, que em particular atendi à exigida referenciação de frases, extratos, imagens e outras formas de trabalho intelectual, e assumindo assim na íntegra as responsabilidades da autoria.

Universidade da Beira Interior, Covilhã 07 / 10 / 2022

Cathy Lopes Ventura

(assinatura conforme Cartão de Cidadão ou preferencialmente
assinatura digital no documento original se naquele mesmo formato)

Agradecimentos

Mais uma etapa concluída. A realização desta dissertação de mestrado trouxe muitos pontos positivos que vou levar para a vida pessoal e profissional, tais como força de vontade, persistência e foco nas tarefas a desempenhar. Foi um caminho longo, com altos e baixos, risos e frustrações. Todo o trabalho desempenhado ao longo deste ano foi fruto de muito conhecimento transmitido, trabalho de equipa e apoio de várias pessoas que sem elas não teria sido possível entregar esta dissertação.

Assim, passo primeiro por agradecer à minha orientadora, a Professora Doutora Ângela Sousa, e à minha coorientadora, a Professora Doutora Diana Costa, por todo o conhecimento transmitido e por todo o apoio. Uma obrigada por me terem acompanhado e guiado ao longo desta jornada da qual levo boas memórias. Ao Professor Doutor Luís Passarinha, obrigada pela ajuda dispensada e pelo conhecimento de biorreator que foi fundamental para a elaboração deste trabalho. Também gostaria de agradecer à Professora Swati Biswas pela colaboração na síntese e caracterização do péptido usado no trabalho. Uma obrigada à Professora Doutora Susana Ferreira por toda ajuda dispensada e pelo conhecimento que me deu.

À Universidade da Beira Interior e ao Centro de Investigação em Ciências da Saúde por me ter disponibilizado todas as condições necessárias à realização desta dissertação.

Ao meu grupo de investigação, obrigada pela partilha, apoio e paciência que tiveram comigo, por terem estado lá quando precisei e por todo o conhecimento que me passaram.

À Sofia, ao Carlos, ao Renato, à Filomena, à Francisca, ao Rodrigo, à Margarida Lorigo, à Ana Margarida Gonçalves, ao Joel, uma obrigada do fundo do coração por todos os bons momentos passados. Pelos risos e gargalhadas. Pelas “noitadas” de trabalho e companhia nos momentos mais difíceis. Pelo apoio, pela motivação e por terem estado sempre, sempre, sempre lá quando eu mais precisei. Sem vocês não teria sido a mesma coisa e, por isso, levo cada um de vocês para a vida.

Aos meus melhores amigos, a Catarina e o Cláudio, obrigada pela amizade e por todos momentos que passamos desde que nos conhecemos. Mesmo estando longe sempre pude contar com vocês e não podia pedir por melhores amigos que vocês! Um enorme obrigada.

Um especial obrigado à minha Alexandra, à minha prima, ao meu xuxu! A ti que me acompanhaste desde o meu primeiro dia na UBI e sei que estarás ao meu lado no último. Obrigada por todo o apoio incondicional, por todos os nossos jantares até de madrugada, pelas nossas conversas intermináveis, e por seres como és! És muito especial para mim e sabes bem que te adoro do fundo do coração.

Ao meu pai, Franck, à minha mãe Tina, obrigada por aturarem a filha mais velha e mais chata que poderiam ter. Obrigada por me terem apoiado sempre a seguir os meus sonhos e por me terem ensinado que nunca devo desistir. Foram 6 anos longos, de esforço, lágrimas, stresse, e sempre estiveram lá para me apoiar, reconfortar e motivar. Obrigada por serem os melhores pais que poderia pedir. *Je vous aime*.

À Sónia, o meu unicórnio fofo. Uma irmã como tu só podia ser minha, pois não deixava que fosse de mais ninguém. Por mais chata que sejas, sabes dar bons conselhos e estiveste sempre "presente" para ser o ombro amigo que eu precisava. Mais que uma irmã, és a minha melhor amiga! Obrigada por tudo sis. *Je t'aime fort*.

Aos meus avós, Fausta, Lurdes, Aníbal e António, obrigada por sempre acreditarem que a vossa "pequena" neta iria conseguir chegar tão longe. Obrigada pelo amor incondicional que sempre me deram e que por mais longe que estivessem, estavam sempre perto. *Je vous aime tous*.

Por fim, mas não menos importante, Carlos Alexandre Ribeiro Andreso, meu amor, obrigada! Não há palavras para descrever tudo o que fizeste por mim desde que nos conhecemos. Nunca me deixaste desistir e nunca me deixaste ir abaixo. Por mais desmotivada que estivesse, tu conseguias voltar a motivar-me. Sempre que uma lágrima aparecia, tu limpavas e convertias num sorriso. Sempre me fizeste acreditar que tudo é possível e que não há limites quando queremos alcançar algo. Obrigada por tudo. Amo-te até ao infinito e mais além.

Resumo Alargado

As vacinas de ácidos nucleicos provaram ser uma tecnologia promissora na luta contra ameaças globais como a doença coronavírus (COVID-19). O DNA minicircular (mcDNA) é um vetor inovador, mais estável do que o RNA mensageiro e mais eficiente na transfecção celular e expressão transgénica do que o DNA plasmídico convencional.

Este trabalho descreve a construção de um vetor de plasmídeo parental (PP) que codifica o domínio de ligação ao recetor (RBD) da proteína S da Síndrome Respiratória Aguda Severa do coronavírus (SARS-CoV-2), e a utilização do Desenho Experimental (DoE) para otimizar a recombinação do PP em mcDNA no agitador orbital. Primeiro, os resultados revelaram que as células hospedeiras devem ser cultivadas a 42 °C com meio *Terrific Broth* (TB) e, posteriormente, deve ser substituído por meio *Luria Broth* (LB) contendo 0,01% de L-arabinose para a etapa de indução. A concentração de antibióticos, o tempo de indução, e a temperatura de indução foram utilizados como *inputs* para o DoE com o intuito de maximizar a % de mcDNA recombinado. O modelo quadrático foi estatisticamente significativo ($p < 0,05$) e apresentou um *lack of fit* não significativo ($p > 0,05$) com um coeficiente de determinação adequado. A produção de mcDNA foi então maximizada numa plataforma de mini-bioreactor. A condição mais favorável no biorreator foi obtida aplicando 60% pO_2 na etapa de fermentação durante 5 h e 30% pO_2 na etapa de indução, com 0,01% de L-arabinose durante 5 h.

A aplicação de sistemas de entrega melhora a eficácia das vacinas de DNA e permite o seu direcionamento quando funcionalizadas com ligandos específicos. O quitosano (Ch) é um polímero natural catiónico, conhecido pelas suas propriedades biodegradáveis, biocompatíveis, mucoadesivas e de baixa citotoxicidade, e tem sido explorado na formulação de sistemas de entrega de biofármacos. A complementação com tripolifosfato (TPP) permite a criação de um sistema de estabilização reticulado através de interações eletrostáticas entre as cargas positivas de Ch e as cargas negativas do TPP e do DNA. A funcionalização com um péptido de penetração celular, como a octa-arginina (R8) melhora a capacidade de penetração e de entrega de biomoléculas. A decoração dos sistemas de entrega com ligandos de manose favorece o reconhecimento específico pelos recetores de manose sobrexpressos na superfície das células apresentadoras de antigénios (APCs). Neste trabalho foram explorados dois polímeros de Ch (HMW e 5 kDa) para formular diferentes nanosistemas baseados em Ch-TPP/R8 e R8-manose para a obtenção de uma nova vacina contra COVID-19, codificando o gene RBD do SARS-CoV-2. Para este efeito, foram avaliados diferentes rácios de TPP, R8 e R8-manose. Todos os sistemas foram formulados utilizando a técnica de *ionotropic gelation* e o seu tamanho, carga superficial, eficiência de encapsulação e estabilidade foram subsequentemente avaliados. A espectroscopia de infravermelho por transformada de Fourier (FTIR) e a microscopia eletrónica de varrimento (SEM) foram também realizadas para determinar os grupos funcionais presentes na superfície das nanopartículas e a sua forma e morfologia, respetivamente. Duas linhas celulares, fibroblastos

humanos (h-Fibro) e células dendríticas imaturas (JAWS II), foram utilizadas em estudos *in vitro* para avaliar a biocompatibilidade, eficiência da transfecção e expressão génica dos sistemas formulados. Os ensaios de 3-[4,5- dimetiltiazol-2-il]-2,5-difeniltetrazólio (MTT) mostraram a biossegurança de todos os nanosistemas baseados em Ch. Posteriormente, foram efetuados estudos de microscopia confocal em células dendríticas (JAWSii), para verificar a diferença na internalização de sistemas não-manosilados e manosilados em APCs.

Este trabalho revelou que a aplicação do biorreator aumentou fortemente o rendimento da biomassa do hospedeiro e simultaneamente melhorou os níveis de recombinação do PP em mcDNA. Adicionalmente, o uso de sistemas de entrega baseados em quitosano mostra um enorme potential para entrega da vacina de DNA, sendo que os sistemas manosilados permitem uma entrega direcionada às APCs melhoram a internalização da vacina de DNA.

Palavras-chave

COVID-19; maximização do mcDNA; quitosano; sistemas de entrega; vacinas de DNA.

Abstract

Nucleic acid vaccines have proven to be a promising technology in the fight against global threats such as coronavirus disease (COVID-19). Minicircle DNA (mcDNA) is an innovative vector more stable than messenger RNA and more efficient in cell transfection and transgene expression than conventional plasmid DNA.

This work describes the construction of a parental plasmid (PP) vector encoding the receptor-binding domain (RBD) of the S protein from severe acute respiratory syndrome coronavirus 2 (SARS-CoV-2), and the use of the Design of Experiments (DoE) to optimize PP recombination into mcDNA vector in an orbital shaker. First, the results revealed that host cells should be grown at 42 °C and the Terrific Broth (TB) medium should be replaced by Luria Broth (LB) medium containing 0.01% L-arabinose for the induction step. The antibiotic concentration, the induction time, and the induction temperature were used as DoE inputs to maximize the % of recombined mcDNA. The quadratic model was statistically significant (p-value < 0.05) and presented a non-significant lack of fit (p-value > 0.05) with a suitable coefficient of determination. The production of mcDNA was then maximized in a mini-bioreactor platform. The most favorable condition obtained in the bioreactor was obtained by applying 60% pO_2 in the fermentation step during 5 h and 30% pO_2 in the induction step, with 0.01% L-arabinose throughout 5 h.

The application of delivery systems improves the DNA vaccines efficacy and allows their targeting when functionalized with specific ligands. In this work were explored two chitosan (Ch) polymers to formulate different Ch-TPP/R8 and R8-mannose based nanosystems for the delivery of a new mcDNA vaccine against COVID-19, encoding the receptor-binding domain (RBD) gene of severe acute respiratory syndrome coronavirus (SARS-CoV-2). For this purpose, different ratios of TPP, R8 and R8-mannose were evaluated. All systems were formulated using the ionotropic gelation technique and their size, surface charge, encapsulation efficiency and stability were subsequently evaluated. Fourier transform infrared spectroscopy (FTIR) and scanning electron microscope (SEM) were also performed to ascertain the functional groups on the surface of the nanoparticles and their shape and morphology, respectively. Two cell lines, human fibroblasts (h-Fibro) and immature dendritic cells (JAWS II) were used in *in vitro* studies to evaluate the compatibility, transfection efficiency and gene expression of formulated systems. The 3-[4,5- dimethylthiazol-2-yl]-2,5-diphenyltetrazolium (MTT) assays showed the biosafety of all Ch-based nanosystems. Subsequently, confocal microscopy studies were performed on dendritic cells (JAWSii), to verify the difference in internalization of non-mannosylated and mannosylated systems in APCs. Systems functionalized with R8-mannose showed better internalization into the cells.

Keywords

COVID-19; mcDNA maximization; chitosan; delivery systems; DNA vaccines.

Index

List of Figures

List of Tables

List of Acronyms

2019-nCoV	New coronavirus-19
aa	Aminoacides
AC	Affinity chromatography
ACE2	Angiotensin-converting enzyme 2
Acr	Antigen-alpha crystallin
Ad26	Adenovirus serotype 26
AEC	Anion exchange chromatography
AEs	Adverse events
APCs	Antigen-presenting cells
BVDV	Bovine viral diarrhea virus
CCF	Central Composite Face
Ch	Chitosan
ChNPs	Chitosan Nanoparticles
COVID-19	Coronavirus disease 2019
CoVlp	Coronavirus viral particles
CoVs	Coronavirus
CPP	Cell-penetrating peptides
CQ	Chloroquine
DC-SIGN	DC-specific ICAM-3 grabbing non-integrin
DCs	Dendritic cells
DEPC	Diethyl pyrocarbonate water
DLS	Dynamic light scattering
DMEM/F- 12	Dulbecco´s Modified Eagle´s Medium with Ham's F-12 Nutrient Mixture
DNGR-1	Dendritic cell natural killer lectin group receptor-1
DO	Dissolved oxygen
DoE	Design of experiments
dsDNA	Double-stranded DNA
E. coli	*Escherichia coli*
E protein	Envelope protein
EPR	Enhanced Permeability Retention
FBS	Fetal bovine serum
FDA	Food and Drug Administration
FibH	Fibroblasts
FTIC	Fluorescein isothiocyanate
FTIR	Fourier transform infrared spectroscopy
FVP	Favipairavir
gDNA	Genomic DNA
HA	Haemagglutinin
HCQ	Hydroxychloroquine
HIC	Hidrophbic interaction chromatography

HIV	Human immunodeficiency virus
HPLC	High Performance Liquid Chromatography
hrsACE2	Soluble form of recombinant human ACE2
iDC	Immature dendritic cells
IFN-I	Type I interferons
IG	Ionotropic gelation
IMAC	Immobilized metal affinity chromatography
JIA	Juvenile idiopathic arthritis
kbp	Kilobase pair
LB	Luria Broth
M protein	Membrane protein
mAb	Monoclonal antibody
mcDNA	Minicircle DNA
MEM-α	Minimum Essential Medium α
MERS-CoV	Severe Middle East Coronavirus
MHC	Major histocompatibility class
miRNA	Micro RNA
mP	Mini plasmid
MR	Mannose receptor
mRNA	RNA messenger
MV	Measles virus
MVA	Modified vaccinia ankara
N protein	Nucleocapsid protein
NIBS	Non-invasive back scattering optics
NPs	Nanoparticles
nt	Nucleotides
oc	Open circular
OD	Optical density
ORF1	Open reading frame
ORI	Origin of replication
PAE	Poli(beta-amino ester)
PAMAM	Poly(amidoamine)
PCR	Polymerase Chain Reaction
PDI	Polydispersion Index
PDMAEMA	Poly[2-(N,N-dimethylamino)ethyl methacrylate]
pDNA	Plasmid DNA
PEC	Polyelectrolyte complexes
PEI	Poly(ethyleneimine)
PLL	Poly-L-lysine
pO_2	Oxygen Pressure
PP	Parental plasmid
PRR	Pattern recognition receptor
RA	Rheumatoid arthritis

RABV	Rhabdoviruses
RBD	Receptor-binding domain
RBM	Receptor-binding motif
RdRP	RNA-dependent RNA polymerase
RPC	Reversed-phase chromatography
RR	Respiratory rehabilitation
RT-PCR	Reverse Transcription Polymerase Chain Reaction
S protein	Spike protein
SARS-CoV	Severe Acute respiratory Syndrome Coronavirus
SARS-CoV-2	Severe Acute respiratory Syndrome Coronavirus 2
Sc	Supercoiled
SEC	Size exclusion chromatography
SFV	Semliki forest virus
SIN	Sindbis virus
siRNA	Small interfering RNA
Ssc	Systemic sclerosis
ssRNA	Single stranded RNA
T reg	Regulatory T cells
TB	Terrific Broth
TCZ	Tocilizumab
Th cells	T helper cells
THAC	Triple-helix affinity chromatography
TLR	Toll-like receptor
TMPRSS2	Transmembrane serine protease
TPP	Tripolyphosphate
VEE	Venezuelan equine encephalitis virus
VPLs	Virus-like particles
VSV	Vesicular stomatitis virus
WHO	World Health Organization
α-CoVs	Alphacoronavirus
β-CoVs	Betacoronavirus
γ-CoVs	Gammacoronavirus
δ-CoVs	Deltacoronavirus

List of Scientific Publications

I. Rodolfo C, Eusébio D, Ventura C, Nunes R, Florindo HF, Costa D, et al. Design of Experiments to Achieve an Efficient Chitosan-Based DNA Vaccine Delivery System. Pharmaceutics. 2021 Aug 31;13(9):1369.

II. Ventura C, Eusébio D, Gonçalves AM, Barroca-Ferreira J, Costa D, Cui Z, et al. Maximization of the Minicircle DNA Vaccine Production. Biomedicines. 2022;10(5):1–18.

III. Ventura C, Luís Â, Soares CP, Venuti A, Paolini F, Sousa Â. The Effectiveness of Therapeutic Vaccines for the Treatment of Cervical Intraepithelial Neoplasia 3 : A Systematic Review and Meta-Analysis. Vaccines. 2022;10(1560):1–18.

List of Scientific Comunication

I. Oral communication in the XVI Annual Symposium of CICS-UBI, Covilhã (2021): Cathy Ventura, Dalinda Eusébio, Luís Passarinha, Ângela Sousa. Optimization of minicircle DNA recombination conditions exploring design of experiments using Erlenmerys.

Chapter 1

Introduction

1.1. Coronavirus Disease 2019 (COVID-19)

In late 2019, an outbreak of a respiratory illness was reported in the city of Wuhan, China. On 9 January 2020, the Chinese Centre for Disease Control and Prevention reported the identification of a new coronavirus, and the World Health Organization (WHO) subsequently announced that it would be designated "new coronavirus-19" (2019-nCoV) (1,2). On 11 February 2020 it was renamed "COVID-19" (coronavirus disease 2019) by the WHO (2).

Several studies have been conducted to clarify the clinical signs present in positive cases for COVID-19, having been considered fever, dry cough, myalgia, dyspnea, fatigue, shortness of breath, and breathing difficulty. In addition, less common symptoms such as headache, abdominal pain, diarrhea, nausea, vomiting, and dizziness were also reported (2–6). COVID-19 has been divided into 4 levels of symptoms: the medium level, where patients present mild symptoms; the moderate level, in which fever, respiratory symptoms, and radiological evidence are already present; the severe level, which is divided into 3 criteria - a) dyspnea when respiratory rehabilitation (RR) is greater than 30 times per minute, b) if oxygen saturation is less than 93% and c) when the ratio between arterial oxygen partial pressure and fractional inspiratory oxygen (PaO_2/FiO_2) is less than 300 mmHg; and finally, the critical level, also divided into 3 criteria - a) respiratory failure, b) septic shock and c) multiple organ failure (2).

A global health emergency alert was activated on 27 February 2020, as this new coronavirus had spread rapidly to 46 countries (2). According to the current situation (25th May 2022) by WHO, 523,786,368 cases of infection and 6,279,667 deaths have been reported worldwide (**Figure 1**).

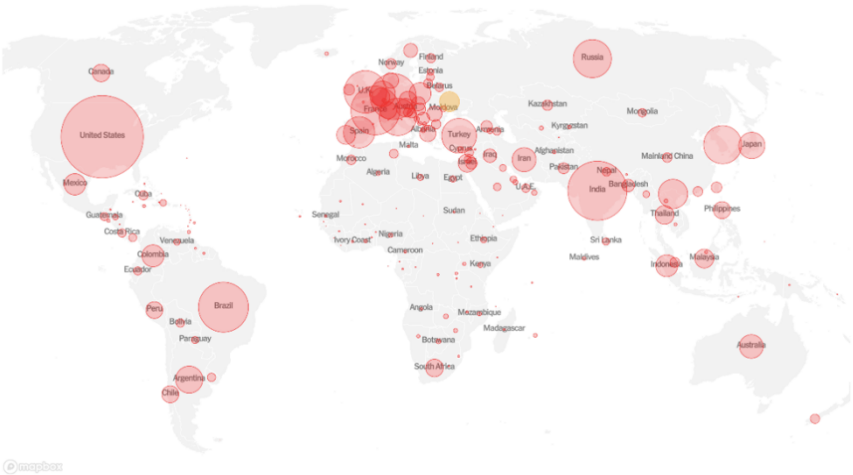

Figure 1 - Coronavirus World Map: Total cases (7).

1.2. Severe Acute Respiratory Syndrome Coronavirus – 2

1.2.1. Classification, comparison, and origin

Coronaviruses (CoVs) belong to the family of "*Coronaviridae*", subfamily of "*Coronavirinae*", and further in 4 genera: "*Alphacoronavirus*" (α-CoVs), "*Betacoronavirus*" (β-CoV), "*Gammacoronavirus*" (γ-CoV) e "*Deltacoronavirus*" (δ-CoV). They are a large family of single-stranded RNA (ssRNA) positive-sense viruses and can infect humans, birds, and other mammals and can cause neurological, hepatic, enteric, and respiratory diseases (8). To date, seven strains of CoVs can infect humans. Four of them, HCoV-OC43, HCoV-229E, HCoV-HKU1, and HCoV-NL63, cause infections with cold-like symptoms and rarely cause infections with more severe symptoms, with severe cases occurring only in children, teenagers, and elderly. The remaining three strains are severe acute respiratory syndrome coronavirus (SARS-CoV), severe middle east coronavirus (MERS-CoV), and severe acute respiratory syndrome coronavirus-2 (SARS-CoV-2). The latter three infect the lower respiratory system and have the ability to cause pneumonia and severe respiratory illness, being identified as β-CoVs (1,8,9).

Similar to SARS-Cov-2, SARS-CoV and MERS-CoV have also been responsible for outbreaks in previous years. SARS-CoV led to an outbreak in Guangdong, China, between 2002 and 2003. During this outbreak, 8,098 cases and 774 deaths were reported in 17 countries, with a mortality rate of 9.56%. On the other hand, MERS-CoV was responsible for an outbreak originating in Saudi, Arabia. Between 2012 and 2019, 2 506 cases and 862 deaths were recorded in 26 countries and its mortality rate was 35.37% (1,8). When comparing SARS-CoV-2 with SARS-CoV and MERS-CoV, similarities are observed at the nucleotide (nt) level of the RNA of each virus. SARS-CoV-2 shows homology of approximately 79% with SARS-CoV and close to 50% with MERS-CoV (1,2). However, there is yet another coronavirus that is more similar with SARS-CoV-2 to a coronavirus that infects bats, RaTG13, being similar at 96.2%, and with bat-SL-CoVZC45 and bat-SL-CoVZXC21, at 88%. These similarities may therefore suggest that bats are the natural host of SARS-CoV-2 (10).

1.2.2. Biology and genetics of SARS-CoV-2

The SARS-CoV-2 genome contains between 29,891 and 29,903 nt (2), and it is organized as follows: 5' - replicase (rep gene) ORF1ab, spike (S), envelope (E), membrane (M), nucleocapsid (N) - 3'. Structural and non-structural proteins are coded from the genome. Structural proteins include the S protein, which is a transmembrane glycoprotein whose function is to enable the binding of SARS-CoV-2 to the angiotensin-converting enzyme 2 (ACE2) receptor (8,11); N protein that allows viral RNA packaging and is essential for replication [11]; M protein that promotes nucleocapsid stability and facilitates the production and release of viral particles; and finally, E protein, which is important for viral production and maturation (**Figure 2**) (12).

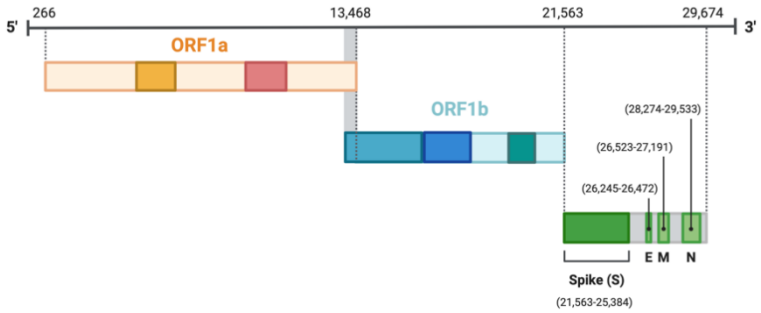

Figure 2 – Schematic representation of the genomes of SARS-CoV-2. Adapted from (13).

The S protein is divided into two subunits, the S1 subunit and the S2 subunit, each with its own specific function. The S1 subunit is responsible for the recognition and binding to the ACE2 receptor, while the S2 subunit allows the fusion between the membrane in SARS-CoV-2 and the host membrane. However, the S1 subunit possesses the receptor-binding domain (RBD) that has affinity for the ACE2 receptor (**Figure 3**) (14). The RBD region contains a core and receptor-binding motif (RBM), in which mutations may occur that affect the infectivity, pathogenesis, and interspecies transmission of SARS-CoV-2 (15). It is known that the RBD region of SARS-CoV-2 is very similar to that of SARS-CoV, which offers some knowledge that have been carried out with the S protein of SARS-CoV as a basis to understand the whole process of interaction of this protein with its receptor (2,15). Li *et al.* described that residues 479 and 487 from S protein of SARS-CoV are important for efficient infection of cells presenting ACE2, since they have a high affinity for this receptor (16).

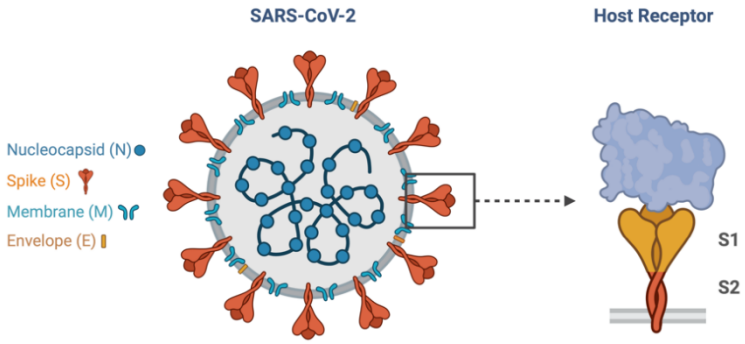

Figure 3 - Molecular structure of SARS-CoV-2. Adapted from (17).

1.2.3. SARS-CoV-2 life cycle

SARS-CoV-2 is a cytopathic virus, since it causes cell death in host cells as part of its replication cycle (18). The presence of its target receptor, ACE2, is significantly elevated in alveolar type II

epithelial cells, which are responsible for the gas exchanges that occur in the lungs (19). Moreover, this receptor is also found in type I pneumocytes, endothelial cells, heart, intestines, blood vessels, kidneys and bladder (20,21). However, type II alveolar epithelial cells are the main viral reservoir allowing dissemination of the virus throughout the body and between individuals (20,22).

The entire replication cycle process begins with the recognition and binding to the ACE2 receptor mediated by the S protein, through the RBD region located in the S1 subunit that promotes receptor recognition (12). The RBD region is constantly undergoing conformational change, moving from a more open conformation (standing-up position) at the time of binding to the ACE2 receptor, to a more closed conformation (lying-down position) allowing escape from the immune system (23,24). When the RBD region and the ACE2 receptor interact, SARS-CoV-2 is endocytosed into the host cell to form an endosomal vesicle. In this vesicle, there is an increased influx of H^+ protons promoting the activation of cathepsin L that will activate the S protein and thus allow fusion of the viral membrane, and subsequently, the release of ssRNA from the endosome (**Figure 4**) (25).

When comparing SARS-CoV with SARS-CoV-2, the affinity between the RBD region and the ACE2 receptor is higher in SARS-CoV-2 (15). By cryo-electron microscopy it was observed that the RBD region of SARS-CoV-2 is mostly in the closed conformation (26,27). Because of this conformation, the binding capacity between the S protein of SARS-CoV-2 and the ACE2 receptor is equal to or less than of SARS-CoV (23). Since binding to the ACE2 receptor is limited, SARS-CoV-2 has developed another strategy to facilitate its binding and internalization by the target cell, using activation of host proteases (27). This mechanism is used to cleave the bond between the S1 and S2 subunit and at the S2' site of the S protein in order to dissociate both subunits and thus allow the fusion between the SARS-CoV-2 membrane and the host cell membrane (24,28). Transmembrane serine protease 2 (TMPRSS2) mediates this cleavage in the S protein thus facilitating membrane fusion, releasing ssRNA into the cytoplasm of the host cell (25). Once inside the cell, firstly the SARS-CoV-2 RNA serves as messenger RNA (mRNA) for the open reading frame (ORF1) sequence to be translated into viral replicases, which will be subsequently cleaved by viral proteinases. This initial step will let the synthesis of viral RNA, which is composed by 2 parts: the first step being genomic replication and the subsequent sub-genomic RNA transcription that will be translated into structural proteins. These proteins are important for the RNA synthesis by the RNA-dependent RNA polymerase (RdRP) that will be responsible for the genomic RNA replication and will be released due to the fusion with the host cell membrane. The involvement of viral genetic material with the cell membrane constitutes an immune system evasion mechanism since the pattern recognition receptor (PRR), which is able to trigger an immune response against the pathogen, is protected inside the cell membrane (29).

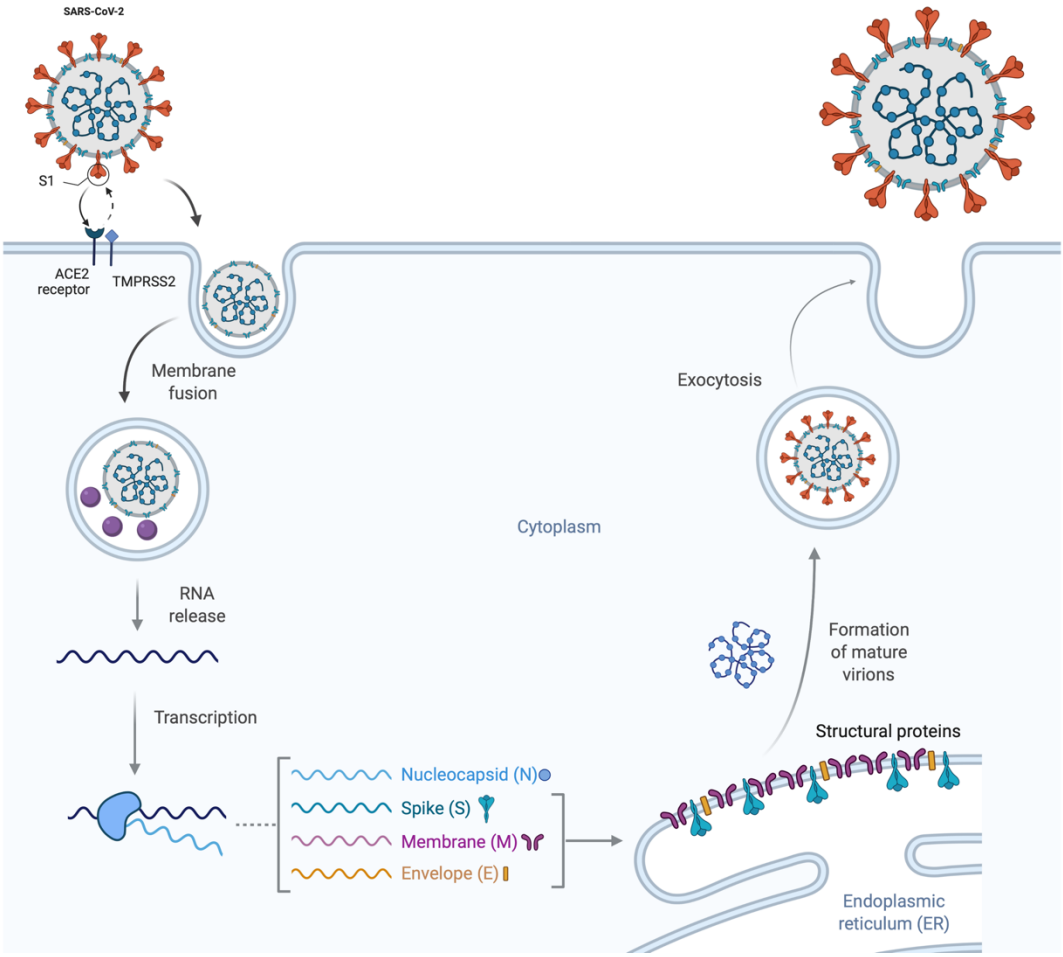

Figure 4 - The mechanism of COVID-19 infection and the amplification process of SARS-CoV-2. Adapted from (29).

1.2.4. Immune response against SARS-CoV-2

Innate immunity is the first line of defense against pathogens, with the expression of type I interferons (IFN-I) and pro-inflammatory cytokines being the "alarm" signal (29). Innate immunity by itself has three main goals, namely restricting viral infection only in already infected cells, creating an antiviral environment by recruiting effector cells and initiating the priming of adaptive immunity. The activation of adaptive immunity is more time-consuming, since it is necessary to select and expand T and B cells specific for that particular antigen (**Figure 5**) (30).

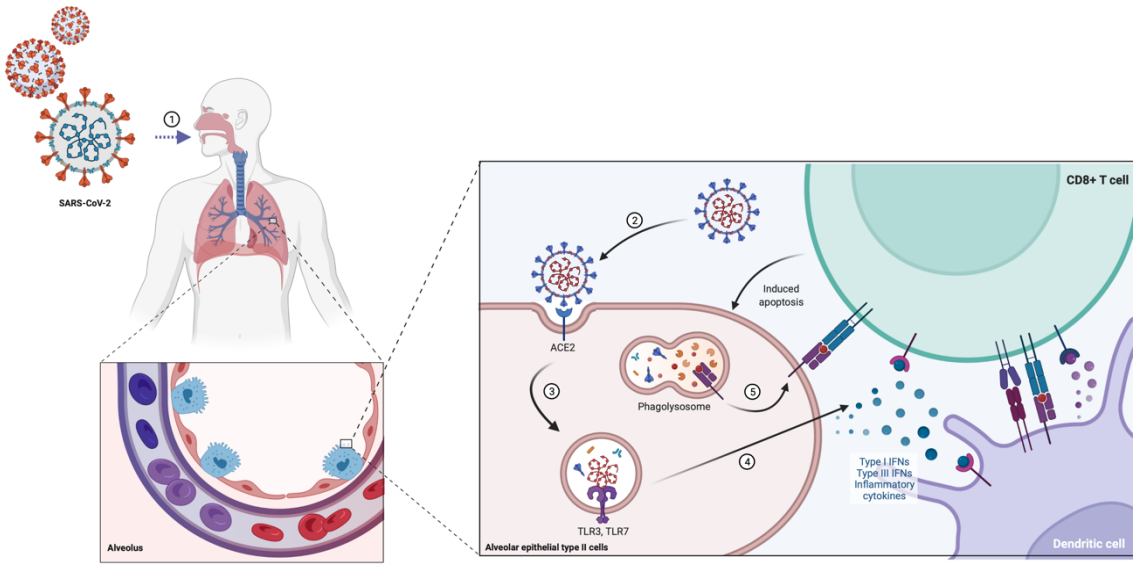

Figure 5 - SARS-CoV-2 alarming the innate and adaptive immune system. **(1)** Entry of the SARS-CoV-2 via cells within the nasal cavity and the upper and lower respiratory tract. **(2)** Recognition, binding between ACE2 and S protein of SARS-CoV-2, fusion of the membrane and RNA release. **(3)** SARS-CoV-2 is most likely recognized by PRRs recognizing foreign RNA including endosomal TLR3 and TLR7. **(4)** Triggering signaling pathways that will activate the transcription of inflammatory cytokines, IFN-I and IFN-III. Recruitment of cells of the innate immune system to contain infection. **(5)** Expression of the antigen by the infected cell. Adapted from (31).

As mentioned earlier, SARS-CoV-2 has the ability to evade early innate immunity (30), preventing the triggering of innate immune responses associated with type I and type III IFNs (32). If there is a delay in the innate immune response, COVID-19 becomes more aggressive. This delay allows the virus to significantly advance in replication, the non-development of the adaptive immune response is compromised and prolonged in time, thus resulting in severe lung disease (30,33).

1.3. Vaccines and Therapies

1.3.1. Inhibitors of virus entry

Arbidol is an antiviral drug against the Influenza virus that targets viral haemagglutinin (HA). This antiviral apparently prevents the binding of SARS-CoV-2 to its receptor and has an anti-inflammatory activity (34). When the sequences of the S protein of SARS-CoV-2 and the HA of influenza are compared, there is a small region of the S2 subunit (aa947 - aa1027) of the S protein of SARS-CoV-2 that resembles to the HA of influenza virus. The structural similarity was also demonstrated in the arbidol-binding region of both the S protein and HA. These structural and sequence similarities can be explored to develop a possible treatment against COVID-19 (35). A study by Z. Wang *et al.* showed that arbidol has a beneficial effect on the recovery of infected patients associated with a decrease in mortality (36).

The use of a soluble form of recombinant human ACE2 (hrsACE2) is a strategy that allows the neutralization of SARS-CoV-2 by blocking the S protein and by hyper-activating the renin-angiotensin system and increasing plasma angiotensin II concentration. Zoufaly *et al.* showed

that hrsACE2 administration decreased the plasma concentration of angiotensin II and also promoted a decrease in levels of pro-inflammatory cytokines (IL-6 and -8) and other inflammatory markers (TNF-α and ferritin) (37).

Chloroquine (CQ) and hydroxychloroquine (HCQ) are drugs used as anti-malarial and in the treatment for autoimmune diseases such as lupus and rheumatoid arthritis. They act as entry blockers for the virus, by increasing the pH in the endosomal vesicle formed when the host cell membrane fuses with the virus membrane. They also interfere with the glycolysis of the SARS-CoV cell receptors (38,39). Studies have described that, regardless of the excellent activity demonstrated against Influenza, there is no clinical benefit in the administration of CQ and HCQ. The use of these drugs is associated with cardiovascular and other risks when administered in high doses or combined with other types of treatments. Both CQ and HCQ have immunomodulatory activity against COVID-19, with mechanisms unknown so far, but may be related to the inhibition of the anti-viral immune response, both innate and adaptive (39).

1.3.2. Proteolytic Inhibitors

Proteolytic inhibitors have been used in the treatment of human immunodeficiency virus (HIV), such as lopinavir combined with ritonavir, being approved by the FDA (Food and Drug Administration) (40). Against SARS-CoV-2, lopanavir alone and in combination with ritonavir have been tested, however, it has been found that when applied alone, it shows effective neutralisation with an acceptable EC_{50} concentration (41).

However, the combination with ritovanir has not been shown to have any beneficial effect on patients infected with COVID-19 or on the mortality rate caused by it, so further trials will be needed to improve the efficacy of this combination (42).

1.3.3. RNA polymerase inhibitors

Favipairavir (FVP) is a purine analog that has the ability to inhibit RdRP and has demonstrated effects against influenza virus, RNA viruses, and SARS-CoV-2 *in vitro* (43). FVP is currently in phase III clinical trials with satisfactory results, but further clinical trials are still needed (19).

Remdesivir, also known as GS-5734, is a prodrug analog of adenosine and has a range of antiviral action against filoviruses, paramyxoviruses, pneumoviruses, and CoVs. In *in vitro* studies, this product inhibited SARS-CoV-2 and showed antiviral activity in animal models against SARS-CoV and MERS-CoV (44). The use of remdesivir allowed an increase in the patients' recovery time, although this was not reflected in survival rates. In clinical trials, there was a 3.8% decrease in mortality when compared to the placebo group. However, the WHO has expressed its opposition to the use of this drug in hospital settings (19).

1.3.4. Vaccines

Vaccines were the first approach to be researched and developed for pandemic control, being the most effective method for acquiring immunity against a pathogen. Due to the global mobilization

to fight this pandemic, several countries have focused on research and development of vaccines against COVID-19, and more than 600 vaccines are in clinical trials, 35 of which have already been approved in several countries (**Figure 6**) (45).

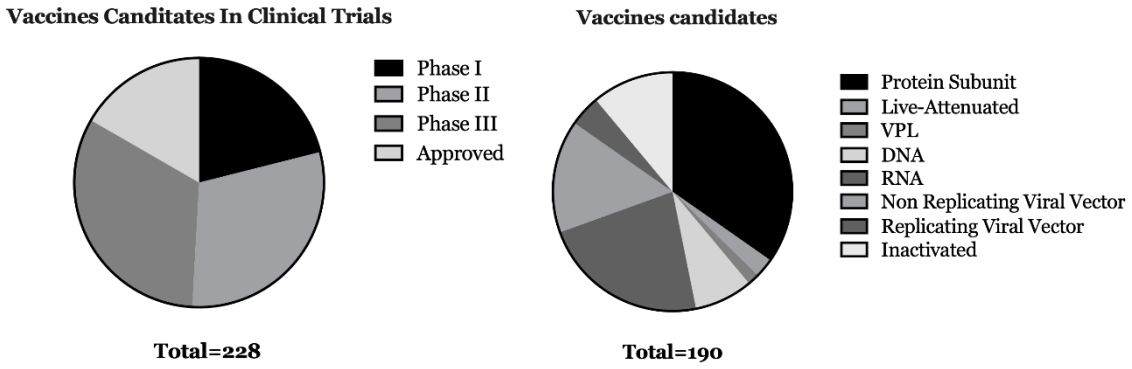

Figure 6 – Scheme showing all vaccines being studied worldwide, and the types of vaccines. Adapted from (45).

1.3.4.1. Inactivated virus vaccine

Inactivated virus vaccines are produced by exposing virulent viruses to chemical or physical agents, for example, formalin or β-propiolactone (46). To date, three inactivated virus vaccines have been approved by WHO.

Covaxin (BBV152), formulated with aluminum hydroxide gel adjuvants (Algel) or 7/8 chemoattractant toll-like receptor (TLR) agonists adsorbed on Algel, was verified for immunogenicity and safety in *in vivo* studies. A significant response was generated and reflected in the increase of neutralizing antibodies (NCT04641481; NCT05258669; NCT04918797; CTRI/2022/02/040065) (**Table 1**) (47). This vaccine has been approved in 14 countries, including India, Mexico and Iran.

Table 1 – List of vaccines in phase III and approved by the WHO.

ID Number	Phase	Vaccine Name	Properties	Vaccine Features	Status
NCT04641481 NCT05258669 NCT04918797 CTRI/2022/02/040065	III	Covaxin	Inactivated virus	Whole-Virion Inactivated SARS-CoV-2 Vaccine	Approved
ChiCTR2000032459 IRCT20171122037571N3 NCT05109559	III	Covilo		Whole-Virion Inactivated SARS-CoV-2 Vaccine	Approved
NCT04352608	III	CoronaVac		Whole-Virion Inactivated SARS-CoV-2 Vaccine	Approved
ISRCTN15779782	III	COVI-VAC	Live Attenuated virus	-	Phase III
NCT04611802 NCT04583995 NCT05249816 NCT05236491 CTRI/2021/02/031554	III	Novavax	Protein Subunit	S protein with matrix M adjuvant	Approved
NCT04636697	III	Covifenz	VLPs	Complete S protein expressed in *N. benthamiana* plants with adjuvant	Approved
NCT04505722	III	Janssen	Non-Replicating Viral Vector	Recombinant and replicating Ad26 encoding a stabilized S protein	Approved
NCT04516746	III	AstraZeneca		Non-replicating chimpanzee adenovirus vector vaccine expressing the FLS-CoV-2 glycoprotein gene	Approved
NCT04368728	III	Comirnaty	RNA	mRNA encodes the RBD of the SARS-CoV-2 S protein with adjuvant	Approved
NCT04927065	III	Spikevax		mRNA encoding the S-2P antigen composed of the S protein and the intact S1-S2 cleavage site	Approved
CTRI/2021/01/030416	III	ZyCoV-D	DNA	Plasmid vector pVAX1 DNA that encodes S protein along with the sequence coding for the IgE signal peptide	Approved

Covilo (BBIBP-CorV), containing aluminum hydroxide as an adjuvant, is a safe and immunogenic vaccine, producing humoral immune responses by day 4 of vaccination. Phase I/II studies have shown that administration of two doses, on day 0 and 21 or day 0 and 28, showed high levels of neutralizing antibodies (ChiCTR2000032459; IRCT20171122037571N3; NCT05109559) (**Table 1**) (48). It has been approved in over 90 countries and implemented by the African Approved Regulatory Working Group and the Caribbean Approved Recommendation for Emergency Use of the Regulatory System.

CoronaVac, also with aluminum hydroxide as an adjuvant, demonstrated to be a safe and immunogenic vaccine. It showed favorable conditions to be approved for phase III clinical trials in both dosing and booster vaccines (NCT04352608) (**Table 1**) (49). It has been approved in over 50 countries and implemented by the African Approved Regulatory Working Group and the Caribbean Approved Recommendation for Emergency Use of the Regulatory System.

1.3.4.2. Live attenuated virus vaccine

Live attenuated vaccines allow replication of the virus, amplifying the antigen for presentation to the immune system. The advantage of this technology is that it mimics wild-type virus replication, eliciting an immune response similar to what would occur in natural infection (46).

COVI-VAC in phase I clinical trials involved 48 volunteers to test three different doses of the vaccine for safety and dose-response (NCT04619628; NCT05233826) (**Table 1**) (50). It is currently in phase III clinical trials that will assess the safety of the vaccine by monitoring and reporting adverse events (AEs) at any time after vaccination (ISRCTN15779782).

1.3.4.3. Subunit vaccine

Subunit vaccines contain the antigen (toxoid, submolecular fragments, and surface molecules) purified rather than using the whole virus. When protein antigens are applied, the T-cell-dependent adaptive immune response is elicited. But when polysaccharide antigens are applied, it is the T-cell-independent response that is developed (51).

Novavax (NVX-CoV2373) is the subunit vaccines approved by the WHO based on recombinant S-glycoprotein nanoparticles with matrix adjuvant-M1. In phase I/II clinical trials, the vaccine has shown to be safe and effective, providing an immune response by T helper (Th) cells. The adjuvant inclusion allowed an enhanced response with respect to the development of neutralizing antibodies and Th (52). The phase III clinical trials included a total of 15,187 participants, in which common reactogenicities such as tenderness, pain at the injection site, fatigue and muscle pain were reported. This vaccine revealed 89.8% of efficiency (NCT04611802; NCT04583995; NCT05249816; NCT05236491; CTRI/2021/02/031554) (**Table 1**) (53). It is approved in over 30 countries, including Belgium, Italy, Portugal, and Spain, and is on the WHO Emergency Use Listing.

1.3.4.4. Virus-like Particles Vaccines

Virus-like particles (VLPs) are used to enable effective epitope presentation by antigen-presenting cells (APCs) to present heterologous epitopes at high density to T and B cells. This approach produces a protective immune response similar to inactivated virus vaccines (54,55).

Covifenz has the complete SARS-CoV-2 S protein that was expressed in *N. benthamiana* plants using *A. tumifaciens* transfection, being tested with two different adjuvants: AS03 adjuvant and CpG1018 adjuvant. In phase I clinical trials, all formulations were well tolerated, and AEs were mild to moderate, transient, and higher in the adjuvant groups. Levels of neutralizing antibodies were almost zero, but these increased significantly in the adjuvanted formulations (NCT04450004) (**Table 1**) (56). In phase II/III clinical trials involving about 24,000 volunteers, the vaccine showed an efficacy of 69.5% against symptomatic infections and 78.8% in moderate to severe disease (NCT04636697) (57). Covifenz is currently only approved in Canada.

1.3.4.5. Non-Replicating Viral Vector Vaccine

The use of viral vector-based vaccines promotes long-term stability and a high level of protein expression that will induce robust immune responses while remaining harmless (58,59).

Janssen (Ad26.COV2.S) is a recombinant and replicating adenovirus serotype 26 (Ad26), encoding a SARS-CoV-2 stabilized S protein. During phase I/II clinical trials, AEs such as fatigue, headache, myalgia, and pain at the injection site were reported, with the most frequent systemic AE being fever. Antibody titers were detected in 90 % of participants and spike-binding antibody responses being of the neutralizing antibody type. The CD_4^+ T-cell responses were detected in 60 to 83% of participants, depending on the dose administered (NCT04436276) (60). In phase III clinical trials it has been shown that a single dose of Ad26.COV2.S provided 52.9% protection against moderate to severe–critical COVID-19 (NCT04505722) (**Table 1**) (61). Today, Janssen is approved in over 100 countries including Portugal, Spain, and France.

AstraZeneca (ChAdOx1 nCoV-19) is a non-replicating chimpanzee adenovirus vector vaccine, expressing the FLS-CoV-2 glycoprotein gene. In phase I/II clinical trials, three doses of the vaccine were studied to assess its reactogenicity and immunogenicity. The study showed that the levels of neutralizing antibodies increased 28 days after the administration of the first dose. When the third dose was given, neutralizing antibody levels increased again after 28 days. An increase in T-cell responses was also seen after a third dose (28 days) (NCT04324606, NCT04400838) (62). When the vaccine progressed to phase III clinical trials, a total of 32,451 participants were involved. The vaccine showed an efficacy of 74%. S and RBD antibody titers increased 57 days after injection. The neutralizing antibody levels also increased after 57 days (NCT04516746) (**Table 1**) (63). Besides of being a vaccine placed on the WHO Emergency Use Listing, it was approved in 138 countries.

1.3.4.6. Nucleic acid vaccines

1.3.4.6.1. RNA vaccines

RNA encodes the genetic information that enables the synthesis of proteins (58). mRNA-based vaccines then allow the transport of mRNA that will encode a virus protein. However, RNA is a relatively unstable molecule and optimizations have been required to improve its stability and protein translation efficiency, also improving its immune response (64).

There are two WHO-approved RNA vaccines that have been administered globally to combat this pandemic, and they were among the first vaccines to be approved. One of them was developed by BioNTech SE and Pfizer and it is a RNA vaccine encapsulated in lipid nanoparticles, called Comirnaty. The mRNA encodes the RBD of the SARS-CoV-2 S protein, which is fused to a folded trimerization domain derived from T4 fibritin to increase the vaccine immunogenicity. The stability and translation efficiency of the mRNA was improved by incorporating 1-methylpseudouridine instead of uridine to decrease immunogenicity in the innate immune response and to increase translation *in vivo*. The clinical trials for BNT162b1 revealed an increase in CD_4^+ and CD_8^+ T-lymphocytes as well as a strong response by the humoral component of the immune system, with anti-RBD IgG antibodies being detected at a higher concentration than patients subsequently on COVID-19. The level of neutralizing antibodies 43 days after vaccine administration increased between 0.7 and 3.5 depending on the dose administered. They also found that most of volunteers had Th1 lymphocytes, CD_8^+ and CD_4^+ T lymphocytes specific for the RBD of S protein (65,66). Another vaccine from the same company, BNT162b2, is based on the same technology but encodes the S protein of the complete SARS-CoV-2 modified by mutation of two proline proteins to fix its pre-fusion conformation, which will improve the development of neutralizing antibodies. In clinical trials, levels of neutralizing antibodies were similar to BNT162b1, however, it shows a lower systemic reactivity in volunteers between 65 and 85 years of age (67). The phase III clinical trials (NCT04368728) involved more than 43,000 volunteers, aged 16 years and older, and demonstrated 95% efficacy in preventing COVID-19.

Other vaccine designed by the company Moderna, Spikevax (mRNA-1273), is based on a mRNA encoding the S-2P antigen, composed by the S protein and the intact S1-S2 cleavage site. It has a pre-fusion conformation stabilized by two mutations in proline 986 and 987 located at the top of the central helix of the S2 subunit (68). In phase I clinical trials (NCT04283461) with 45 volunteers elicited a response from the humoral component of the adaptive immune system was greater the higher the dose administered, and this was increased with the second dose of the vaccine (69). In phase II/III clinical trials, the vaccine administration of 100 μg was tested and showed an increase of the geometric mean titers of neutralizing antibodies against SARS-CoV-2. The sero-response rate (booster dose versus primary series in a historical control group) was 100% after 28 days. Thus, boosting of this vaccine induced a robust neutralizing antibody response, and reactogenicity was higher with the 100 μg booster dose compared to the 50 μg authorized booster (NCT04927065) (**Table 1**) (70).

1.3.4.6.2. DNA vaccines

DNA vaccine can promote the delivery of genes or fragments encoding antigens, being safe, non-immunogenic, stable and inexpensive to produce (71). This technology effectively induces both humoral and cellular immune responses. APCs are the major target for receiving the genetic material carried by DNA vaccines (64).

ZyCoV-D is one of the first pDNA vaccines approved in the world. This vaccine is based on a plasmid vector pVAX1 DNA that encodes the S protein along with the sequence coding for the IgE signal peptide (59). In phase III clinical trials involving 27,703, the vaccine reflected 66.6% efficacy, being a safe and immunogenic vaccine (CTRI/2021/01/030416) (72). Until now, this vaccine was only approved in India.

1.3.4.6.3. DNA Vaccine-induced immunity

DNA delivery occurs in several steps that are initiated with the DNA condensation within the delivery systems. Then, the vaccine is subsequently administered into the body, followed by targeted delivery to specific cells promoting cellular uptake, endosomal release, nuclear transport, and unpacking of the carrier/DNA polyplexes before the final translation step into eukaryotic cells (73).

Following the vaccine presence in muscle tissues, it will be endocytosed by immature dendritic cells (iDC) that will preferentially present antigen via major histocompatibility class (MHC I or II) to CD_4^+ and CD_8^+ T cells in lymph nodes (**Figure 7**) (74).

The activation of naïve T cells requires the binding of antigen to specific T cell receptors (TCR) coupled with a co-stimulatory signal. CD_8^+ or CD_4^+ T cells form T cells based on antigen presentation by MHC class I or MHC class II molecules. Extracellular antigens are presented by MHC class II, activating CD_4^+ T cells, also known as T helper cells. On the other hand, intracellular antigens presented by MHC class I molecules promote the activation of CD_8^+ T cells, also known as cytotoxic T cells. Thus the cellular pathway of the immune system is activated (51).

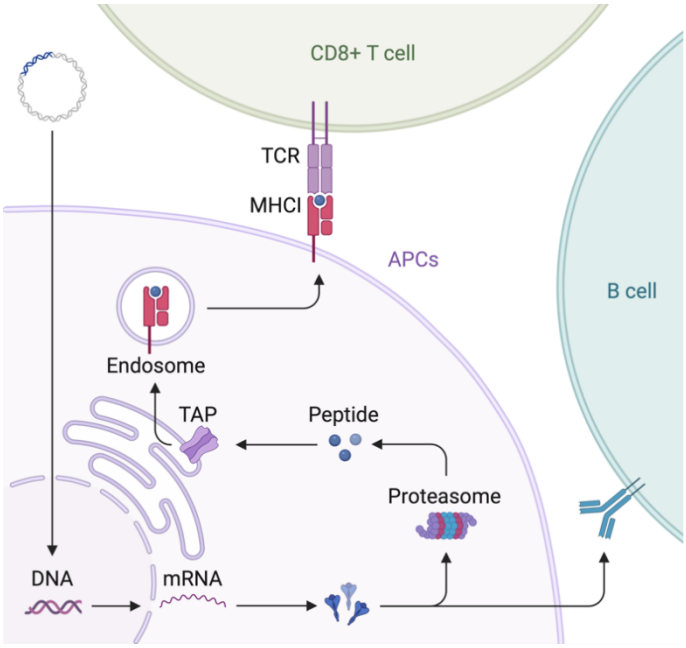

Figure 7 - Different pathways of the immune response to DNA vaccines. Adapted from (75).

1.3.4.7. Other strategies

Other alternatives are based on host protein blockade and immune response modulators. With regard to host protein blockade, Camostat mesylate is used in order to block TMPRSS2 activity preventing the entry of SARS-CoV-2 into the host cell (76). The modulators of immune responses, nitazoxanide interferes with viral infection by downregulating immune escape mechanisms. It can amplify the RNA sensing present in the cytoplasm and the type I IFN pathways allowing the innate immune system to be more effective. Clinical trials show no real efficacy *in vivo*. However, when applied against SARS-CoV-2 *in vitro*, it shows promising results but further studies are required to understand the role of this drug against COVID-19 (41).

The use of anti-inflammatory and anti-coagulant agents has been implemented as another approach to combat this pandemic as there is a strong inflammatory response in the lungs of individuals infected with SARS-CoV-2 (19). The tocilizumab (TCZ) is a recombinant humanized monoclonal antibody (mAb) of the IgG1 class whose function is to recognize the IL-6 receptor, both in soluble and membrane form (77). IL-6 is a cytokine that plays a very important role in both acute and chronic inflammation. Dysregulation or persistence in the production of this cytokine leads to the development of chronic inflammation associated with many diseases such as rheumatoid arthritis (RA), juvenile idiopathic arthritis (JIA), and systemic sclerosis (SSc), amongst others. TCZ has been applied to combat these pathologies and leads to a decrease in the levels of neutrophils, myeloid dendritic cells, monocytes, macrophages, and Th17 lymphocytes; an increase in regulatory T cells (T reg); induces the clonal expansion of regular B cells causing a decrease in hyperactive B cells and decreases the number of memory B cells in the periphery (78). In phase III clinical trials have been registered using TCZ, and additional trials are needed to determine the efficacy of this mAb during patient hospitalization (19).

Glucocorticoids have a suppressive effect on the immune system and inhibit the exaggerated inflammatory process through effective inhibition of pro-inflammatory cytokines, leading to the preservation of tissues and organs involved in acute respiratory problems. Since it has such capabilities it is used in critical COVID-19 patients who experience high levels of pro-inflammatory cytokines (79). A clinical trial demonstrated that giving a dose of dexamethasone (6 mg) reduced mortality associated with respiratory support patients, but it maybe harmful for patients who do not require oxygen support (80).

The use of plasma from patients who have recovered from COVID-19 to perform passive immunization is also a possible therapeutic approach. This route addresses the humoral immunity of previously infected patients to help prevent and treat already infected individuals. Passive immunization is approved by the WHO for the treatment and prevention of other diseases such as polio, measles, mumps, Ebola, SARS, MERS, and H1N1. It has been approved by the FDA and WHO despite the failure of other drugs being studied, and there are now several clinical trials to test the effectiveness of this therapy (81). A study in which 20,000 patients infected with COVID-19 received a convalescent plasma transfusion demonstrated that the application of plasma is safe, without complications for patients and also found a decrease in the mortality rate (82).

Related to passive immunization, the administration of neutralizing antibodies has been explored. LY-CoV555 (bamlanivimab, LY3819253) is a neutralizing anti-S mAbs with a high affinity for the RBD region of the S protein of SARS-CoV-2 and is a derivative of convalescent plasma from a patient infected with COVID-19. These mAbs, at the end of phase II clinical trial, proved an acceleration in the natural decline of viral load in infected patients with only one intravenous administration (83). AZD7442 is a combination of two antibodies, COV2-2196 and COV2-2130, isolated from convalescent plasma that can recognize S protein sites and synergistically neutralize SARS-CoV-2 when tested in animal models. *In vivo* tests demonstrated decreased viral load and decreased inflammation in lungs (84). There are also more mAbs in phase I clinical trials such as VIR-7831, 47D11, CT-P59, ALVR109, STI-1499, IVIG and COVID-HIG (19).

1.4. Plasmid DNA

In the area of gene therapy and DNA vaccines, different vectors can be used such as viral vectors, which include adenoviruses, retroviruses and lentiviruses, and non-viral vectors such as plasmid DNA (pDNA) and RNA. Viral vectors continue to be the most widely used in research, with 18.5% of clinical trials reported to use adenoviruses compared to 14.9% using free pDNA (93). This difference is associated with the high transfection efficiency of the viral vectors. However, it presents several disadvantages, such as immunogenicity and the capacity of genetic perturbation of the host, compromising the safety of this method. Thus, pDNA has been the alternative to non-viral vectors (94).

Plasmid DNA is a small circular DNA molecule, obtained through covalent bonding between two ends and is capable of self-replication within a host. The pDNA presents a size that can vary between 1 and 1000 kilobase pairs (kbp). It can present different conformations such as supercoiled (sc), denatured, relaxed, linear, and open circular (oc) (85). These five conformations differ in their size, charge, hydrophobicity, and exposure of bases (86). Over the years, the application of therapies such as DNA vaccines and gene therapy have been explored as pDNA is capable of expressing a gene of interest (87), has low toxicity and a safe profile to be applied as a new generation of biopharmaceuticals (88). The sc isoform is the biologically active conformation recommended for gene therapies and DNA vaccines due to absence of structural damages. However, the sc isoform can be converted into oc and linear isoforms due to physicochemical processes, which makes the purification of this molecule difficult (86).

To obtain pDNA, the first step is to build the expression vector and select the microorganism for its production. Next, the production conditions are chosen (upstream) and finally, the pDNA extraction and purification steps are taken (downstream) (**Figure 8**) (89).

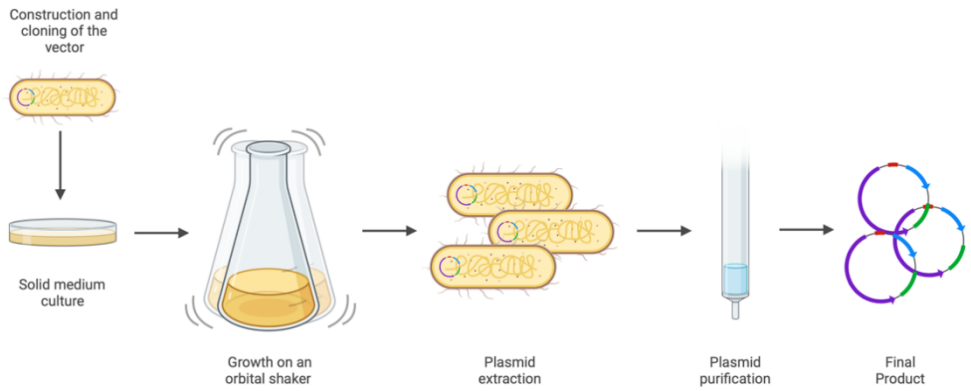

Figure 8 - Schematic representation of the biotechnological approach used in the plasmid DNA production. Adapted from (90).

1.4.1. Construction of plasmid DNA

The construction of pDNA is the first step in obtaining this biomolecule for application in DNA vaccines and gene therapy. It is primordial that the plasmid contains sequences for its replication and maintenance inside the microorganism and sequences for expression in the human host. At the replication stage, the plasmid must contain an origin of replication (ORI) and a selection marker to select the bacteria that have incorporated the plasmid, which could be an antibiotic resistance gene. When thinking about the applicability of the plasmid as a biopharmaceutical, it must contain a eukaryotic promoter, a termination sequence and the gene of interest (91). As a bacterial host, *Escherichia coli* (*E. coli*) is the microorganism par excellence, since it is a well-known and characterized organism, has a low production cost and a good yield (92).

1.4.2. Production of plasmid DNA

Once the vector of interest is constructed, it undergoes a fermentation process to increase the biomass and the number of pDNA copies inside the bacterial host. For this it is necessary to select a fermentation medium, pH, temperature and oxygen, as these parameters will influence the biomass and plasmid yields obtained (88,91). Thus, the bioprocess culminates with pDNA amplification, the final objectives being its extraction and purification of the sc pDNA isoform (90). After fermentation and for subsequent cell lysis, the medium with biomass should be centrifuged to recover a cell pellet (90). Cell lysis is performed in order to eliminate cellular debris and components such as genomic DNA (gDNA), RNA, endotoxins and proteins (89). As a final step, pDNA must go through a purification step in order to respect the purity and conformation grades implemented by regulatory agencies (90).

1.4.3. Purification of plasmid DNA

Chromatography allows to purify biomolecules, such as pDNA, using the various properties of each biomolecule (86). The increase of the purification yield is dependent on the optimization of the upstream process, since the greater the biomass the greater the quantity of pDNA and the extraction allows to eliminate most of the contaminants. There are different chromatographic techniques, such as molecular exclusion, hydrophobic, reverse phase, anion exchange and affinity (93), that explore the size, charge, hydrophobicity, base exposure and affinity of pDNA (94). Despite technological advances, poor selectivity and co-elution of molecules with similar properties has been a challenge for researchers dealing with sc pDNA purification (94).

1.4.3.1. Size-exclusion Chromatography

Size-exclusion chromatography (SEC) is based on the difference in sizes of the lysate components (94). It can be used to eliminate low molecular weight molecules such as RNA and endotoxins (88). There are two types of media for SEC, Superose 6 (Pharmacia BioTech) and Sephacryl S1000 (Pharmacia Biotech). For both supports, the high molecular weight nucleic acids, gDNA and pDNA, are excluded from the matrix, being eluted in a first instance, and finally, the low molecular weight components enter the pores of the matrix delaying their elution (89). However, this technique shows poor selectivity for pDNA isoforms. Therefore, SEC is idealized for a final purification step to remove contaminants (endotoxins, gDNA and RNA) from sc and oc pDNA isoforms (85).

1.4.3.2. Hydrophobic Interaction Chromatography

Hydrophobic interaction chromatography (HIC) is based on the hydrophobic characteristics of biomolecules, which promote reversible interactions with the hydrophobic groups of matrix ligands. To promote binding of the lysate components to the chromatographic matrix, a buffer with a high salt concentration is required. The elution of the molecules takes place gradually with decreasing salt concentration in the buffer, which weakens the biomolecules hydrophobicity (94). However, this technique presents disadvantages at industrial level, since a high salt concentration is associated with high cost and an environmental impact. Despite this disadvantage, HIC can

preserve the biological structure and activity of biomolecules. Parameters such as temperature, pH and salts influence the selectivity and retention capacity of HIC and can be optimized to improve the separation of biomolecules (95).

1.4.3.3. Reverse Phase Chromatography

Reversed-phase chromatography (RPC) is based on hydrophobic interactions between biomolecules and the polar stationary phase, requiring high salt concentrations in the binding step. The elution is mediated by the decrease in polarity of the stationary phase (93). However, this elution is performed with organic solvents, which are toxic, mutagenic and volatile, and can compromise the biomolecules integrity, being a problem for large scale purifications (85).

1.4.3.4. Anion Exchange Chromatography

Anion exchange chromatography (AEC) uses a positively charged stationary phase that allows the adhesion of negatively charged pDNA due to the presence of phosphate groups. The increase in salt concentration allows the elution of pDNA depending on the size of the molecules, whereby the greater the number of phosphate groups the greater the negative charge (86). However, the elimination of RNA, gDNA, proteins and endotoxins is hampered, since they have a similar affinity for pDNA, which causes co-purification (95,96). This selectivity problem makes pDNA purification more difficult to achieve in just one AEC step (96).

1.4.3.5. Affinity chromatography

Affinity chromatography (AC) allows separation due to the high selectivity between matrix ligands and biomolecules. The use of different types of interactions such as hydrogen bounds, ionic or hydrophobic interactions and van der Waals forces allow the separation of pDNA, RNA, gDNA and impurities, based on the physicochemical characteristics of each component of the cell lysate (86). AC allows purifications with high yields and relatively low costs, but ligands have some limitations, such as some fragility and low binding capacity (94). There are different types of AC such as immobilized metal affinity chromatography (IMAC), triple-helix affinity chromatography (THAC), amino acid-DNA and protein-DNA affinity chromatography (85). One of the great advantages of this type of chromatography is that it has the ability to separate pDNA isoforms, namely sc and oc isoforms (86).

1.5. Minicircle DNA

Despite the advantages presented by pDNA face to viral vectors, it also presents some limitations in regard to transfection efficiency and transgene expression. These limitations are associated with the size of the vector, with smaller plasmid sizes being better for reaching the nucleus; the topology of the vector, in which the sc isoform plays a key role from a therapeutic standpoint; and the content of the DNA vector (97).

To overcome these problems, the minicircular DNA molecule (mcDNA) has emerged as an innovative technology. The mcDNA is obtained through the recombination process of a plasmid mediated by specific recombination sites, obtaining two molecules: miniplasmid (mP) and mcDNA (98). Therefore, mcDNA is a small molecule, more stable, with high bioavailability, good capacity for transfection and transgenic expression, which highlights the potential therapeutic application of this biomolecule (99).

1.5.1. Minicircle DNA production

Minicircle DNA production is based on *in vivo* recombination of parental plasmid (PP) into mcDNA and mP (99). Recombination is initiated in the presence of an inducer, L-arabinose, which allows the expression of integrase ΦC31 and endonuclease I-SceI (100). The ΦC31 integrase will recognize the recombination sites and cleave them, while the I-SceI endonuclease will recognize the 32x SceI restriction site present in PP and mP (101,102). The *E. coli* strain ZYCY10P3S2T has an inducible system, pBAD/AraC, that allows the expression of these enzymes that will subsequently cleave the recognition sites, attP and attB, and degrade the unrecombined PP and mP (**Figure 9**) (100).

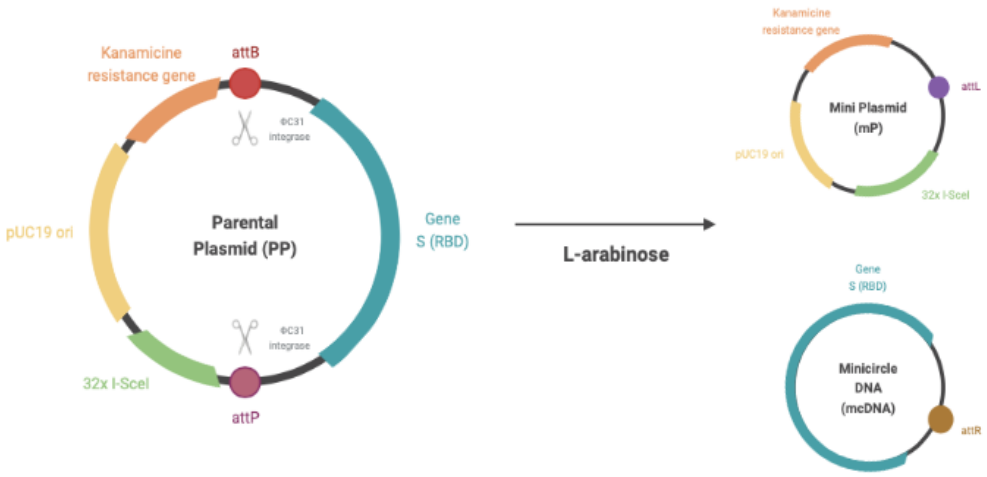

Figure 9 - Schematics of mcDNA recombination. Once L-arabinose is added PP recombines in mcDNA by ΦC31 integrase action, who recognize attP and attB recombination sequences. Adapted from (102).

1.5.2. Minicircle DNA purification

mcDNA is a novel technology with high potential for a therapeutic application, but at the end of the production process, the presence of other isoforms, non-recombinant PP and mP make mcDNA purification difficult. Thus, different mcDNA purification strategies have been explored (103).

Mayrhofer and colleagues developed a PP with an intrinsic sequence corresponding to a part of mcDNA after its recombination. This insert allows the isolation of mcDNA by AC through binding

to a specific ligand, the repressor of the lactose operon protein lactose. This method allowed a recombination efficiency above 99.5% with a purity above 98.5% (104). On the other hand, Hou *et al.* studied the improvement of triplex DNA technology to eliminate mcDNA impurities. They placed a pair of TriD-forming sequences to cleave the kanamycin resistance gene of PP. Subsequently the recombination products were incubated with biotinylated DNA oligonucleotides and the TriDs were removed by binding to streptavidin-coated magnetic beads (105). Another approach was described by Alves and colleagues that combines an enzymatic relaxation of the unrecombined PP and mP, via the nicking endonuclease Nb.BbvCI. Thus, unrecombined sc mPs and PPs are converted into oc isoforms, while sc mcDNA remains unchanged. Finally, the sample is purified through HIC allowing to obtain mcDNA free of impurities (106). Another approach is the use of a monolithic anion exchange column (CIM® DEAE-1). This strategy allowed to obtain pure mcDNA sc isoforms, successfully removing impurities from other isoforms and residues from *E. coli*. However the use of this monolithic column only allowed the recovery of 50% of the sc mcDNA (99).

The mcDNA can also be purified by SEC using a Sephacryl S-1000 matrix. This method allowed the recovery of 66.7% of mcDNA with 98.1% purity. SEC is a simple and effective strategy in the isolation of sc mcDNA, and allows a good separation between gDNA, PP, RNA and mcDNA (107). Despite this result, for higher molecular weight molecules, the separation by SEC becomes more complicated due to the low porosity of the matrix, which sometimes leads to the co-elution of molecules with larger sizes, for example gDNA. Thus, this technique has a great potential for the separation of small molecules, between 5 and 8.2 kbp (107), despite the time spent on this chromatography. Still, the presence of non-degraded PP and mP in the upstream part of the production process makes mcDNA purification difficult due to the similarity of sizes and isoforms (108).

The combination of monoliths with amino acid-based ligands appears to be a good strategy for nucleic acid purification. Lysine and its decarboxylated derivative, cadaverine, were explored as immobilised ligands on monolithic supports for the purification of the sc isoform of mcDNA. This cadaverine-modified support interacted more with mcDNA than the lysine-modified monolith at acidic pH and showed better selectivity, promoting the isolation of the mcDNA sc isoform. Moreover, the purity level was in accordance with the recommendations of the regulatory agencies. The results obtained show the potential of cadaverine-modified monolith as a viable and advantageous chromatographic strategy for the purification of the sc isoform of mcDNA, as it is a simple, practical and efficient approach (109).

1.6. Gene Delivery Systems

Nucleic acid-based therapies and vaccines have gained a lot of attention in biotechnology, pharmacology, and medicine. However, over the years, strategies to improve the efficacy and targeting of these molecules have been studied. The development of delivery systems, namely nanoparticles (NPs), allows the encapsulation and control of the biomolecules release, improves

tissue penetration and cellular uptake due to their nanoscale, and protects nucleic acids from intra- and extracellular barriers. These NPs can interact with the cell surface and when inside cells, deliver the respective nucleic acid (110). Delivery systems can be divided into viral vectors and non-viral vectors (111).

1.6.1. Viral Vectors

Viral vectors for the development of vaccines against COVID-19 have been explored due to their gene transfection efficiencies, specific delivery to target cells, and trigger robust immune responses, enhancing cellular immunity. Among the various viral vectors, adenovirus, poxvirus, lentivirus, measles virus, rhabdovirus and alphavirus type vaccines are the most studied to fight the pandemic (**Figure 10**) (112,113).

Adenoviruses have been firstly used as vectors for gene therapy. Recently, their use for DNA vaccines has been increasing. They are characterized as non-enveloped viruses with double-stranded DNA. So far, about 50 serotypes have been identified, being divided into 6 subgroups from A to F. However, only five serotypes can infect human cells (114). Adenoviruses are vectors of low pathogenicity, have a high capacity to express viral proteins, can deliver the viral genome inside the nucleus and have infection properties. Its infective capacity reaches both dividing and non-dividing cells and can carry DNA between 8-10 kbp (113).

Poxviruses are characterized as double-stranded DNA (dsDNA) enveloped viruses with a capacity to carry more than 30 kb of genetic information. Modified Vaccinia Ankara (MVA) is a highly attenuated strain derived from the vaccinia strain Ankara. Its modification allowed the 15% loss of its genome and the ability to replicate in mammalian cells (112,113).

Lentiviruses are widely used for cell and gene therapies as they allow gene transfer and integration for therapeutic benefit. They are capable of transfecting dividing and non-dividing cells, such as neurons, hematopoietic stem cells, and those of the immune system, namely T cells. They have the ability to transport genes up to 11 kbp (115).

Measles virus (MV) are non-segmented, negative sense, ssRNA enveloped viruses of ~16 kb. They possess a capacity to carry 6 kb of genetic material and being able to self-amplify cytoplasmic RNA (112,116).

Rhabdoviruses (RABV) are MV-like viruses with negative polarity ssRNA capable of carrying genes up to 6 kb. There are two well-studied RABVs, rabies virus, of the genus *Lyssavirus*, and vesicular stomatitis virus (VSV), of the genus *Vesiculovirus*. Both have genomes between 11-12 kbp, but differ in biology (112,117).

Alphaviruses are self-amplifying ssRNA viruses with a positive-strand polarity. They can carry 8 kbp. In recent years several vectors have been designed such as the Sindbis virus (SIN) expressing herpes simplex virus type 1 glycoprotein B (HSV-1-gB), the Semliki Forest virus (SFV) centered

on the expression of bovine viral diarrhea virus (BVDV) p80 (NS3) in BALB/c mice, and the Venezuelan equine encephalitis virus (VEE), based on the expression fusion of the *M. tuberculosis* antigens α-crystallin (Acr) and Ag85B (118).

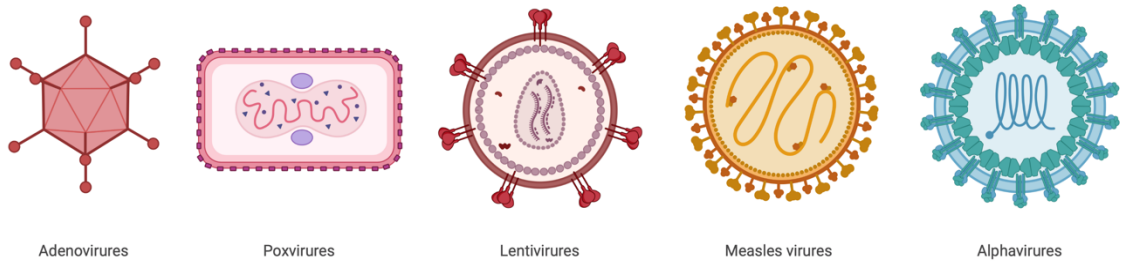

Figure 10 - Viral vectors examples used to deliver nucleic acids for COVID-19 vaccines.

1.6.2. Non-viral vectors

Despite the advantages that viral vectors may present, they have drawbacks including carcinogenesis, immunogenicity, broad tropism, limited DNA packaging capacity, and difficulty of vector production. It also presents limitations in terms of safety. Non-viral vectors have the potential to carry higher genetic payloads and are easier to synthesize compared to viral vectors. These vectors allow the delivery of DNA, mRNA, siRNA, and microRNA (miRNA) mimics (119). For DNA delivery, two methods can be applied: (i) chemical methods, in which transporters that undergo various chemical reactions are used; (ii) physical methods, by the action of physical forces that succeed in weakening and allowing it to permeate the membrane (120).

1.6.2.1. Physical Methods

Cells present an electric potential difference between the internal and external parts of the membrane, displaying a resting potential between -40 and -70 mV. If a cell is exposed to an external electric field, this will cause structural changes in the membrane as well as changes in its constituent molecules (121). The electroporation process provides small electrical pulses that favor the formation of transient pores in the cell membrane. During this period, the DNA crosses the destabilized membrane to the interior of the cell (122).

DNA delivery via microneedle allows direct injection of DNA into a target tissue via a micro-needle array. This injection allows a localized delivery and the molecule uptake is achieved by physical damages, when inserting the needles and the pressure required to inject the DNA (123).

Gene gun is a technology that permits delivery to target cells and tissue using biocompatible heavy metal accelerated particle carriers, such as gold, tungsten, or silver. This method reduces the amount of DNA used and is a more efficient dose-response strategy (120,122). This approach is often used for intramuscular, intradermal, and intratumoral DNA vaccination. The applications of gene guns are mainly limited to superficial tissues such as skin and muscle, as it can deliver DNA only at a depth between 100-500 μm (124).

Magnetofection consists of delivering DNA with magnetic particles that are controlled by an external magnetic field, allowing the efficiency of the therapy to be increased. It has several benefits such as higher efficiency, requiring a lower dose of nucleic acid, shorter delivery time, and the ability of transfection local and in a limited area (125).

Hydrodynamic gene delivery uses rapid injection of high-volume DNA solution, leading to momentary cardiac congestion, which allows an increase of hydrodynamic pressure in the inferior vena cava. Although, it provides effective gene transfer, its clinical application is restricted due to the high-volume injection (124).

Sonoporation uses ultrasound to briefly permeabilize the membrane to allow the passage of exogenous molecules into the cells. Although less effective than hydrodynamic injection and electroporation, sonoporation has been gaining interest due to its non-invasiveness, safety, simplicity, and flexibility compared to other non-viral vector delivery methods (123,124).

1.6.2.2. Chemical Methods

The use of cationic lipids has also been explored for the delivery of DNA. They are positively charged amphiphilic molecules with a similar molecular structure to natural lipids, the main difference being the cationic head group (119,126).

The use of cationic polymers for DNA delivery is associated with their potential to form polyelectrolyte complexes with nucleic acids. They mediate transfection by condensing nucleic acids, protecting them against enzymatic degradation and enhancing cellular uptake and endolysosomal escape. The most studied polymers are poly(ethyleneimine) (PEI), poly-L-lysine (PLL), poly[2-(N,N-dimethylamino)ethyl methacrylate] (PDMAEMA), chitosan (Ch) (127), poly(amidoamine) (PAMAM) (128), poly(β-amino ester) (PAE) (129), and β-cyclodextrin-containing polycations (119).

The advantage of using cationic polymers is to obtain smaller and usually water-soluble complexes. They promote protection to DNA against nucleases, improve the reach of target cells and permeate the cell membrane. An example of these cationic polymers is chitosan, which is able to increase immune efficiency by providing mucoadhesive characteristics (130). Coupling a cationic peptide to a cationic polymer can improve the uptake of the system by target cells as well as enhance its ability to penetrate the cell membrane. In this field, octaarginine (R8) is a small cationic peptide with the ability to penetrate the cell membrane (131).

1.6.3. Chitosan

Chitosan (Ch) is a cationic, hydrophilic polymer that results from the alkaline hydrolysis of chitin. It is characterized as a non-toxic and biocompatible polymer consisting of randomly distributed β-(1, 4)-linked d-glucosamine (deacetylated) and N-acetyl-d-glucosamine (acetylated) units (132). The degree of deacetylation influences its biodegradability, immunological activity, solubility, and physicochemical characteristics. Chitosan is classified according to its molecular

weight, with three main types: (i) low molecular weight (LMW) Ch (< 150 kDa), (ii) intermediate molecular weight Ch (150 - 700 kDa), and (iii) high molecular weight (HMW) Ch (700 - 1000 kDa) (133).

Chitosan is soluble in acidic media (acetic acid, citric acid, glutamic acid, aspartic acid, hydrochloric acid, lactic acid) and insoluble at neutral and alkaline pH values. In addition to pH, its solubility is influenced by the degree of deacetylation, molecular weight, and ionic strength of the solution. Under physiological conditions, it is easily digested by lysozymes and chitinases, produced by the normal flora of the intestine or existing in the blood. This polymer is in high demand by the pharmaceutical industry for drug delivery, and recently, the interest in its application in non-viral vector delivery has been increasing (130).

Since one of the main characteristics of Ch is its positive charge, it interacts very easily with nucleic acids through electrostatic interactions, allowing DNA condensation and protecting it from extra- and intracellular damage. Since the plasma and nuclear membrane are negatively charged, the interaction between the delivery system and the target cell improves transfection efficiency. Its natural mucoadhesive capacity promotes adhesion to negatively charged mucin through electrostatic attraction, hydrogen bonding, and hydrophobic effects (134). Thus, this polymer has promising capabilities for DNA vaccine delivery.

Chitosan nanoparticles (ChNPs) are obtained by ionotropic gelation (IG), precipitation with consequent polyelectrolyte complexes formation (PEC), spray drying, solvent evaporation, precipitation, and solution coating methods (135).

The IG technique is based on electrostatic interactions between the amine groups of Ch and a variety of negatively charged polyanions, such as tripolyphosphate (TPP), which is the method normally used to synthesize these NPs (132,135).

PEC consists of mixing oppositely charged polyelectrolytes resulting in electrostatic interactions in dependence on pH and external salt concentration. The formation of ChNPs occurs by the addition of DNA to a solution of Ch under magnetic stirring at room temperature (135,136).

Spray drying allows an emulsion, suspension, dispersion, or liquid to be transformed into a dry state by atomizing the product and dispersing it through a hot gas (137). Obtaining a dry inhalable powder allows delivery by the lung, through inhalation of the ChNPs (138).

The solvent evaporation method promotes the passage of a polymer emulsion in an aqueous phase, followed by the evaporation of the polymer-solvent precipitating from the polymer forming nanospheres (139).

The coagulation/flocculation technique is based on the destabilization of small, suspended colloids by the addition of coagulants. Destabilization allows the particles to aggregate to form larger flocs which are removed by sedimentation (140).

Coating with Ch solution is obtained by adding to already formulated NPs a coating of another chitosan solution. The NPs have a good morphology and a size between 75 and 85 nm. They have a good absorption and a good controlled release performance of the biomolecule (141).

1.6.4. Cell-penetrating peptides

Cell-penetrating peptides (CPPs) are short peptides of about 4 to 40 amino acids (aa), allowing access to the cell interior through different mechanisms, such as endocytosis, and promoting intracellular effects through these same peptides, or by covalently conjugated or unconjugated bioactive cargoes (142). CPPs comprise cationic, amphipathic, and hydrophobic peptides, have various functions for biomedical applications and are easily synthesized. Since they facilitate the cellular uptake of nucleic acids, they are ideal for application in delivery systems. In addition, CPPs help to prevent nucleation-mediated degradation before and after cellular uptake (143).

CPPs can be classified according to their chemical structure, protein nature, or the mechanism of cellular entry. Cationic CPPs consist of positively charged peptides containing several lysine and arginine residues. Studies have shown that a minimum of eight arginine residues increases the ease of cell penetration and that the greater the number of arginines, the better the penetration efficiency (144). For example, RALA (WEARLARALALHLARALALARA) and R8 (RRRRRRRRR) are some of the cationic CPPs explored in delivery systems (145,146). Amphipathic CPPs have parts of their structure alternating between polar (hydrophilic) and non-polar (hydrophobic) aa, and may have a positive, neutral, or negative charge. MPG (GLAFLGFLGAAGSTMGAWSQPKKKRKV) and Pep-1 (KETWWETWWTEWSQPKKRKV) allow efficient cell membrane guidance and favor the formation of hydrophobic interactions with proteins. Hydrophobic CPPs are composed mainly of non-polar aa (alanine, leucine, isoleucine, phenylalanine, tryptophan, methionine, and tyrosine). They show a high affinity for the hydrophobic domain of the membrane and can be translocated into the cell. C105Y (CSIPPEVKFNKPFVYLI) and Pep-7 (CSIPPEVKFNK)PFVYLI) are examples of hydrophobic CPPs (144,147).

Octa-arginine (R8) is a cationic CPP composed of eight arginines and has the ability to enhance the delivery of biomolecules (148), being explored to improve cell penetration (149). Several studies have used delivery systems modified with arginine peptides to promote the delivery of DNA, siRNA and proteins (150). R8 is taken up by cells by receptor-mediated endocytosis and by direct cell penetration (151). Peptides rich in arginine present several advantages, including: (i) good ability to transport exogenous proteins and membrane-permeable molecules, (ii) allow internalization within minutes, (iii) accumulate easily in the nucleus and in a concentrated form, (iv) have low sensitivity to endocytic inhibitors, and (v) are highly biocompatible (152).

The use of arginines conjugated with PEI NPs for DNA delivery has been studied and revealed promising results (146). Li and co-workers formulated arginine-chitosan (Arg-Ch)/DNA self-assembled NPs (AChNPs) and found an improvement in transfection efficiencies when compared with Ch/DNA self-assembled NPs (153).

1.7. Functionalized delivery systems

Targeted delivery of biomolecules is a method to reduce toxic side effects, increase treatment efficacy, increase specific localization, control bio-distribution, modulate pharmacokinetics, reduce dose requirements, and improve patient compliance. There are two ways to target nanosystems: passive targeting and active targeting. Passive targeting promotes an accumulation of drugs near the site of interest. This process is called the Enhanced Permeability Retention (EPR). Active targeting involves ligand-receptor interactions, promoted by ligands on the surface of the NPs, and specific receptors overexpressed on the target cell membrane. For instance, antigen-presenting cells (APCs) are considered the target cells for DNA vaccines (154).

Dendritic cells (DCs) are the APCs par excellence since they have a high capacity for antigen uptake and processing. When the antigen is taken up, they migrate to lymph nodes and present via MHC molecules in synergy with co-stimulatory signals leading to the expansion of specific T cells and B cells (155). In addition, DCs and macrophages express lots of lectins receptors on their surface and may be a target for DNA vaccine delivery systems. C-type lectin receptors (CLRs) can mediate binding to carbohydrates through one or more carbohydrate recognition domains (CRDs). Mannose specificity is associated with the aa sequence constituting the CRD. However, each mannose receptor's three-dimensional conformation and multimerization pattern also influences the specificity and interaction with mannose residues (156).

The CLRs of DCs include DC-specific ICAM-3 grabbing non-integrin (DC-SIGN), mannose receptor (MR) or CD206, Dectin-1 and -2, Mincle, Dendritic cell natural killer lectin group receptor-1 (DNGR-1) and DEC-205 are important receptors for the immune synapse and induction of cellular and humoral immunity. The combination of more than one receptor could work as adjuvant for a DNA vaccine, potentiating its effect (157,158).

1.8. Design of Experiments

Increasing the yield of mcDNA has been a challenge as the number of experiments to be performed to obtain results makes this an expensive and time-consuming process. Thus, the need to improve efficiency and decrease expenses and costs has led to the development of methods to generate smart experiments that provide maximum information with minimum experimentation (159). Design of Experiments (DoE) is a tool that allows analyzing and optimizing procedures relatively quickly and easily (160,161). Thus, this method allows a simultaneous variation of several parameters to combine several experimental conditions to improve a process (162). It also has the advantage of carrying out statistical analysis to verify the veracity of the results obtained.

There are different design models depending on the intended purpose. For example, Central Composite Face (CCF), Box-Behnken or Doehlert are models applied when the aim is to optimize a process. Looking at central composite design, it is the most suitable strategy in the process optimization, even though they require a higher number of experiments compared to Box-Behnken and Doehlert (159). The CCF design covers a larger design space, allowing for less error and better predictive models (162,163). This model combines two levels complete or fractional factorial designs with additional axial or stellar points and at least one point in the center of the experimental region. Thus it is the best option for a three-level full factorial design as it requires a smaller number of experiments while providing comparable results (164,165). To construct a CCF, it is necessary to specify the following points: (i) how many cubic points should be used, (ii) what will be the distance α of the axial paths from the center of the design and (iii) how many number of center points (160,165). It is a very efficient design to fit the second-order model (160). In **Figure 11** it is schematically represented the CCF design. Each point represents a combination of different values of several factors of an experiment. The black dots at the vertices of the cubes represent the factorial design points under evaluation. The central black dots that lie within the cube faces represent the star points (159). The red dot in the center of the cube represents the center point, which should be replicated in order to provide a measure of pure error and stabilize the variation of the predicted response (165).

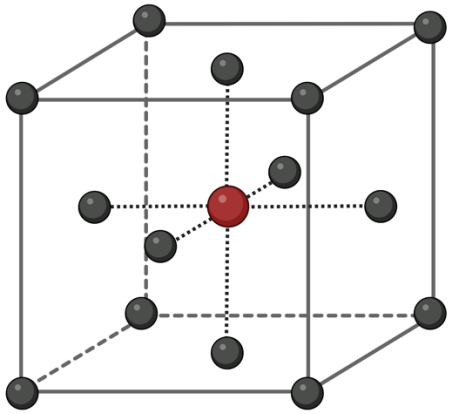

Figure 11 - Schematic representation of CCF design. Adapted from (165).

CCF design is the most suitable for optimizing procedures, since it uses the full quadratic model that is described as (n) = $2^{k-p} + 2k + cp$, where k is the factor number, p is the fractionalization number and cp is the number of central points required by the estimation curve (165).

Chapter 2

Aim

As COVID-19 is a global-concern and has a major socio-economic impact, it is necessary to develop strategies to combat, control, and prevent this disease. The first approved vaccine against COVID-19 is based on a messenger RNA (mRNA) that will give rise to the SARS-CoV-2 S-protein. This technology has shown that the use of nucleic acids has thus gained prominence in the pharmaceutical industry. DNA vaccines offer the same advantages as mRNA vaccines once they are more stable, easier to produce, and can encode more than one antigen. Minicircular DNA has recently emerged as an innovative vector due to the absence of bacterial genes, thus overcoming the limitations associated with the pDNA vector.

In line with this, the aim of the present project consisted in the cloning of a DNA vaccine with the S protein gene, optimizing the recombination process of PP into mcDNA by applying DoE and developing of binary and ternary delivery systems with chitosan and the R8-mannose complex to protect, transport and specifically deliver the mcDNA vaccine to APCs. Chitosan (Ch) is a cationic polymer known for its biodegradable, biocompatible, mucoadhesive and low cytotoxicity properties and has been vaguely explored in delivery systems. Complexation of tripolyphosphate (TPP) allows the creation of crosslinked stabilizing systems through electrostatic interactions between the positive charges of Ch and the negative charges of both TPP and DNA. The functionalization with R8 CPP aims to enhance the cell uptake and the specificity for the nuclear localization. The inclusion of mannose ligands intends the targeted delivery of mcDNA vaccine to APCs, since these cells overexpress mannose receptors on the surface. The systems were formulated with different ratios, varying concentrations of each system component. Physicochemical characteristics, structural properties, and stability of all systems were evaluated. Two cell lines, human fibroblasts (hFibro) and immature dendritic cells (JAWS II) were used in *in vitro* studies to evaluate the compatibility and transfection efficiency.

Chapter 3

Materials and Methods

3.1Construction of the parental plasmid

The plasmid pcDNA3-SARS-CoV-2-S-RBD-8his (Addgene, USA - Plasmid #145145) was used to amplify the receptor-binding domain (RBD; a.a. 333-529) of the S protein of SARS-CoV-2. The plasmid pMC.CMV-MCS-EF1-GFP-SV40Poly A (System Biosciences, USA) was used as the base to initiate the cloning process of the RBD gene sequence.

The polymerase chain reaction (PCR) technique was performed to amplify the RBD gene of the S protein of SARS-CoV-2. For each PCR reaction the following components were added: 0.75 µL MgCl2 (25 mM), 0.25 µL dNTPs (10 mM each), 1.25 µL PCR buffer, 100 ng DNA, 0.25 µL Taq DNA Polymerase (5 U/µL), making up to a final volume of 12.5 µL with water. Specific primers with XbaI and BamHI restriction sites were used, with a final concentration of 0.16 µM (FW: 5'-AAT CTA GAA TGA AGA CCA TCA TCG CCC T -3'; RV: 5'- ATG GAT CCT CAA TGA TGA TGG TGG TGG -3'). The reaction mixtures were then placed in the thermocycler programmed with the following steps: 5 min at 95 °C, 30 cycles of 30 seconds at 95 °C, 30 seconds at 60 °C and 1 minute at 72 °C, and finally 10 min at 72 °C. PCR products were analysed by 1% agarose gel electrophoresis. GRS Ladder 1kb (GRiSP, Portugal) was used as a DNA molecular weight marker.

After amplification of our gene of interest, enzymatic digests were applied to both the RBD fragment and the starting plasmid. The restriction enzymes XbaI (Takara Bio, USA) and BamHI (NZYTech, Portugal). For this purpose, a reaction mixture was prepared with 1 µL of the enzyme BamHI, 2 µL of 10x H Buffer and about 500 ng of RBD fragment or starting plasmid. The mixture was incubated for 1 hour at 37 °C in a thermal cycler. Before proceeding with 2nd digestion, dephosphorylation of the vector was performed using the enzyme alkaline phosphatase CIP (New England Biolabs, USA), and a reaction mixture was prepared with 1 µL of this enzyme, 2 µL of 10x NEB3 Buffer and about 500 ng of vector. The preparation was placed in the thermocycler for 1 hour at 37 °C. The 2nd digestion was performed with the restriction enzyme XbaI, following the same preparation and incubation performed for the 1st digestion with the restriction enzyme BamHI. Between each step, i.e., 1st digestion, dephosphorylation, 2nd digestion, the products obtained were always purified using the GRS PCR & Gel Band Purification kit (GRiSP, Portugal), according to the manufacturer's instructions. Each PCR product was analyzed by 0.6% agarose gel electrophoresis.

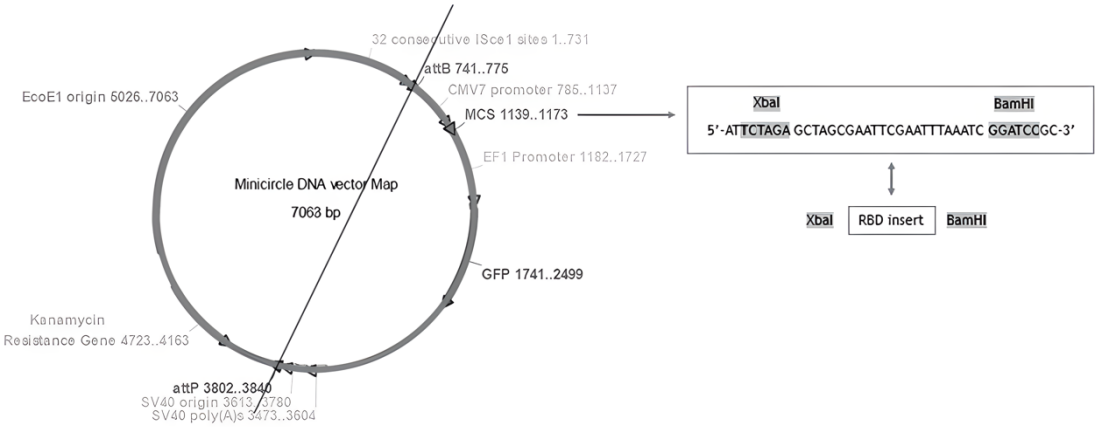

Figure 12 -Minicircle DNA vector map for PP-RBD construction and restriction enzyme map.

At the end of the cloning step, the vector concentration was set to 50 ng and the fragment concentration was varied for three different ratios, according to the following equation:

$$\text{fragment (ng)} = \frac{\text{vector (ng)} \times \text{ fragment size (pb)}}{\text{vector size (pb)}} \times \frac{\text{fragment}}{\text{vector}}$$

The three ratios tested were: 1:3, 1:6, and 1:9. Reaction mixtures were prepared with 1 µL of T4 DNA Ligase enzyme (NZYTech, Portugal), 2µL of 10x Buffer, 100 ng of vector and the amount of fragment calculated previously, making up with water until a final volume of 20 µL was reached. As recommended for cohesive binding, both the vector and the DNA insert were heated prior to binding for 10 min at 56 °C. The reaction mixtures were incubated for 16 h at 18 °C and subsequently, these mixtures were used to transform competent *E. coli* TOP10 and ZYCY10P3S2T cells.

The preparation of competent *E. coli* cells was performed according to the method described by Inoue (166). At first, *E. coli* TOP10 and ZYCY10P3S2T cells were inoculated on an LB-agar plate and incubated at 37 °C for 18 hours. Subsequently, the colonies are transferred to a 250 mL Erlenmeyer flask containing 25 mL of SOB medium (2% (w/v) tryptone, 0.5% (w/v) yeast extract, 8.56 mM NaCl, 2.5 mM KCl, 10 mM $MgCl_2$ and 10 mM $MgSO_4$). The Erlenmeyer flask was placed on an orbital shaker for 8 hours under 250 rpm shaking at 37 °C. Three 250 mL Erlenmeyer flasks containing 62.5 mL of SOB medium were then inoculated with 100 µL, 50 µL and 25 µL for the TOP 10 strain, and 25 µL, 10 µL and 5 µL for the ZYCY10P3S2T strain, respectively. These were placed on an orbital shaker overnight at 20 °C under 250 rpm shaking. The optical density at 600 nm (OD_{600nm}) was monitored until one of the Erlenmeyer flasks reached a value of approximately 0.55 and then transferred to a cold bath for 10 min to stop its growth. The cells were centrifuged at 2500 *g* for 10 m at 4 °C and the supernatant was discarded. The pellet was then resuspended in 20 mL of ice-cold ITB (Inoue Transformation Buffer) medium consisting of 55 mM $MnCl_2.4H_2O$, 15 mM $CaCl_2.2H_2O$, 250 mM KCl, 10 mM PIPES (0.5 M at pH 6.7). The cells were

centrifuged again at 2500 g for 10 min at 4 °C, discarding the supernatant. The pellet was again resuspended in 5 mL of ice-cold ITB. Subsequently, 375 µL of DMSO was added carefully, and the cells were placed on ice for 10 min. Finally, 100 µL of cells were transferred to cold sterile tubes, and these were rapidly frozen in liquid nitrogen, and finally stored at -80 °C.

Competent *E. coli* cells were transformed through heat shock. For this, a 100 µL aliquot of competent *E. coli* TOP 10 and ZYCY10P3S2T cells were placed on ice for 30 min. Then, thermal shock was performed by placing the cells at 42 °C for 1 minute and placed back on ice for another 2 min. Subsequently, 400 µL of SOB medium was added, and the cells were incubated at 37 °C for 1 hour on an orbital shaker under 250 rpm. Finally, 250 µL of culture was transferred to a LB-agar plate containing kanamycin (50 µg/mL) and incubated overnight at 37 °C.

3.2. Parent plasmid production

3.2.1. Bacterial growth conditions

E. coli ZYCY10P3S2T transformed with PP-RBD was inoculated on an LB-agar plate with kanamycin (50 µg/mL) and was incubated at 37 °C for overnight incubation. Subsequently, some colonies were inoculated in Terrific Broth (TB) medium, composed of 20 g/L tryptone, 24 g/L yeast extract, 4 mL/L glycerol, 0.017 M KH_2PO_4 and 0.072 M K_2HPO_4, supplemented with kanamycin (50 µg/mL). To verify the influence of temperature on PP amplification two temperatures, 37 and 42 °C, were tested. For this purpose, two 250 mL Erlenmeyer containing 62.5 mL of TB medium were prepared, one for each temperature, and both were placed on an orbital shaker under agitation of 250 rpm. Bacterial growth was monitored using the OD_{600nm}. When an OD_{600nm} between 2.4 - 2.6 was reached, a volume was transferred from the pre-fermentation to the fermentation to assure that the fermentation starts at an OD_{600nm} of 0.2. Finally, fermentation was continued under 250 rpm, and the growth is controlled until an OD_{600nm} between 5.0 - 6.0 is reached. After the fermentation process, cells were centrifuged at 3900 rpm at 4 °C for 10 min. The supernatant was discarded, and the pellets were stored at -20 °C for further analysis.

3.2.2. Preliminary assays for PP-RBD recombination

To evaluate the effect of TB medium on PP recombination into mcDNA, two production strategies were investigated: in the first strategy, fermentation medium was directly transferred to induction medium; and in the second strategy, cells were centrifuged to remove TB medium and then resuspended and transferred to induction medium. For samples that underwent centrifugation, 2000 rpm was applied for 20 min at room temperature to avoid any damage or induced stress to the cells. The pellet was then resuspended in 5 mL of Luria Broth (LB) medium, 25 g/L - supplemented with 0.04 M NaOH and 0.01% sterile L-arabinose and transferred to a 500 mL Erlenmeyer flask with 125 mL of LB medium containing 0.04 M NaOH to ensure pH 7.0 and 0.01% (w/v) L-arabinose. For both strategies, the induction process was carried out for 2 h at 32

°C with constant shaking at 250 rpm. After fermentation or induction, 10 mL of cells were recovered by centrifugation at 3900 rpm for 10 min at 4 °C and stored at -20 °C (**Figure 13**).

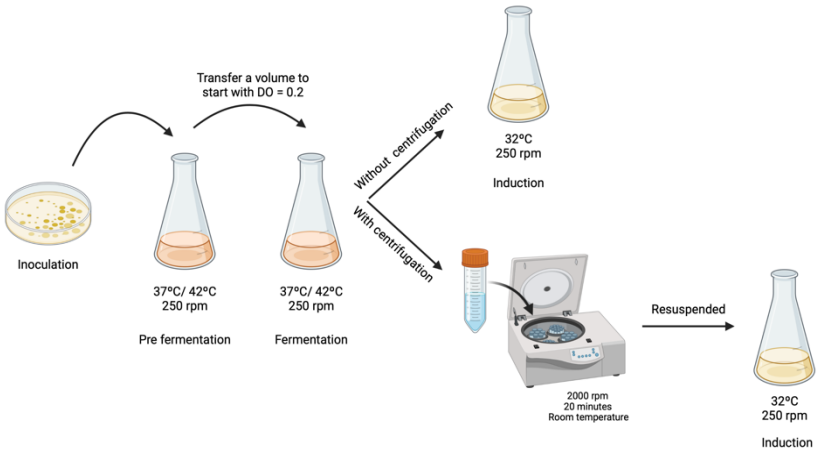

Figure 13 - Schematic representation of different procedures to start the induction step.

3.3. Design of Experiment

DoE was used to optimize the recombination of PP into mcDNA by applying the CCF model. For this purpose, three inputs A, B, and C (corresponding to induction temperature (°C), antibiotic concentration (µg/mL), and induction time (h), respectively) were selected, while the percentage of recombined mcDNA was the output to be maximized. The inputs were studied at three levels (-1; 0; +1). The software Design-Expert version 11 applied the CCF model and proposed a total of 17 experiments, considering three replicates of the central point. After performing all the experiments and evaluating the respective results, the results were included in the DoE software and statistical analysis was performed to validate the suitability of the model applied in the DoE.

The generalized equation of the second-order polynomial model used was (1):

$$Y = \beta_0 + \beta_1 X_1 + \beta_2 X_2 + \beta_3 X_3 + \beta_{11} X_1^2 + \beta_{22} X_2^2 + \beta_{33} X_3^2 + \beta_{12} X_1 X_2 + \beta_{13} X_1 X_3 + \beta_{23} X_2 X_3 \quad (1)$$

3.4. Recombination of the parental plasmid

3.4.1. Experimental conditions

As the goal is to increase the yield of mcDNA, the inputs that, according to the literature, have an influence on the recombination of PP into mcDNA were chosen. Therefore, 3 inputs were chosen: induction temperature, antibiotic concentration, and induction time. Precise ranges were defined for each parameter: induction temperature was varied between 30°C and 38°C; antibiotic concentration was varied from 0 µg/mL to 50 µg/mL; and finally, induction time was restricted

between 1 hour and 5 h. When applied in Design Expert, seventeen conditions were generated represented in **Table 2**.

Table 2 - Experimental conditions generated by DoE

Assay Number	Temperature (°C)	Antibiotic Concentration (µg/mL)	Induction Time (h)
1	30	50	1
2	30	0	1
3	30	25	3
4	30	50	5
5	30	0	5
6	34	25	1
7	34	0	3
8	34	25	3
9	34	25	3
10	34	25	3
11	34	50	3
12	34	25	5
13	38	50	1
14	38	0	1
15	38	25	3
16	38	50	5
17	38	0	5

3.5. Extraction, purification, and quantification of plasmid DNA and minicircular DNA

3.5.1. Extraction of PP-RBD

For PP-RBD extraction the NZYMaxiprep Kit (NZYTech - Genes and Enzymes, Portugal) was used to pre-purify plasmid DNA, according to the package insert provided by the manufacturer. After cell lysis, the plasmid DNA selectively bound to the anion-exchange columns and all contaminants, such as proteins, RNA, and low molecular weight molecules were eliminated. For the elution step, the positive column charge was neutralized by changing the pH to slightly alkaline conditions, and the plasmid DNA was eluted with a high salt buffer. After elution, the plasmid DNA was precipitated with 0.7 volumes of ice-cold isopropanol and incubated for 30 min on ice, and centrifuged at 16000 g for 30 min at 4 °C. After discarding the supernatant, the pellet was resuspended in 10mM Tris-HCl buffer (pH 8.0). The final PP-RBD samples were quantified

using a nanophotometer (Implen GmbH, Germany) and stored at -80 °C for further cell transfection assays.

3.5.2. Extraction of PP-RBD and mcDNA-RBD

The pellet obtained from the experimental conditions resulting from the DoE was extracted using a kit, Kit GeneJET Plasmid Miniprep (ThermoFisher - K0503) and following the respective package insert provided by the manufacturer. Briefly, the pellet was thawed and 250 µL of the resuspension solution was added and this was shaken vigorously in the vortex until complete dissolution of the pellet. Then 250 µL of the lysis solution was added, the Eppendorf was carefully homogenized and incubated for 5 min at room temperature. To stop lysis, 350 µL of neutralization solution were added, the Eppendorf was carefully homogenized and centrifuged at 12,000 g for 5 min. The supernatant was collected and transferred to a column and centrifuged for 1 min at 12,000 g. The eluate was discarded, and the column was washed twice with 500 µL of wash solution, centrifuged at 12,000 g for 1 min and discarding the eluate between each wash. After washing the column, it was centrifuged again at 12,000 g for 1 min so that the column matrix is dry. Finally, the column was placed in a new Eppendorf and 50 µL of the elution solution was added and incubated for 2 min at room temperature. Afterwards it was centrifuged at 12,000 g for 2 min and the mcDNA recovered in the Eppendorf was stored at -80 °C.

3.5.3. Modified Alkaline Lysis

The bacterial pellet resulting from the bioreactor fermentation was lysed with the intention of being further purified, it was lysed through a modified alkaline lysis. For this, the pellet was thawed and added 20 mL of solution A (50 mM glucose, 25 mM Tris-HCL, 10 mM EDTA at pH 8.0), shaking vigorously in the vortex until complete dissolution of the pellet. The contents were divided into two lysis tubes and 10 mL of solution B (200 mM NaOH, 1 % SDS (w/v)) was added in each, homogenizing carefully, and leaving to incubate at room temperature for 5 min. Next, 10 mL of solution C (3 M potassium acetate, pH 5.0) was added, again homogenizing carefully, and incubating on ice for 20 min. To remove cellular debris such as genomic DNA and proteins, the tubes were centrifuged twice at 20,000 g for 30 min at 4 °C. The supernatant was measured and divided between two lysis tubes for subsequent addition of 0.7 volumes of isopropanol, incubating on ice for 30 min after careful homogenization, to precipitate nucleic acids. The tubes were centrifuged at 16,000 g for 30 min and the supernatant was discarded. The resulting pellet was resuspended in 2 mL of Tris-HCl (pH 8.0). After resuspension, ammonium sulfate was added to a final concentration of 3 M (for 2 mL 0.793 g is required). Finally, centrifugation was performed at 16,000 g for 20 min at 4 °C to precipitate RNA and proteins, and the supernatant was recovered and stored at -80 °C for later use in molecular exclusion chromatography.

3.5.4. Purification of minicircular DNA by molecular exclusion chromatography

After modified alkaline lysis, mcDNA-RBD purification was performed in ÄKTA Pure equipment to promote the elimination of PP-RBD and RNA. A Sephacryl S-1000 SF gel filtration column (GE Healthcare Biosciences, Sweden) was used, with a volume of 106 mL, equilibrated with 10 mM Tris, 10 mM EDTA, 150 mM NaCl, at pH 7.0. 2 mL of sample from the extraction was injected and 3 mL fractions corresponding to the mcDNA peak were collected. The assay was performed at a flow rate of 0.3 mL/min at room temperature and absorbance was monitored at 260 nm. All collected fractions were subsequently desalted and concentrated to 200 µL in Vivaspin® concentrators.

3.5.5. Agarose gel electrophoresis

Agarose gel electrophoresis was performed to verify the integrity of DNA, both PP and mcDNA, and in order to verify the recombination of PP into mcDNA. It was prepared to 1% (w/w) to 100 mL of TAE 1x buffer (40 mM Tris, 20 mM acetic acid, 1 mM EDTA at pH 8.0) and supplemented with 1.2 µL of Green Safe. The gel was run at 150 V for 40 min before ultraviolet (UV) visualization. Uvitec Fire-Reader equipment (UVITEC, United Kingdom) was used to observe the gel.

3.6. Bioreactor culture

To initiate the bioreactor culture of *E. coli* ZYCY10P3S2T, cells were inoculated on LB-agar plates supplemented with kanamycin (50 µg/mL), and a pre-fermentation was performed following the same procedure performed in an Erlenmeyer flask. Then, the fermentation and induction processes were performed in 750 mL parallel mini bioreactors (Infors HT, Switzerland) with 250 mL of sterile TB or LB medium, respectively. The pH was kept constant in both media at 7.0 by automatic addition of 0.75 M H_2SO_4 and 12.5 % (v/v) NH_4OH via two peristaltic pumps. Dissolved oxygen (DO) was controlled by a cascade of three stirring levels between 250 and 950 rpm and mass flow between 0.2 and 2 vvm. The temperature was set at 42 °C for fermentation and for induction it was reduced to 30 °C. Throughout the process, foaming was manually controlled by the addition of an antifoaming agent (Antifoam A, Sigma-Aldrich) at 1 % (v/v) concentration. The parameters and their profiles were kept under constant control using IRIS software (Infors HT). In the fermentation process, the operational and experimental conditions previously established for the Erlenmeyer cultures were maintained, although various values of oxygen pressure (pO_2) were analyzed - 30 and 60 %. In turn, during the whole induction phase, the influence of pO_2 - 30, and 60 % -, concentration of L-arabinose inducer - 0.01 and 1% -, and induction time point - 5, 10, and 24 h - were evaluated. Cells were collected by centrifugation at 3900 rpm for 10 min at 4 °C, and then stored at -20 °C for further analysis.

3.6.1. High Performance Liquid Chromatography

High Performance Liquid Chromatography (HPLC) was performed to detect and quantify the consumption of L-arabinose during the induction procedure in the bioreactor. Initially, a calibration curve was performed, implementing a method similar to the one described by Pedro and collaborators (167). The chromatographic analysis was performed using an HPLC model

Agilent 1260 (Agilent, Santa Clara, CA, USA) equipped with an autosampler and quaternary pump coupled to a 1260 Infinity Refractive Index Detector (RID) (Agilent, CA, USA). The chromatographic separation was achieved on a cation-exchange analytical column Agilent Hi-Plex H (300× 7.7 mm i. d.; 8 μm), acquired from Specanalítica (Lisbon, Portugal). The analysis was performed at 50 °C with a flow rate of 0.5 mL/min using an isocratic elution with 0.005 M H_2SO_4. The mobile phase was filtered prior to the analysis under vacuum using a 0.2-μm pore nylon membrane and degassed for 15 min in an ultrasonic bath. A calibration curve was constructed with L-arabinose standards (0.001–1%), as indicated in **Equation (2)**:

$$y = 3 \text{ x } 10^6 x + 43265 \quad (2)$$

For the analysis of L-arabinose consumption, the collected samples were then centrifuged at 3900 rpm for 10 min, and the supernatant was recovered and filtered through a 0.22-μm cellulose-acetate filter.

3.7. Preparation of delivery systems

High molecular weight (HMW) chitosan with a molecular weight ranging from 200 - 500 kDa were obtained by Hepp Medical (Halle, Germany) and 5 kDa molecular weight chitosan was obtained by Sigma Aldrich Chemicals (St. Louis, MO, USA), and were prepared to a stock concentration of 1.0 mg/mL. TPP was obtained by GRISP (Porto, Portugal), and was prepared to a stock concentration of 1 mg/mL. R8 and R8-mannose, synthesized and characterized by Professor Swati Biswas (Department of Pharmacy, Nanomedicine Research Laboratory, Birla Institute of Technology & Science- Pilani) (**Figure 14**) in an established collaboration with our research group, was supplied as a freeze-dried desalinated powder and reconstituted with ultrapure water to a stock concentration of 0.5 mg/mL. Binary systems of Ch-TPP/PP-RBD and Ch-TPP/mcDNA-RBD, and ternary systems of Ch-TPP/R8-mannose/PP-RBD, Ch-TPP/R8/PP-RBD, Ch-TPP/R8-mannose/mcDNA-RBD and Ch-TPP/R8/mcDNA-RBD were prepared (**Table 3**). Their formulation occurred by dropwise addition for 1 min under stirring of 100 μL of TPP, containing 20 ng of PP-RBD/mcDNA-RBD, to 400 μL of chitosan for the binary systems. For ternary systems, the same procedure was performed and after the addition of TPP, 50 μL of R8/R8-mannose was added dropwise for 1 min. The systems were left to stand at room temperature for 30 min to allow the formation of complexes. Subsequently, the systems were centrifuged at 10,000 rpm at 4 °C for 20 min. To find out which would be the most suitable ternary system, the concentrations of TPP and R8 or R8-mannose were varied to obtain the best characteristics in terms of size (nm), surface charge (mV), and polydispersion index (PDI).

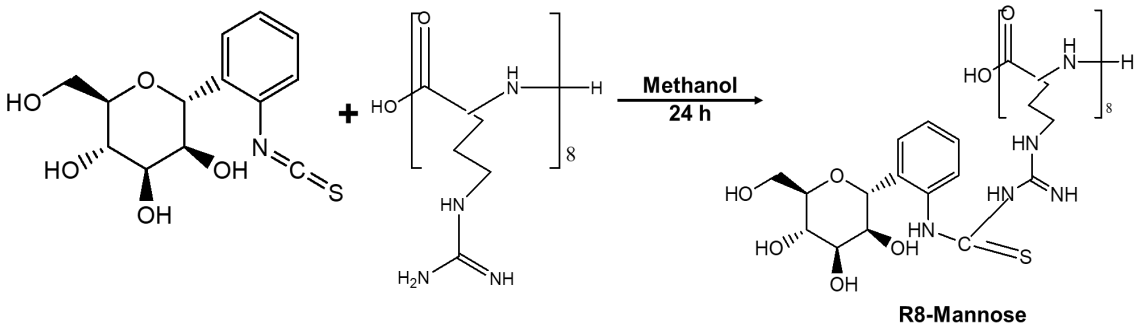

Figure 14 - Synthesis of R8-Mannose conjugate.

Table 3 - All experimental conditions for the formulation of ChNPs.

Chitosan Polymer	Chitosan Concentration (mg/mL)	TPP Concentration (mg/mL)	R8/ R8-Mannose Ratio
HWM Chitosan	0.51	0.25	0.5
			0.75
		0.50	1.0
			1.25
		0.75	2.5
5 kDa Chitosan	0.56	0.25	0.5
			0.75
		0.50	1.0
			1.25
		0.75	2.5

3.8. Determination of encapsulation efficiency

After systems centrifugation at 10,000 rpm for 20 min at 4 °C, the supernatant was collected for subsequent determination of encapsulation efficiency by electrophoretic mobility analysis on an agarose gel.

3.9. Size, zeta potential and polydispersity index

The average size and the surface charges (zeta potential) of nanoparticles were determined at 25 °C using the Zetasizer nano ZS device. For these evaluations, Dynamic Light Scattering (DLS) using a 633 nm He-Ne laser with non-invasive back scattering optics (NIBS) and electrophoretic

light scattering using a laser named M3-PALS (Phase analysis Light Scattering) were performed, respectively. After centrifugation of formulated systems, the resulting supernatant was discarded, and the pellet resuspended in 600 µL of Milli Q water. The mean values of sizes and surface potentials were obtained by 3 measurements ± standard deviation.

3.10. FTIR

To evaluate the presence of different components in the formulated systems was, Fourier transform infrared spectroscopy (FTIR) was used. Pellets resulting from various assays were resuspended in 10 µL of Milli Q water for further analysis. Spectra were acquired using a Nicolet iS10 FTIR spectrophotometer (Thermo Scientific, Waltham, MA, USA), operated in ATR mode (Smart iTR diamond ATR), at 120 scans with a spectral width between 4000 and 600 cm^{-1} and a spectral resolution of 32 cm^{-1}.

3.11. Scanning Electron Microscopy (SEM)

The morphology of the formulated systems was evaluated by scanning electron microscopy (SEM). After formulation of the systems, they were centrifuged, subsequently discarding the supernatant and the preserved pellet. The NPs were washed four times with 200 µL of Milli Q water and between each wash, centrifugation was performed at 9,500 rpm for 12 min. After the last wash, the pellet was resuspended in 40 µL of 2% tungsten and a 1:20 dilution of the sample in Milli Q water was performed. After this dilution, 10 µL were pipetted onto a round coverslip and allowed to dry "overnight" at room temperature. The next day, the samples were gold plated using the Emitech K550 spray layer (London, England).

3.12. Stability Assays

Stability assays aimed to assess the NPs stability upon incubation in cell culture medium. To mimic *in vitro* and *in vivo* conditions, several conditions were tested such as medium with or without FBS supplementation, and with or without trypsin. Thus, after the systems formulation, NPs were centrifuged and resuspended in 50 µL of DMEM/F-12 or MEM-α medium, supplemented or not with FBS and trypsin. Next, they were incubated at 37 °C for 6 h to verify the occurrence of DNA release and degradation. After 0, 3 and 6h, 20 µL were collected and the samples were evaluated by 1% agarose gel electrophoresis.

3.13. Cell lines and culture conditions

ATCC cell lines, the murine iDC, JAWS II, and human fibroblasts (FibH) were used in this study. JAWSii cells were cultured in Minimum Essential Medium α (MEM- α) and supplemented with 20% (v/v) heat-inactivated fetal bovine serum (FBS), 4 mM L-glutamine, 5 ng/mL GM-CSF and 1% (v/v) of an antibiotic mixture consisting of penicillin (100 µg/mL) and streptomycin (100 µg/mL). FibH were cultured in Dulbecco's Modified Eagle's Medium with Ham's F-12 Nutrient

Mixture (DMEM/F- 12) and supplemented with 10% (v/v) FBS, 2.438 g/L sodium bicarbonate and 1% (v/v) of an antibiotic mixture consisting of penicillin (100 µg/mL) and streptomycin (100 µg/mL). Cell growth was promoted at a temperature of 37 °C in a humid atmosphere containing 5% CO_2.

3.14. Cytotoxicity analysis

The cytotoxicity of systems was evaluated in JAWS II and FibH with the MTT (3-[4,5-dimethylthiazol-2-yl]-2,5-diphenyltetrazolium) assay. It is a colorimetric method that quantifies metabolically active cells. Both cell lines were plated at confluency at a density of 1×10^4 cells per well and grown at 37 °C in a humidified atmosphere with 95% O_2/5% CO_2.

24 h later and at least 12 h before the addition of NPs, the medium of the plate was changed to a simple medium to cause nutritional stress to the cells. 50 µL of each system under study were added to the wells of the plate. After 24 and 48 h of incubation, the redox activity was evaluated through the reduction of MTT. For this, 100 µL of MTT dye solution (1 mg/mL) was added to each well, followed by incubation for 4 h at 37 °C in a 5 % CO_2 atmosphere. After the period and incubation, the medium was removed from the wells and 100 µL of DMSO was added to dissolve the formazan crystals. The absorbance at 570 nm was measured using a Biorad Microplate Reader Benchmark. The relative cell viability (%) of samples related to the control wells was calculated by $[A]_{test}$ / $[A]_{control}$ × 100, where $[A]_{test}$ is the absorbance of the test sample and $[A]_{control}$ is the absorbance of the control sample. The statistical analysis was performed with two-way ANOVA followed by Tukey test (GraphPad Prism 9 software, GraphPad Software, San Diego, CA, USA). Statistical significance was accepted at a level of $p < 0.05$.

3.15. *In vitro* transfection studies

3.15.1. Plasmid labelling with FTIC

The PP was fluorescein isothiocyanate (FITC) labelled by adding 2 µg of PP, 2 µL of FITC and the labelling buffer was added up to a volume of 85 µL. Samples were placed under constant shaking for 4 h at room temperature and protected from light. After 4 h, 1 volume of 3 M NaCl (85 µL) and 2.5 volumes of 100% ethanol (212.5 µL) were subsequently added. The samples with the labelled PP were incubated at -20 °C overnight. The samples were then centrifuged at 4 °C for 30 min at 12000 g, the supernatant was discarded, and the pellet was washed with 75% ethanol. This procedure was repeated several times until the supernatant no longer had an orange color. After washing, the pellet was resuspended in 100 µL of TPP for further formulation of the nanoparticles.

3.15.2. Live cell imaging

To perform the Live cell imaging experiment, JAWS II cells were seeded at a density of 3 x 104 cells per well in "µ-Slide 8 Well" plates (Ibidi, Martinsried, Germany) and grown in 250 µL of complete medium at 37 °C in a humidified atmosphere with 5% CO_2. After 24 h and 12 h before transfection, the medium was changed to simple medium. Cells were transfected by adding 0.99

μg of PP, encapsulated in the different systems, binary and ternary, to each well. Prior to visualization in confocal microscopy, nuclei were labelled with 60 μL of DAPI. Cell internalization was visualized using the LSM710 laser scanning confocal microscope (Carl Zeiss, Germany) under a magnification of 63x.

Chapter 4

Results and Discussion

4.1. PP-RBD Cloning, Production and Recombination

4.1.1. Cloning of RBD Gene Sequence into PP Vector

The construction of a PP vector encoding the RBD of the SARS-CoV-2 S protein was initiated by PCR amplification with specific primers designed to amplify the RBD insert and using pcDNA3-SARS-CoV-2-S-RBD-8 as a template. The enzymes XbaI and BamHI were then used to recognize the restriction sites present on both the RBD insert and the PP vector, specifically the multiple cloning site (MCS), as schematically depicted in **Figure 14**, to acquire the same cohesive ends and facilitate the subsequent ligation step. After purification of the digested products, the resulting fragments were analyzed by 0.8% agarose electrophoresis. As shown in **Figure 15**, both the PP vector (7.0 kbp) and the RBD insert (640 bp) are integrated.

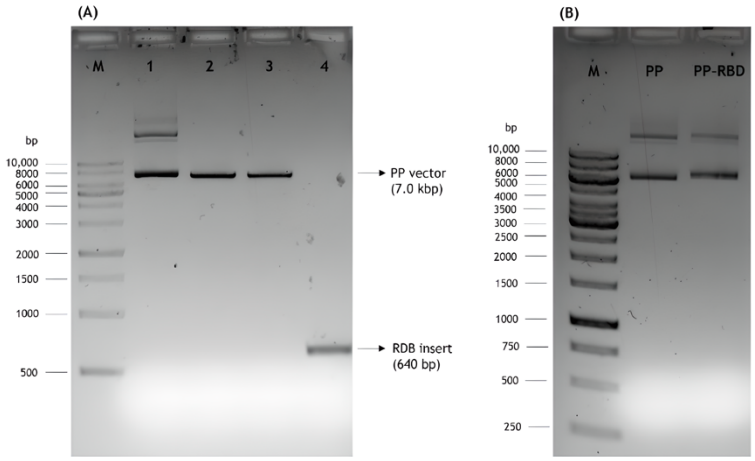

Figure 15 - Analysis of DNA fragments by agarose gel electrophoresis. **M**–molecular weight marker. **(A)** 1–PP vector; 2–PP vector digested with XbaI; 3–PP vector digested with XbaI and BamHI; 4–RBD insert digested with XbaI and BamHI. **(B)** Initial PP and PP-RBD vector.

The PP vector was dephosphorylated between digests to prevent self-ligation of the vector during the cloning step. Afterward, the DNA T4 ligase enzyme was used to perform ligation of the RBD insert in the PP vector. Three different molar ratios of vector:insert (1:3, 1:6, 1:10) were tested and competent *E. coli* TOP10 cells were heat shock transformed. The isolated colonies, previously grown on an LB-agar plate containing kanamycin (50 μg/mL), were used for PCR screening tests to verify the presence of RBD insert and a positive colony was selected to grow in a liquid medium. After purification of the pDNA, the vector was used to transform *E. coli* ZYCY10P3S2T, the minicircle producer strain, and an isolated colony was used for a PCR test to confirm the presence of the RBD insert. The positive colony was grown in liquid medium and the purified vector was

used for DNA sequencing to confirm alignment between the RBD insert and the cloned PP vector (**Figure 16**). The results revealed that the RBD insert was successfully cloned into the PP vector. The sequenced colony was used to create cryopreserved bacterial banks to explore the best conditions for production of PP-RBD and its recombination into mcDNA-RBD.

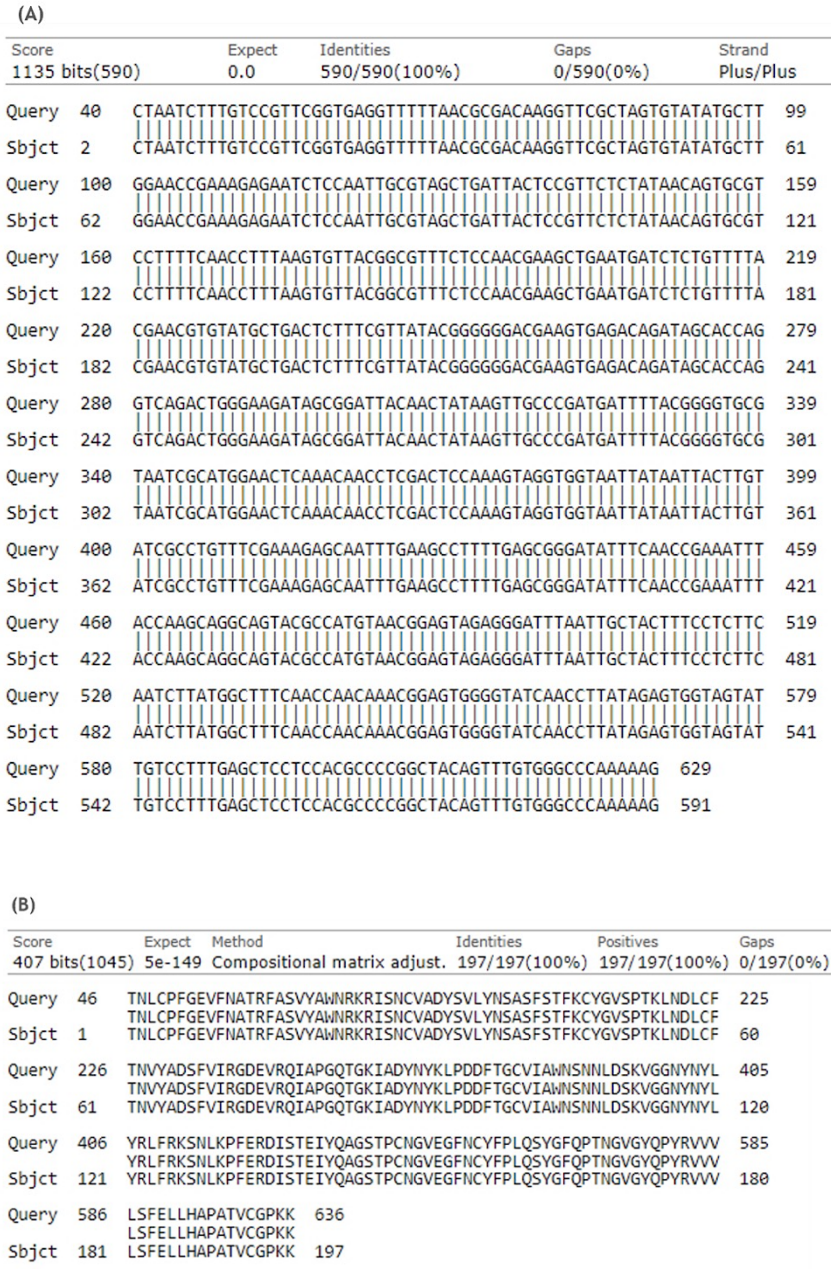

Figure 16 - Alignments of RBD-cloned PP vector and RBD sequence performed with basic local alignment search tool (BLAST). **(A)** Nucleotide alignment. **(B)** Amino acid alignment. The query corresponds to PP-RBD vector sequence and the subject is the sequence corresponding to RBD (aa 333-529) of S protein from SARS-CoV-2 (NCBI reference sequence: NC_045512.2 (21563..25384)).

4.1.2. PP Amplification and Recombination into mcDNA

Minicircles are small molecules that lack bacterial sequences, having great potential for therapeutic application as they exhibit low immunogenicity (168). However, an mcDNA vector shows higher transfection efficiency and transgene expression when compared to its PP precursor (101,169). Unfortunately, the full recombination of PP into mcDNA during the induction step was not fully effective, and the similarities between these biomolecules have a negative impact on the purification steps. Therefore, the goal is to optimize the recombination of PP into mcDNA.

As preliminary steps and to understand the influence of temperature on PP amplification two temperatures (37 °C or 42 °C) of the fermentation step were studied, as well as the best way to transfer the cells between these two steps (with or without centrifugation), thus allowing to assess its influence on both PP and mcDNA levels. At the end of each fermentation or induction step, cells were recovered, PP or mcDNA were extracted, and the results were analyzed by agarose gel electrophoresis. In lanes 1 and 2 of **Figure 16,** the influence of temperature on PP amplification during fermentation is shown. It is noticeable that PP remains intact at both fermentation temperatures (lanes 1 and 2, **Figure 16**). Nevertheless, when the temperature of 42 °C (lane 2) is applied the band density for PP is higher compared to the temperature of 37 °C (lane 1). In comparison with previous studies, it was reported that different fermentation temperatures could have an influence on the final pDNA yield. For example, using a genetically modified *E. coli* strain, fermentation at 42 °C increased the plasmid-specific yield compared to the yield obtained at 37 °C (170,171).

Then, the indirect influence of temperature on the PP-RBD recombination process was evaluated in the induction step combined with cell transfer in TB medium (without centrifugation) or without TB medium (after cell centrifugation). To this end, for both fermentation temperatures (37 °C and 42 °C), two 250 mL Erlenmeyer with 62.5 mL of TB medium followed different paths. In the first, a total of 62.5 mL of TB medium was added directly to a 500 mL Erlenmeyer flask with 62.5 mL of LB medium. In the second, the total 62.5 mL of TB medium was centrifuged, and the supernatant was discarded to recover the cells, which were resuspended in 125 mL of LB medium and placed in a 500 mL Erlenmeyer flask. These results are present in **Figure 17** and demonstrate an increase in mcDNA content when cell centrifugation was performed compared to experiments without centrifugation. This effect may be explained due to the glucose present in the TB medium being transferred to the induction step, and may be repressing the pBAD/AraC promoter, and consequently inhibiting PP recombination into mcDNA (172).

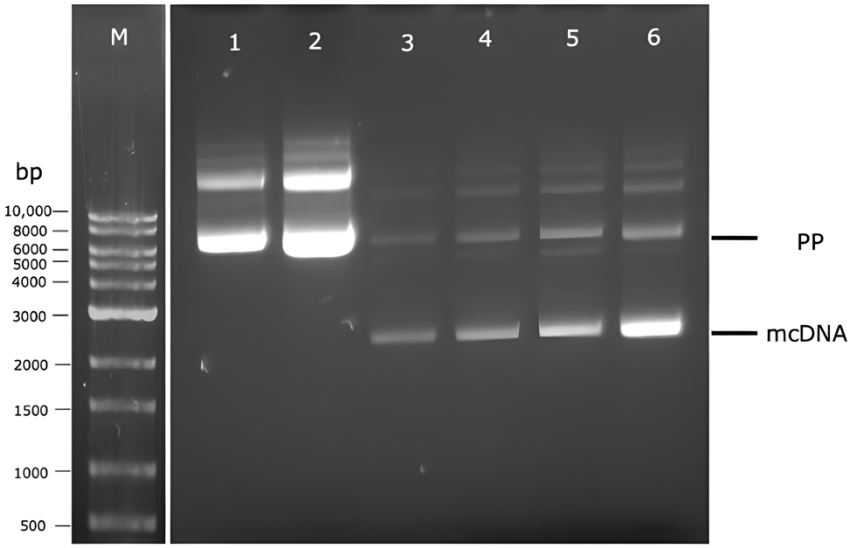

Figure 17 - Analysis of PP and mcDNA content, after fermentation or induction steps, by agarose gel electrophoresis. M– molecular weight marker. **(1)** Fermentation at 37 °C; **(2)** Fermentation at 42 °C; **(3)** Fermentation at 37 °C and induction without centrifugation; **(4)** Fermentation at 42 °C and induction without centrifugation; **(5)** Fermentation at 37 °C and induction with centrifugation; **(6)** Fermentation at 42 °C and induction with centrifugation.

Therefore, the best conditions for PP production and cell transfer to the induction step should be to conduct the fermentation step at 42 °C and to remove glucose from the TB medium by cell centrifugation before starting the induction process in LB medium containing L-arabinose. However, the conditions for recombination of PP into mcDNA during the induction step need to be explored and optimized. DoE is a suitable tool to rapidly achieve this goal using as few experiments as possible.

4.1.3. Inputs selected for DoE

There are several parameters that can influence the yield of PP recombination into mcDNA, ranging from the amount of PP achieved in the fermentation step, inducer concentration, antibiotic concentration, induction time, and induction temperature. However, previous studies conducted using orbital shakers explored different concentrations of L-arabinose and concluded that the increase in inducer concentration is not reflected in an increase in mcDNA yield (101). Given these assumptions, this work was initiated with the application of a standardized L-arabinose concentration of 0.01%, being the lowest concentration that revealed a very satisfactory mcDNA yield. Since the aim was to improve mcDNA yield, three parameters were considered paramount as DoE inputs. To define the input ranges, data from previously published works were considered (98,101,102).

The parameters were explored with a defined range of 0-50 μg/mL for kanamycin concentration, considering that 50 μg/mL has already been used in our research group (102); 1-5 h for induction time, as it is not recommended to prolong the induction step more than 5.5 h on an orbital shaker (98); and 30 °C - 38 °C for induction temperature, because the ΦC31 integrase and I-SceI

endonuclease enzymes involved in the recombination process had different optimal activity temperatures - 32 °C and 37 °C, respectively (173).

Since the stipulated output was the % recombined mcDNA and we only intend to explore points within predetermined ranges, the CCF design was chosen for this work. This model designed 17 experimental conditions with different input conditions, with three replicates of the central point, as shown in **Table 3**, **4** and **5**. For all conditions studied, cells were recovered and mcDNA was extracted and analyzed by agarose gel electrophoresis as illustrated in **Figure 18**. Bands from each lane were analyzed by band densitometry using Image Lab software, reflecting a percentage of recombined mcDNA from each experiment to be included in the DoE as the respective output. The percentage was calculated by the ratio between the relative density of the band corresponding to mcDNA and the relative density of the band corresponding to PP.

When analyzing the results obtained, the most promising conditions are 30 °C, without the presence of kanamycin, for 1 h (run 2 of **Table 4** and **Figure 18**), and 92.75% of recombined mcDNA was obtained. Over the time, a decrease in the amount of recombined mcDNA is noted. Furthermore, the presence of antibiotics during the time also causes a decrease in the yield of mcDNA. This decrease may be associated with some toxicity induced by the antibiotic, since the recombination process causes bacteria to lose antibiotic resistance, as the selection marker gene is degraded by the I-SceI endonuclease upon recognition of PP and mP.

Table 4 - Experimental conditions for 30ºC by DoE.

Assay Number	Temperature (°C)	Antibiotic Concentration (µg/mL)	Induction Time (h)	mcDNA Recombined (%)
1	30	50	1	81.43
2		0	1	92.75
3		25	3	58.73
4		50	5	26.98
5		0	5	47.85

Considering the conditions at 34 °C, the best recombination rate is reached only with 1 h of induction and 25 µg/mL kanamycin (run 6 of **Table 5** and **Figure 18**). Again, the amount of recombined mcDNA decreases over time and the presence of antibiotic negatively influences the mcDNA yield.

Table 5 - Experimental conditions for 34 ºC by DoE.

Assay Number	Temperature (°C)	Antibiotic Concentration (µg/mL)	Induction Time (h)	mcDNA Recombined (%)
6	34	25	1	57.78
7		0	3	22.60
8		25	3	42.01
9		25	3	41.24
10		25	3	40.95
11		50	3	28.55
12		25	5	23.40

Analyzing the kanamycin-free conditions for 1 h of induction at opposite temperatures (lanes 2 and 14), changes in mcDNA yields reveal that when the temperature increases, 30 °C to 38 °C, the recombined mcDNA decreases (92.75% to 38.84%). This indicates that low temperatures can be explained by the fact that the ΦC31 integrase has an optimal activity at low temperatures and the I-SceI endonuclease shows minimal activity under these conditions (173). It is also possible to minimize degradation of PP will occur prior to its recombination. When a duration of 5 h in the induction step is explored, without considering any other inputs, there are a gradual decrease in mcDNA yield. This phenomenon may reflect an increased metabolic stress that favors cell lysis and death during a prolonged induction phase, and the recombined mcDNA is degraded over time (98).

Table 6 - Experimental conditions for 38 ºC by DoE.

Assay Number	Temperature (°C)	Antibiotic Concentration (µg/mL)	Induction Time (h)	mcDNA Recombined (%)
13	38	50	1	43.40
14		0	1	38.84
15		25	3	21.56
16		50	5	16.51
17		0	5	18.68

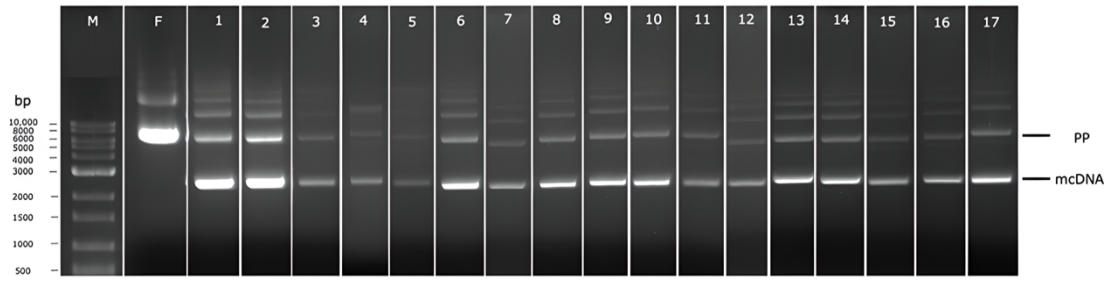

Figure 18 - Analysis of PP recombination into mcDNA by agarose gel electrophoresis. M–molecular weight marker. F-Fermentation at 42 °C. Numbers 1–17 correspond to each condition generated by DoE, as indicated in Table 1

4.1.4. Application and analysis of the model

Once all experiments proposed by the CCF design and the evaluation of results were performed, a statistical analysis was performed by the Design-Expert software. In **Table 7** are presented the statistical coefficients obtained for the % recombined mcDNA, which are used to understand if the statistical model generated from these experiments is valid and fits the data. Thus, R^2 represents the coefficient of determination, providing information about the fit of the statistical model output to the data (161). This value ranges between 0 and 1, being desirable when close to 1. As it is noticeable in **Table 7** the R^2 of the output is 0.9972, suggesting that the model fits the data. The adjusted R^2 represents the theoretical values to be fitted to the experimental data (160). The result shows a valid adjusted R^2 as it only decreased by 0.0035 compared to its R^2. The predicted R^2 provides information about the suitability of the model in predicting new data. The model presents a high predicted R^2 value (0.9762), thus highlighting the predictive power of this model. Finally, adequate accuracy allows the measurement of the signal-to-noise ratio (174). This parameter must be greater than four to indicate an adequate signal. According to **Table 7**, the ratio of 60.885 indicates an excellent signal and suggests that this model can be used to navigate the design space.

Table 7 - Statistical coefficients of mcDNA optimization.

Output	R^2	Adjusted R^2	Predicted R^2	Adequate Precision
% of mcDNA	0.9972	0.9937	0.9762	60.885

Observing all these coefficients, the quadratic model was chosen to proceed with the statistical analysis of this output. To further prove the validity of the DoE, ANOVA analysis was performed. In **Table 8** is represented the model significance for the output % of recombined mcDNA, including all the parameters used in this model, coupled with the corresponding lack of fit. A good valid model must present a significant value for the model (p-value < 0.05) and a non-significant value for the lack of fit (p-value > 0.05), thus suggesting the model data are significant and is suitable for the assay performed (174). According to **Table 8**, all the model values are significant

and do not present a significant lack of fit. Consequently, it can be confirmed that a good and valid statistical model was achieved for this output.

Table 8 - ANOVA analysis for response surface quadratic model for the % of recombined mcDNA. *p*-value < 0.05 is considered significant.

Source	Sum of Squares	dF	Mean Square	F Value	*p* Value
Model	6526.52	9	725.17	280.41	<0.0001
Temperature (A)	2520.16	1	2520.16	974.50	<0.0001
[Antibiotic] (B)	129.17	1	129.17	49.95	0.002
Induction time (C)	3268.14	1	3268.14	1263.73	<0.0001
AB	149.47	1	149.47	57.80	0.0001
AC	341.91	1	341.91	132.21	<0.0001
BC	33.13	1	33.13	12.81	0.0090
A^2	50.20	1	50.20	19.41	0.0031
B^2	0.88	1	0.88	0.34	0.5776
C^2	0.14	1	0.14	0.053	0.8244
Residual	18.10	1	2.59	–	–
Lack of fit	17.50	5	3.50	11.66	0.0808

To evaluate the main effects that each input presents towards the % of recombined mcDNA, a coded multiple regression equation was generated by Design-Expert software. In this equation, the signal behind each factor indicates a positive or negative effect in the response (164). In **Equation (2)** is presented the output regression equation, where A represents induction temperature (°C), B represents antibiotic concentration (µg/mL), and C represents induction time (h). Through the equation, it can be deduced that the induction temperature has a negative effect on the % of recombined mcDNA. As mentioned before, the temperature effect can be related to the temperature at which ΦC31 integrase has optimal activity [28]. Since ΦC31 integrase will be responsible for PP recombination into mP and mcDNA, and displays an optimal activity at low temperatures, the increase in this factor seems to be critical for the percentage of recombined mcDNA (175). The antibiotic concentration increment also has a negative effect on the output. During the induction phase, the endonuclease I-SceI will degrade the mP and unrecombined PP, which possess the antibiotic resistance gene and recognition sequence for this enzyme. After this digestion, the bacteria lose antibiotic resistance, and the presence of antibiotics in the induction medium will be a stress factor that can cause cell death. Finally, the induction time shows a negative effect which may indicate that the bacteria enter a state of stress and eventually die, and the recombined mcDNA is degraded (98).

$$\%\ \text{of recombined mcDNA} = +636.57 - 25.90\,A - 1.54\,B - 35.47\,C + 0.04\,AB + 0.82\,AC - 0.04\,BC + 0.27\,A^2 + 9.18 \times 10^{-4}\,B^2 - 0.06\,C^2 \quad (2)$$

After validation of the statistical model and understanding the effect that each factor has on the output, conditions of each input to reach the optimal point (maximizing the percentage of recombined mcDNA) were predicted. Design-Expert software suggested the combination of the induction temperature at 30 °C, the absence of antibiotics and 1 h of induction time, to obtain a % of recombined mcDNA between 88.72% and 95.50% of the confidence interval for the validation of the optimal point. These conditions were applied in three independent experiments and the average of the resulting outputs provided 93.87 ± 3.24 % of recombined mcDNA. This value is within the confidence interval provided by the Design-Expert software, where the output is considered valid, according to **Table 9**.

Table 9 - Predicted outputs for optimal point. CI–Confidence Interval.

Output	Predicted Mean	SE Mean	95% CI Low	95% CI High	SE Predicted	95% PI Low	95% PI High
% of recombined mcDNA	92.1131	1.43	88.72	95.50	2.15	87.02	97.21

Overall, with experimental design, the optimization of PP recombination process into mcDNA was successfully achieved. The induction temperature, antibiotic concentration, and induction time revealed important factors that strongly influence the output.

4.1.5. Scale up of the mcDNA Biosynthesis in Mini-Bioreactor

The culture of *E. coli* ZYCY10P3S2T is divided into two main phases, fermentation and induction. The fermentation phase allows to increase the PP yield associated with biomass production in these cultures. Besides having manipulated the temperature and centrifugation between production stages, the impact of different DO levels on cell growth was studied, which could maximize PP production in this initial phase and improve the final mcDNA yield. Looking at culture conditions explored by other research groups for pDNA fermentation in bioreactors, 30% pO_2 was the starting point (176–178). To understand the evolution of bacterial growth, samples of bacteria were taken every hour and monitored at OD_{600nm}, and the result revealed that cells reached a stationary phase after 6 h of fermentation (OD_{600nm} = 27.7 ± 0.1) (**Figure 19.A**). Subsequently, the pO_2 was increased to 60%, and after 6 h of fermentation, the cells reached an OD_{600nm} = 42.0 ± 0.8. Therefore, bacterial amplification using 60% pO_2 resulted in higher cell levels than those obtained at lower oxygen pressure. This bacterial growth of *E. coli* ZYCY10P3S2T using 60% pO_2 was characterized to determine the evolution profile during fermentation and was observed in a stationary phase between 5 and 6 h (**Figure 19.B**). Since the induction phase should be performed at the end of the exponential growth phase, in the following assays, induction was performed after 5 h of fermentation. When densitometry analysis was applied, it revealed that PP production was increased by a factor of 37.22 and 65.46 for 30 and 60% pO_2, respectively, compared to the results obtained under an orbital shaker. In agreement with previous studies, higher plasmid productivity and faster cell growth were obtained at higher DO concentrations (179,180).

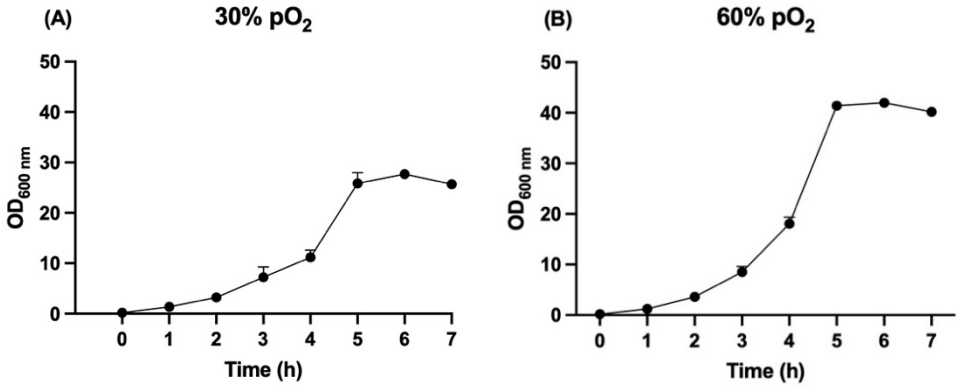

Figure 19 - Growth curve of *E. coli* ZYCY10P3S2T strain at 42 °C and using 30% (A) and 60% pO_2 (B) in bioreactor, respectively. Data are represented as mean ± S.D., n = 3.

Considering the increase of biomass in bioreactor, being eight times higher than the biomass obtained in the orbital shaker (OD_{600nm} of 42 and 5, respectively), the influence of L-arabinose concentration (0.01 and 1%) was evaluated in the induction step of the bioreactor to ascertain if a possible increase would be reflected in an increase of mcDNA levels. Thus, the optimized conditions for the recombination of PP into mcDNA obtained on the orbital shaker were first applied in the bioreactor induction step (temperature 30 °C, no antibiotic and 0.01% L-arabinose), applying 30% pO_2. For the same conditions, the concentration of L-arabinose was increased from 0.01% to 1%. Recombination of PP into mcDNA was increased by a factor of 60.86 and 61.19, respectively. On the other hand, the consumption of L-arabinose from the culture medium during these induction steps was evaluated resorting to the use of HPLC coupled to RID, using an Agilent Hi-Plex H cation exchange analytical column. For this purpose, a calibration curve was constructed with various L-arabinose standards (range 0.001 to 1%), as previously indicated in **Equation (2)**.

The results represented in **Table 10** showed that the ability of the method to detect L-arabinose, as well as its consumption, is most evident after 4 or 6 h of induction. However, despite the amount of L-arabinose consumed in the medium, the increment of mcDNA was minimal. Therefore, there is no need to supplement the medium with more L-arabinose inducer during the induction phase (181), and the L-arabinose concentration of 0.01% was established for future assays.

Table 10 - Determination of L-arabinose consumption during the bioreactor induction step.

Time (h)	Initial Concentration of L-Arabinose (%)	
	0.010	**1.000**
2	0.006 ± 0.0012	0.868 ± 0.0150
4	0.005 ± 0.0025	0.791 ± 0.0112
6	0.003 ± 0.0003	0.774 ± 0.0209
8	0.003 ± 0.0002	0.729 ± 0.0183
10	0.002 ± 0.0012	0.707 ± 0.0106

Finally, the influence of pO_2 was tested in the induction step of the bioreactor, being also explored 30 and 60%. The results showed that the recombination of PP into mcDNA was increased by a factor of 69.97 and 43.67, respectively, when compared to orbital shaker studies. This result suggests that the acceleration of biomass growth/amplification at 60% pO_2 did not favor the induction step, as occurred in the fermentation step. Probably, during the induction step, the increased cellular metabolism interferes with the time the cells require for the expression of ΦC31 integrase and endonuclease I-SceI and their action in PP recombination and mP degradation (98). Thus, the most favorable conditions for each stage of the bioreactor cultures were 60% pO_2 in the fermentation step during 5 h and 30% pO_2 for induction step, with 0.01% L-arabinose also during 5 h.

4.2. Nanoparticles formulation and characterization

4.2.1. Size, PDI and Zeta Potential

The HWM and 5 kDa Ch, are positively charged cationic polymers, known for their mucoadhesive, biocompatible and DNA-condensing properties (130,133). Once coupled to the TPP, complexes are created and stabilized by electrostatic bonds that allow ChNPs to fuse with the cell membrane (132,135). Functionalization of ChNPs with a CPP improves the system's uptake by cells (142). For instance, R8 is able to enhance cell penetration and consequently improve the delivery of biomolecules (148,149). The use of mannose ligands promotes targeted delivery of systems to APCs, namely DCs (157,158).

Previous studies have shown that Ch-TPP-based complexes allow good encapsulation of PP, these systems were a basis for the development and study of the systems proposed in this work (182). However, mcDNA encapsulation is not well described for these delivery systems, and a preliminary assay was conducted to compare the characteristics of the systems when PP and mcDNA are encapsulated. Examining **Table 11**, both HMW and 5 kDa systems show similar characteristics at the size (nm), PDI and zeta potential (mV) level. Another study by our research group found that HMW-TPP/PP systems had a size of about 125.28 nm, with a PDI of 0.228 and

a zeta potential of 30.1 mV. The 5 kDa systems had a size of 81.27 nm, a PDI of 0.257 and a zeta potential of 20.4 mV (182). Thus, all the system characterization assays were performed considering the encapsulation of PP, since this vector is of easy production and purification.

Table 11 - Size and zeta potential of Ch-TPP/ nanoparticles encapsulating PP and mcDNA. Values were calculated with the data obtained in three independent measurements (mean ± SD, n = 3).

Nucleic acid	Chitosan Polymer	Chitosan Concentration (mg/mL)	TPP Concentration (mg/mL)	Size (nm)	PDI	Zeta Potential (mV)
PP	HMW	0.51	0.25	119.83 ± 3.47	0.369 ± 0.01	27.6 ± 0.47
	5 kDa	0.56	0.42	75.42 ± 1.42	0.338 ± 0.01	22.4 ± 2.48
mcDNA	HMW	0.51	0.25	118.20 ± 1.22	0.301 ± 0.01	26.9 ± 3.41
	5 kDa	0.56	0.42	76.96 ± 0.66	0.261 ± 0.02	20.3 ± 4.36

To confirm that the systems under study allow an encapsulation and condensation of both PP and mcDNA, a 1% agarose gel electrophoresis was performed. The results obtained in **Figure 20** demonstrate that the studied systems, for both PP and mcDNA, allow the encapsulation and condensation of payload, since there is no presence of PP or mcDNA bands in lanes 1-4.

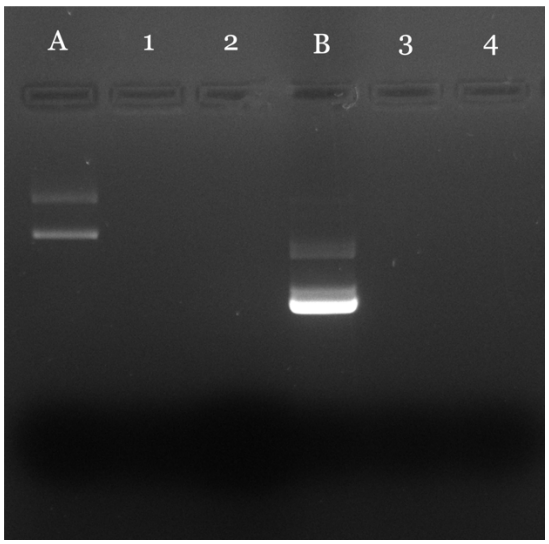

Figure 20 - Agarose gel electrophoresis of the supernatant of different formulated systems. Lanes **(A)** PP; **(1)** PP/HMW-TPP; **(2)** PP/5 kDa-TPP; **(B)** mcDNA; **(3)** mcDNA/HMW-TPP; **(4)** mcDNA/5 kDa-TPP.

Keeping the same binary systems, the variation of R8 and R8-mannose concentrations were explored (182). Hence, HMW concentrations of 0.51 and 5 kDa concentrations of 0.56 were used, conjugated with a TPP concentration of 0.25 and 0.41, respectively. For these systems, the R8 ratio 0.50, 0.75, 1.0, 1.25 and 2.5 was varied (145). After formulation through IG, samples were characterized in respect to their size, PDI and zeta potential. For HMW Ch polymer, the sizes ranged between 145.13 and 158.73 nm, PDI between 0.290 and 0.420, with a zeta potential

between 22.3 and 29.6 mV. It can be seen from **Table 12** that the charge of NPs increases with increasing R8 ratio. Considering the 5 kDa Ch polymer, the sizes were obtained between 95.60 and 108.70 nm, with PDI between 0.250 and 0.420, and zeta potential of 20.9 and 27.4 mV. As with HMW Ch, the charge of the systems with 5 kDa Ch increases in proportion to the increase of R8 (**Table 12**). This increase in surface charge of both systems can be associated with the increase in positive charges provided by the presence of R8 (octa-arginine peptide positively charged) that is able to neutralize the negative charges of the encapsulated DNA and TPP (146).

Table 12 - Size and zeta potential of Ch-TPP/R8 nanoparticles formulated for various R8 ratio. Values were calculated with the data obtained in three independent measurements (mean ± SD, n = 3).

Chitosan Polymer	Chitosan Concentration (mg/mL)	TPP Concentration (mg/mL)	R8 ratio	Size (nm)	PDI	Zeta Potential (mV)
HWM Chitosan	0.51	0.25	0.5	145.13 ± 1.63	0.290 ± 0.01	22.3 ± 0.92
			0.75	148.50 ± 3.39	0.400 ± 0.03	24.1 ± 1.04
			1.0	158.73 ± 1.51	0.420 ±0.01	26.0 ± 0.61
			1.25	149.63 ± 2.47	0.310 ± 0.04	27.9 ± 0.97
			2.5	145.93 ± 3.66	0.310 ±0.02	29.6 ± 1.04
5 kDa Chitosan	0.56	0.41	0.5	104.20 ± 3.99	0.250 ± 0.01	20.9 ± 1.34
			0.75	95.60 ± 3.25	0.370 ± 0.06	24.3 ± 1.30
			1.0	104.17 ± 1.81	0.370 ± 0.01	24.9 ± 0.96
			1.25	108.70 ± 2.65	0.420 ± 0.04	26.6 ± 0.96
			2.5	103.40 ± 1.55	0.400 ±0.02	27.4 ± 0.32

Being one of the goals the formulation of systems with R8-mannose, the size, PDI and zeta potential of systems with R8-mannose were also evaluated. As described above, HMW concentrations of 0.51 and 5 kDa concentrations of 0.56 were used, conjugated with a TPP concentration of 0.25 and 0.41, respectively. In addition, the R8-mannose ratio 0.50, 0.75, 1.0, 1.25 and 2.5 was varied (145). Once again, after formulation through IG, the samples were characterized according to their size, PDI and zeta potential. For HMW Ch polymer, the sizes ranged between 118.38 and 125.33 nm, PDI between 0.305 and 0.446, with a zeta potential between +21.4 and +29.7 mV. It can be seen from **Table 13** that the charge of NPs increases with increasing R8-mannose ratio. Considering the 5 kDa Ch polymer, the sizes were obtained between 77.38 and 116.03 nm, with PDI between 0.250 and 0.419, and zeta potential of 21.4 and 27.7 mV. As with HMW Ch, the charge of the systems with 5 kDa Ch increases in proportion to the increase

of R8-mannose (**Table 13**). Likewise, the increase in surface charge of both systems will be associated with the increase in positive charges provided by the presence of R8-mannose (146).

Table 13 - Size and zeta potential of Ch-TPP/R8-mannose nanoparticles formulated for various R8-mannose ratios. Values were calculated with the data obtained in three independent measurements (mean ± SD, n = 3).

Chitosan Polymer	Chitosan Concentration (mg/mL)	TPP Concentration (mg/mL)	R8-mannose ratio	Size (nm)	PDI	Zeta Potential (mV)
HWM Chitosan	0.51	0.25	0.5	125.00 ± 9.70	0.436 ± 0.02	21.4 ± 3.15
			0.75	118.83 ± 1.65	0.336 ± 0.05	24.0 ± 4.70
			1.0	120.37 ± 2.95	0.428 ±0.03	28.2 ± 2.02
			1.25	123.15 ± 0.64	0.446 ± 0.01	29.2 ± 3.04
			2.5	121.33 ± 0.42	0.305 ±0.01	29.7 ± 0.60
5 kDa Chitosan	0.56	0.41	0.5	107.97 ± 3.31	0.381 ± 0.02	21.4 ± 1.14
			0.75	116.03 ± 2.35	0.419 ± 0.05	21.4 ± 1.56
			1.0	77.38 ± 1.25	0.250 ±0.01	22.8 ± 2.63
			1.25	95.65 ± 1.74	0.352 ± 0.05	26.5 ± 1.98
			2.5	87.51 ± 1.40	0.310 ± 0.02	27.7 ± 1.45

For the tested combinations, the encapsulation efficiency of the systems was evaluated by 1% agarose gel. The results obtained in **Figure 21** demonstrate that the studied systems, with R8 and R8-mannose, allow the encapsulation and condensation of PP, since there is no presence of PP bands in lanes 1-20.

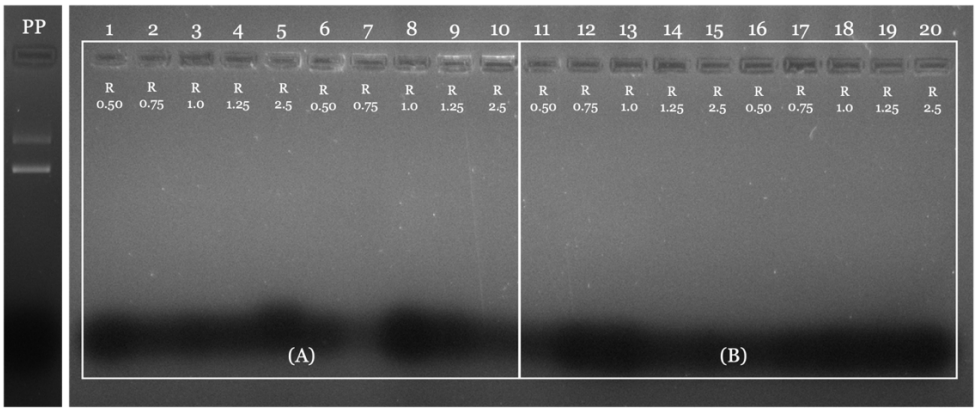

Figure 21 – Agarose gel electrophoresis of the initial PP sample **(PP)** and the supernatant of the different formulated systems. **(A)** systems with R8 – lanes **(1-5**) HWM-TPP/R8; lanes **(6-10)** 5 kDa-TPP/R8. **(B)** systems with R8-mannose – lanes **(11-15)** HWM-TPP/R8-mannose; lanes **(16-20)** 5 kDa-TPP/R8-mannose.

Looking at the results in **Tables 12** and **13**, together with **Figure 20**, the addition of R8 or R8-mannose shows similar characteristics at the size and PDI level. The trend of increasing charge with increasing N/P ratio is seen with both R8 and R8-mannose. For resources reasons, the rest of characterization tests were performed with R8-mannose.

As it was possible to verify in results obtained in **Table 12** and **Table 13**, the zeta potential of the NPs increases with the R8-mannose ratio. Next, the variation of the TPP concentration in the system was explored to verify whether it favors the binding of more R8-mannose to the system. For this, the R8-mannose ratio was set at 2.5 and the TPP concentration was varied between 0.25, 0.50 and 0.75. Subsequently, samples were analyzed for size, PDI and zeta potential. Looking at the results in **Table 14**, HMW showed sizes between 124.60 and 180.60 nm, a PDI between 0.261 and 0.343 with a zeta potential between 33.70 and 45.50 mV. For 5 kDa, the sizes recorded are between 80.90 and 113.10 nm, a PDI between 0.248 and 0.344, with a zeta potential between 27.70 and 30.90 mV. Considering these results, the increase of the TPP concentration, associated with the increase of negative charges available in the system, favored the binding of R8-mannose and improved the charge to + 15 mV for HMW and + 10 mV for 5 kDa.

Table 14 - Size and zeta potential of Ch-TPP/R8-mannose nanoparticles formulated for various TPP ratios and R8-mannose ratio of 2.5. Values were calculated with the data obtained in three independent measurements (mean ± SD, n = 3).

Chitosan Polymer	Chitosan Concentration (mg/mL)	TPP Concentration (mg/mL)	R8-mannose ratio	Size (nm)	PDI	Zeta Potential (mV)
HWM Chitosan	0.51	0.25	2.5	132.10 ± 0.59	0.343 ± 0.04	33.70 ± 1.46
		0.50		124.60 ± 1.40	0.261 ± 0.02	40.10 ± 3.29
		0.75		180.60 ± 3.56	0.261 ± 0.02	45.50 ± 2,08
5 kDa Chitosan	0.56	0.25	2.5	113.10 ± 9.77	0.248 ± 0.01	27.70 ± 0.61
		0.50		90.87 ± 9.29	0.344 ± 0.10	29.60 ± 0.60
		0.75		80.90 ± 0.30	0.329 ± 0.02	30.90 ± 0.61

Considering that the R8-mannose ratio of 2.5 would not bind all to the system, the use of half the ratio, 1.25, was studied. Keeping the same conditions tested in **Table 14** changing only the N/P ratio, the samples after formulation were evaluated for their size, PDI and zeta potential. Looking at **Table 15**, for HMW, the sizes vary between 135.0 and 167.90 nm (124.60 - 180.60 nm, **Table 14**), the PDI varies between 0.243 and 0.306 (0.261 and 0.343, **Table 14**) and with a zeta potential between 34.10 and 43.20 mV (33.70 and 45.50 mV, **Table 14**). For 5 kDa, the systems displayed sizes between 84.77 and 112.60 nm (80.90 and 113.10 nm, **Table 14**), PDI between 0.253 and 0.341 (0.248 and 0.344, **Table 14**), with a zeta potential between 30.10 and 31.20 mV (27.70 and 30.90 mV, **Table 14**). It can be seen that varying the N/P ratio did not induce a

difference in either the size, PDI or zeta potential of the system. Another study based on Ch systems with R8 investigated what effect increasing the R8 ratio would have on the characterization of the systems. They found that the increase in the ratio did not reflect a proportional increase in the zeta potential of the system (183). Considering these values, differences between the R8-mannose ratio 1.25 and 2.5 are not very disparate, so the ratio 1.25 was defined as the ideal ratio and was applied in all subsequent assays.

Table 15 - Size and zeta potential of Ch-TPP/R8-mannose nanoparticles formulated for various TPP ratios fixed R8-mannose ratio of 1.25. Values were calculated with the data obtained in three independent measurements (mean ± SD, n = 3).

Chitosan Polymer	Chitosan Concentration (mg/mL)	TPP Concentration (mg/mL)	R8-mannose ratio	Size (nm)	PDI	Zeta Potential (mV)
HWM Chitosan	0.51	0.25	1.25	135.0 ± 5.62	0.306 ± 0.02	34.10 ± 1.16
		0.50		135.80 ± 0.25	0.253 ± 0.01	41.00 ± 2.29
		0.75		167.90 ± 0.68	0.243 ± 0.01	43.20 ± 1.31
5 kDa Chitosan	0.56	0.25	1.25	112.60 ± 3.17	0.341 ± 0.04	30.10 ± 0.60
		0.50		84.77 ± 0.38	0.253 ± 0.01	30.30 ± 1.57
		0.75		85.43 ± 2.77	0.291 ± 0.03	31.20 ± 0.57

To verify that the changes in TPP concentration did not affect the encapsulation efficiency of the systems, an electrophoresis study was performed considering a 1% agarose gel. The results obtained in **Figure 22** demonstrate that this variation did not alter the capacity of DNA encapsulation and condensation, since there are no PP bands in the 1 - 12 lanes.

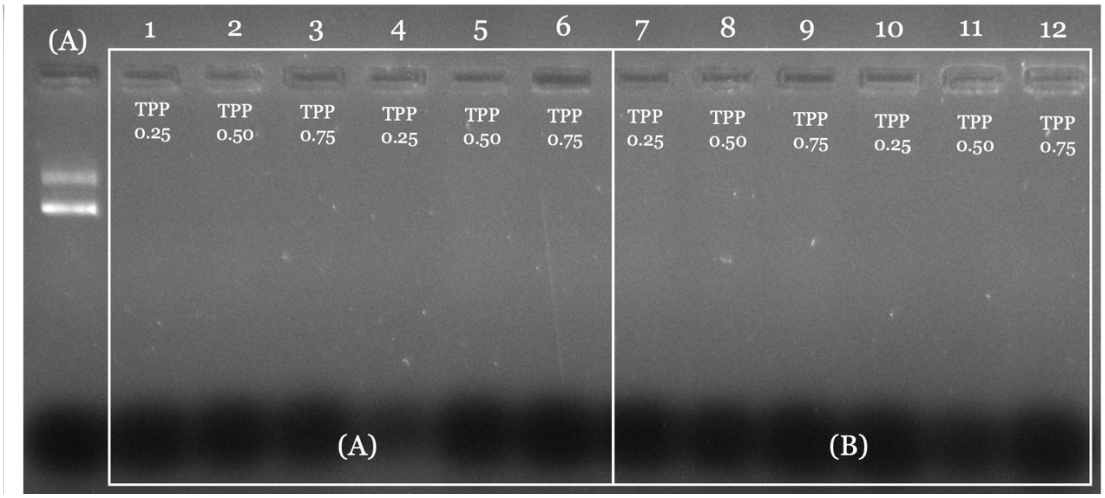

Figure 22 - Agarose gel electrophoresis of the initial PP sample **(A)** and the supernatant of the different formulated systems. **(A)** Systems with R8-mannose 1.25 – lanes **(1-3)** HMW-TPP/R8-man/PP; lanes **(4-6)** 5 kDa-TPP/R8-man/PP. **(B)** Systems with R8-manno 2.5 – lanes **(7-9)** HM-TPP/R8-man/PP; lanes **(10-12)** 5 kDa-TPP/R8-man/PP.

Analyzing the characterization results, it is possible to establish which are the most suitable systems to progress with the following tests. Thus, the system with HMW that exhibits the best potential to be applied in the following assays is the system conceived by using a concentration of 0.50 of TPP and a ratio of R8 and R8/mannose of 1.25. For the 5 kDa, the best system is obtained when adding 0.75 TPP and a ratio of R8 and R8-mannose of 1.25. For the following tests, these were the systems studied.

4.2.2. FTIR

Aiming to verify the presence of all components of formulated NPs, the FTIR technique was applied on the individual components and after the systems formulation. The spectra of pDNA, HMW Ch, 5 kDa Ch, TPP, R8, R8-mannose, HMW-TPP/R8/PP, HMW-TPP/R8-man/PP, 5 kDa-TPP/R8/PP and 5 kDa-TPP/R8-man/PP are shown in **Figure 23**. All spectra were analyzed between 4,000 and 600 cm^{-1}.

Regarding the pDNA spectrum, the peak in the region between 1700 – 1500 cm^{-1} corresponds to the nitrogenous bases, the peak near 1116 cm^{-1} is characteristic of the ribose vibration (C-C sugar) and at 944 cm^{-1} indicates the presence of pDNA (184). For HMW and 5 kDa Ch polymers, despite having different molecular weights, characteristic peaks are the same. Thus, the region between 3584 - 3328 cm^{-1} is related to N-H and O-H stretching vibrations as well as intramolecular hydrogen bonds. The zone between 2911 - 2880 cm^{-1} corresponds to the symmetric and asymmetric stretching vibrations. Bands between 1581 and 1544 cm^{-1} are characteristic of the asymmetric stretching of the C–O–C bridge (185). Observing the spectrum of TPP, it shows peaks at 1214 cm^{-1} (P-O stretching vibration), 1084 cm^{-1} (symmetric and asymmetric stretching vibrations in the PO_2 group), 973 cm^{-1} (symmetric and asymmetric stretching vibrations in the PO_3 group) and 908 cm^{-1} (asymmetric stretching of the P-O-P bridge) (186,187). Considering the spectrum of R8, the characteristic peak of arginine is near 1463 cm^{-1}. At 1678 cm^{-1} corresponds to

elongation of guanidine N=C and carbonyl C=O. Bands between 1353 and 1294 cm^{-1} are related to C(O)-O and N-C stretching, respectively (131). For R8-mannose, peaks are the same as in the R8 spectrum, with the addition of a peak at 1097 cm^{-1} of the C-O vibration of mannose (188,189). Spectra of conjugated systems, HMW-TPP/R8 and 5 kDa-TPP/R8 present peaks at 1709 cm^{-1} corresponding to N=C guanidine stretching (proving the presence of R8), at 1413 cm^{-1} demonstrating N-O-P stretching vibrations (evidencing the presence of TPP crosslinked with the Ch amines) (187,190). For HMW/TPP/R8-mannose and 5 kDa/TPP/R8-mannose, also present the same peaks as the previous systems and also observed at 1279 cm^{-1} reflecting the C(O)-O and N-C stretching and the peak near 1019 cm^{-1} corresponding to the presence of mannose.

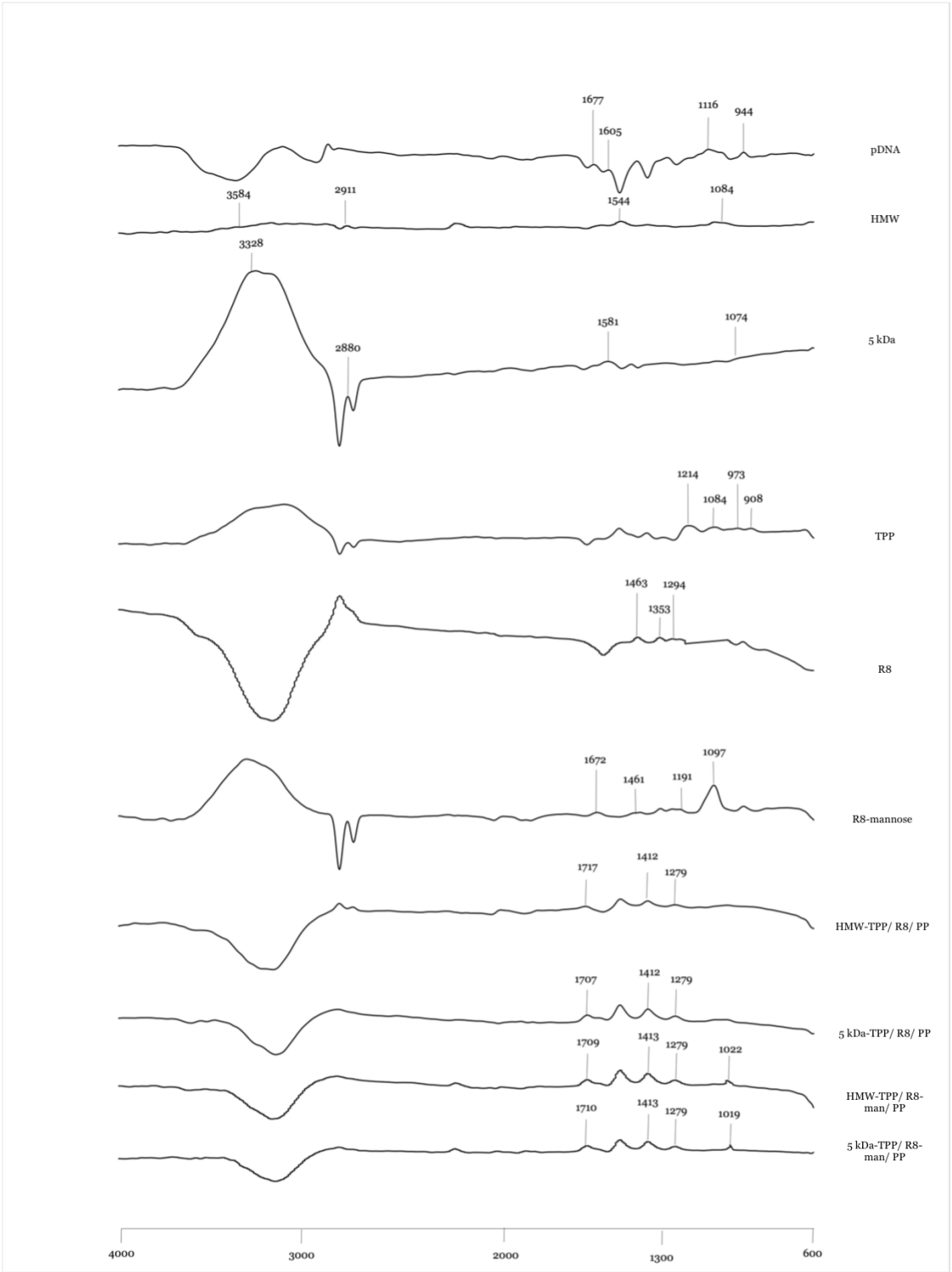

Figure 23 - FTIR spectra (Absorbance versus Wavenumbers) of pDNA, HMW, 5 kDa, TPP, R8, R8-mannose, HMW-TPP/R8/PP, 5 kDa-TPP/R8/PP, HMW-TPP/R8-man/PP, 5 kDa-TPP/R8-man/PP nanoparticles.

4.2.3. SEM

The morphology of Ch Nps was analysed by scanning electron microscopy. **Figure 24** shows images of the developed carriers. It can be seen that the NPs formed exhibit a spherical shape, which makes them suitable for a cell internalization process. Previous studies had shown that ChNPs present a spherical shape (182). It has also been found that the spherical morphology of delivery systems favours their internalization by target cells as well as their transfection efficiency (191).

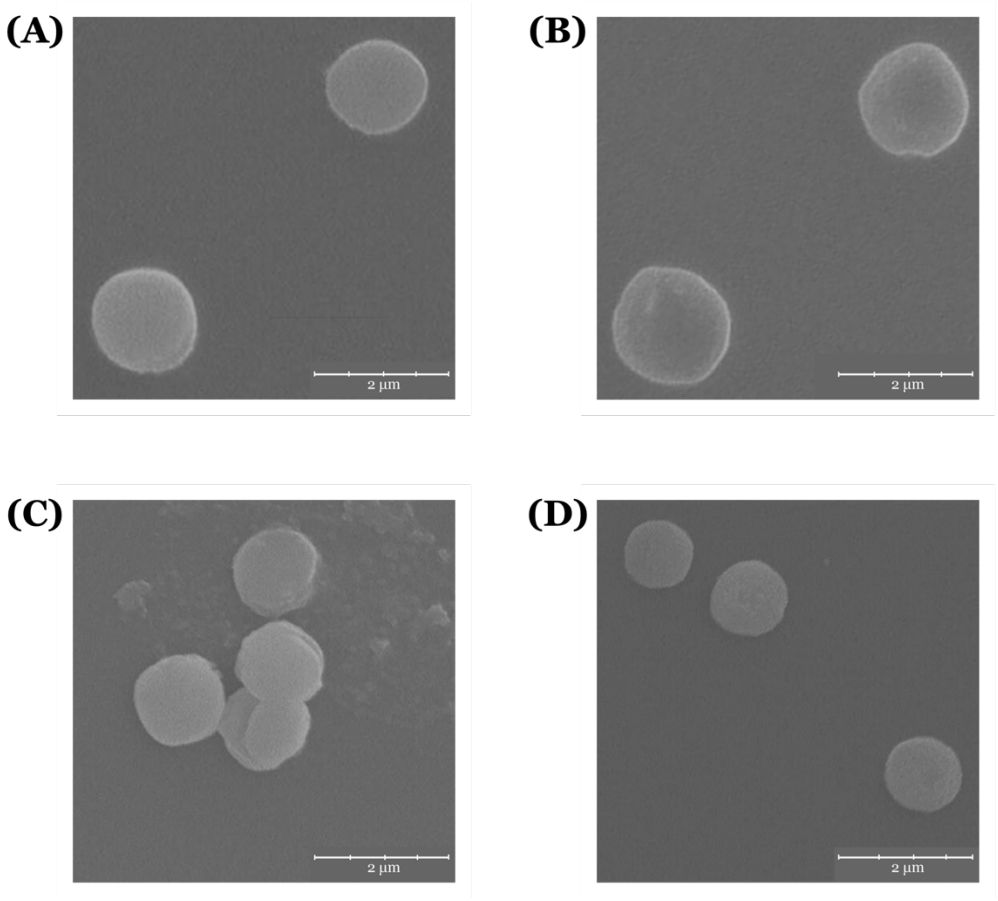

Figure 24 - Scanning electron micrographs of ChNPs with R8 and R8-mannose: (A) HMW-TPP/R8/PP, (B) HMW-TPP/R8-man/PP, (C) 5 kDa-TPP/R8/PP, (D) 5 kDa-TPP/R8-man/PP.

4.2.4.Stability assays

Stability studies of NPs allow the evaluation of their capacity to condense and protect DNA during *in vitro* and *in vivo* applications. In this way, after formulation, the four systems selected were resuspended in 60 µL of trypsin, simple medium or medium supplemented with 10 % FBS and 1 % penicillin-streptomycin. The stability of free PP was also evaluated under the same conditions as those indicated for evaluated systems. The media used were DMEM-F12 (for FibH) and MEM-α (for JAWSii). Subsequently, samples were incubated at 37 °C for 0, 3 and 6h. At each set hour, 20 µL were removed and their stability was assessed by 1% agarose gel electrophoresis.

As it can be seen in **Figure 25**, ChNPs remain stable over time, with no DNA presence in the agarose gel between 0 and 6 h. This behavior is observed when both trypsin, simple medium and supplemented medium were applied. Even in the presence of FBS, the systems are not destabilized, showing good resilience of the ChNPs. In the runs corresponding to the supplemented medium, in **Figure 25** (A - lane C; lane 3; lane 6), (B - lane C; lane 3; lane 6), (C - lane 3; lane 5), the band observed is related to the supplementation of the medium with FBS, since when only medium is injected, the same band is observed.

Thus, it can be stated that ChNPs have the ability to protect and condense DNA, which will allow and facilitate their delivery for *in vitro* and *in vivo* assays. Even in the presence of FBS, ChNPs remain resilient as no pDNA bands are identified on the electrophoresis gel. So, ChNPs are good systems to protect, condense, transport and deliver pDNA to target cells. The same results were described by Rodolfo *et al.* (182).

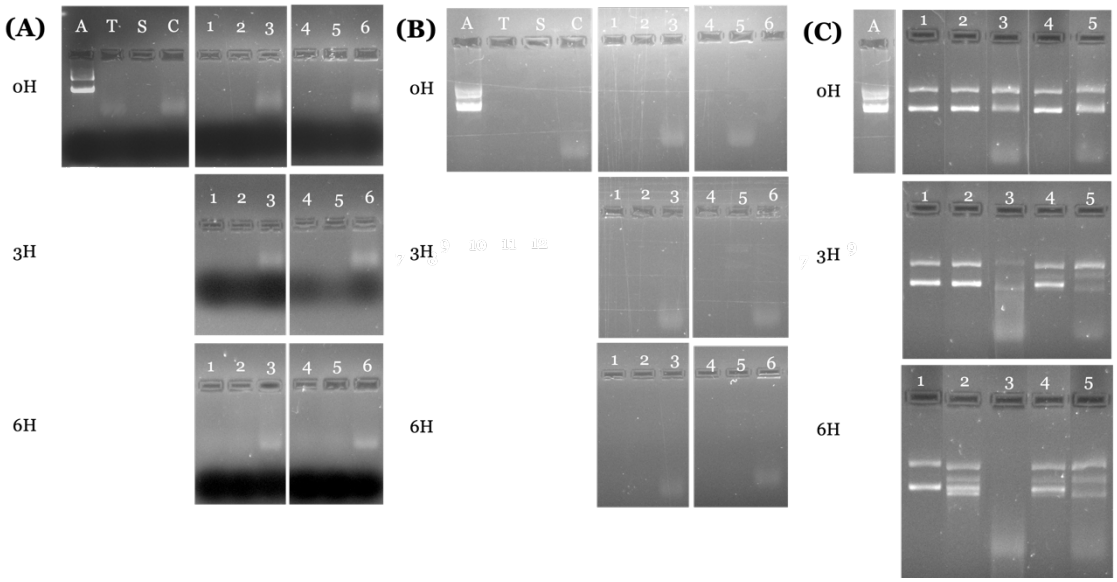

Figure 25 – Analysis of nanoparticles' stability in cellular simple medium by agarose gel electrophoresis. **(A)** assays performed with DMEM-F12 medium; **(B)** assays performed with MEM-α medium; **(T)** trypsin, **(S)** simple medium, **(C)** supplemented medium, this pattern being repeated all 3 lanes. **(A)** PP initial sample**;** lanes **(1)** to **(3)** HMW/ TPP/ R8-mannose; lanes **(4)** to **(6)** 5 kDa/ TPP/ R8-mannose. **(C)** assays performed with free PP: Lane **(1)** - trypsin, Lane **(2)** – simple MEM-α medium, Lane **(3)** - supplemented MEM-α medium, Lane **(4)** – simples DMEM-F12 medium, Lane **(5)** - supplemented DMEM-F12 medium.

4.3. *In vitro* transfection studies

4.3.1. Viability assay

Cellular cytotoxicity is an important parameter to be investigated when considering the application of a delivery system for gene transfection. If a system presents toxicity, it may compromise its use for cellular transfection.

To determine the biocompatibility of the studied ChNPs, an MTT assay was performed on FibH and JAWS II cells-at 24 and 48 h. The results of the MTT assay on both cell lines are presented in **Figure 26**.

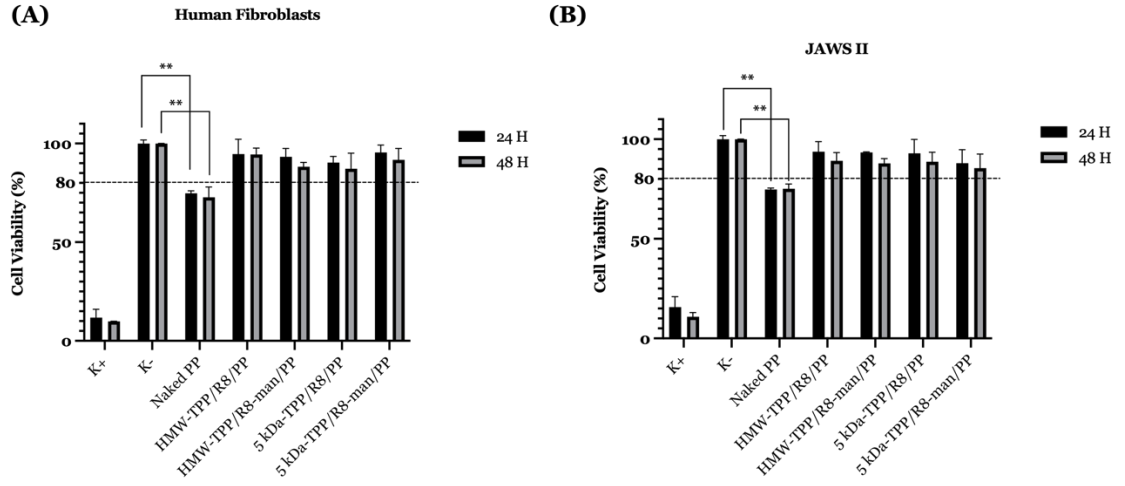

Figure 26 – Cellular viability of human fibroblasts and JAWSII cells at 24 and 48 h after transfection with the different Ch/TPP/R8 and Ch/TPP/R8-mannose systems and naked PP. Cells treated with 70% ethanol were used as positive control (K+) and non-transfected cells were used as negative control (K–). The percent cell viability is expressed relative to the negative control. Data obtained from three in-dependent measurements (mean ± S.D., n = 2). Statistical analysis was performed using "one-way ANOVA" (** $p < 0.01$).

Observing **Figure 26**, in FibH, HMW systems showed a cell viability between 93 and 94% and 5 kDa systems between 90 and 95%. In JAWS II cells, when HMW systems were applied viability was around 93% and in 5 kDa systems viability ranged between 87 and 92%. It is possible to observe that none of the nanoparticles are cytotoxic to the cells. Both HMW and 5 kDa systems functionalized with R8 or R8-mannose showed a cell viability higher than 80%, following the trend described in another assay with Ch systems (192). Considering naked PP, it reduced viability in both cell lines, with obtained values ranging between 72 and 74%. Thus, it is possible to state that Ch-based systems allow delivery of PP, while protecting it and avoiding toxic effects to the cells. HMW-TPP/PP and 5 kDa-TPP/PP binary systems have been studied elsewhere, in which the biocompatibility of the systems compared to naked PP delivery was verified (182).

4.3.2. Transfection efficiency

The cellular uptake and internalization of HMW and 5 kDa systems after 4 h transfection was assessed by fluorescence confocal microscopy. The images are shown in **Figure 27** and **Figure 28**. The nucleus was labeled with DAPI, showing blue staining, while the green represents FITC-labeled PP. The control presented in **Figure 27** and **Figure 28** corresponds to untransfected cells and displays no green fluorescence signals.

According to **Figure 27** and **Figure 28**, it is possible to observe that formulations with R8 and R8-mannose have a superior capacity to overcome the cell membrane and enter the

cytoplasm of the cells compared to the binary system. Cells transfected with ternary systems, both with R8 and R8-mannose, show evidence of the ability to overcome extracellular and intracellular barriers, since they reveal the ability to penetrate the cell membrane, to be internalized by the cell and to localize in the nucleus. Once inside the nucleus, transcription and expression of the target gene is expected to proceed. The entry of these systems into cells can be explained by the presence of R8 mannose, in particular CPP R8, which has been described as responsible for efficiently increasing cellular entry, internalization and accumulation of the target molecule in the nucleus (149,193). In addition to the presence of R8, systems with mannose exhibit greater internalization than systems with R8 alone, as there is a specific interaction of mannose and APCs receptors (194).

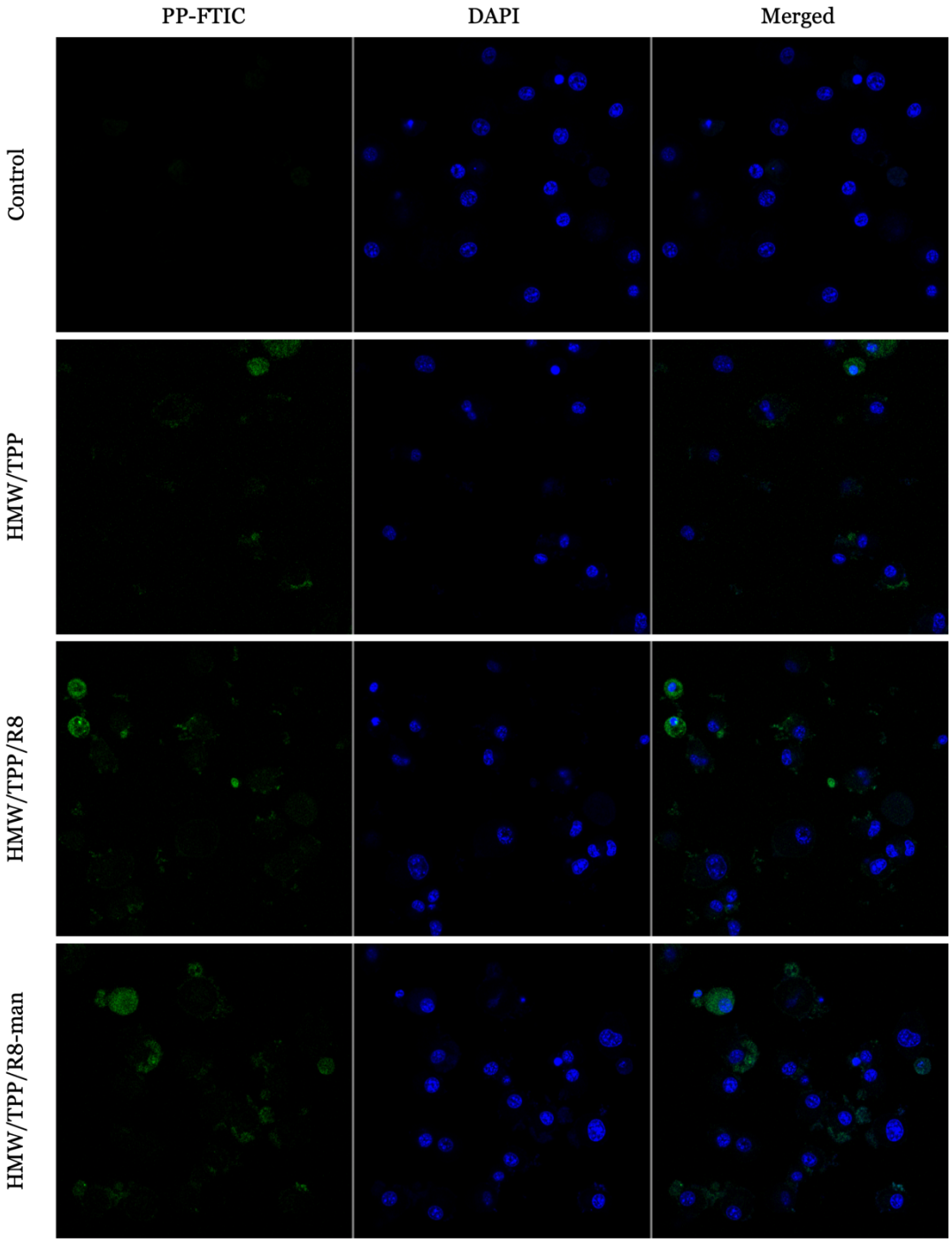

Figure 27 - Evaluation of the transfection capacity of HMW-TPP/PP, HMW-TPP/R8/PP and HMW-TPP/R8-man/PP. Nuclei were stained blue by DAPI and green represents FITC-stained PP. The control is untransfected JAWS II.

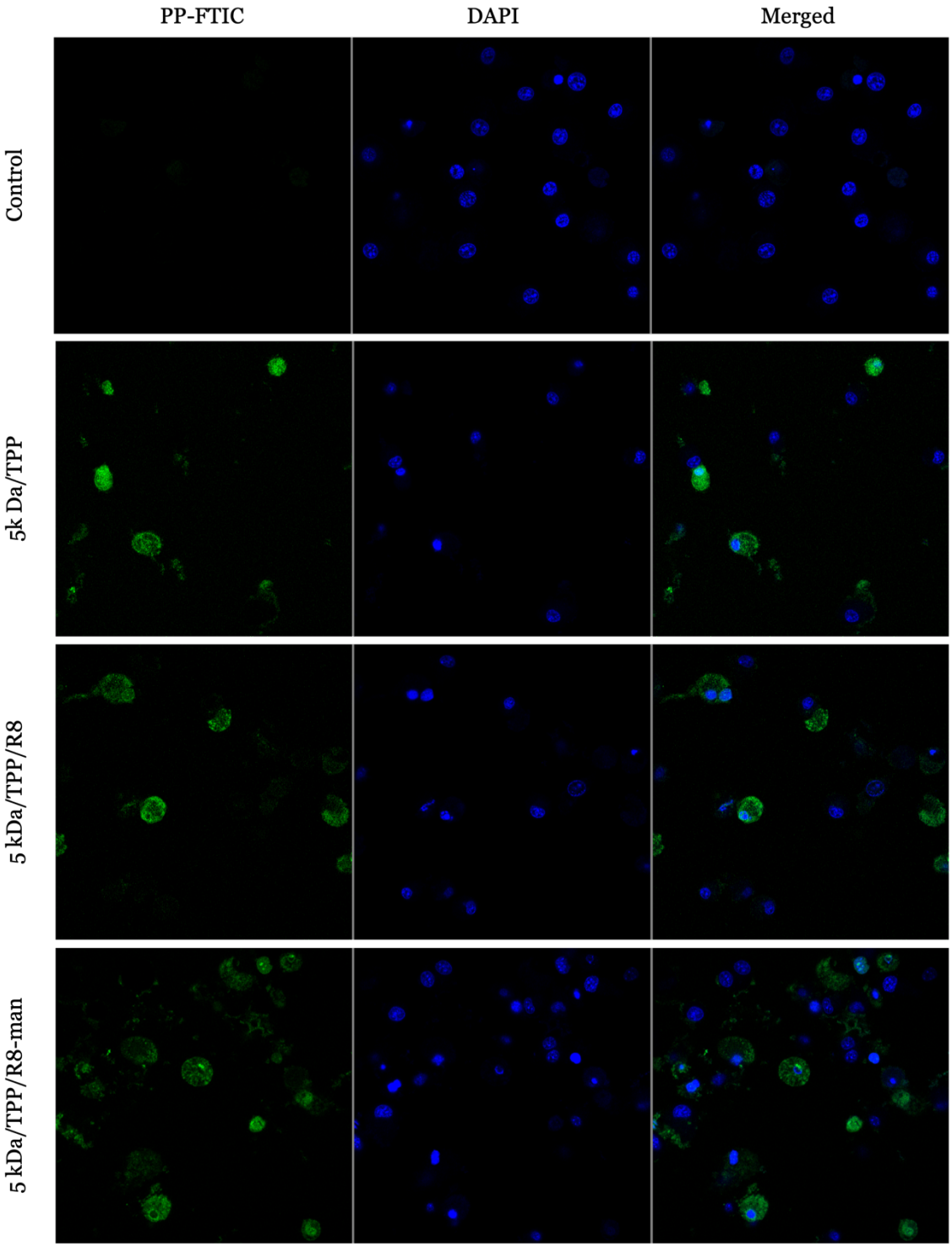

Figure 28 - Evaluation of the transfection capacity of 5 kDa-TPP/PP, 5 kDa-TPP/R8/PP and 5 kDa-TPP/R8-man/PP. Nuclei were stained blue by DAPI and green represents FITC-stained PP. The control is non-transfected JAWS II.

To verify the confocal microscopy results, the evaluation of the fluorescence intensity inside JAWS II cells 4 h after internalization of Ch systems was performed (**Figure 29**). Non-transfected cells (CT) had shown residual fluorescence that was removed from the fluorescence analysis of the systems. Observing **Figure 29**, for the HMW systems, the TPP-only system did not show significant fluorescence, demonstrating that they are not very efficient systems for cellular transfection purposes. When functionalized with R8 or R8-

mannose, the systems show an increase in fluorescence but not higher than the binary system. Compared with the 5 kDa systems, these present high fluorescence values. Focusing on the binary system, it shows a good internalization, and very similar to the systems with R8. But when compared with the mannose functionalized systems, they overcame in internalization efficiency, since they present the highest fluorescence intensity of all systems under study. Therefore, we can imply that the most promising system for gene transfection into target cells will be the 5 kDa-TPP/R8-man/PP system.

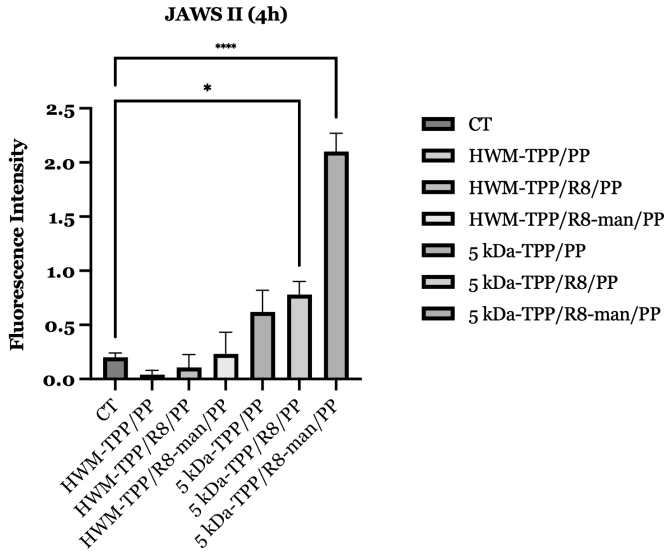

Figure 29 - Fluorescence intensity of JAWS II cells after 4 h of internalization with the different delivery systems.

Chapter 5

Conclusion and Future Prospects

The times we live in have shown the importance of research and the relevance of the development of new approaches to combat new adversities, such as the SARS-CoV-2 pandemic. With the approval of the first RNA vaccine against COVID-19, the world of nucleic acid vaccines has been greatly boosted, given the potential presented by this technology. DNA vaccines have been widely explored as they have the ability to stimulate both the cellular and humoral components of the immune system. However, the main challenge for their clinical application are the biological barriers that make it impossible to stimulate immune responses, thus reducing their therapeutic efficacy.

In this work, a new PP vector for encoding the RBD gene as well as new delivery systems were developed with the aim of preventing and/or treating SARS-CoV-2 infections. After performing 17 experimental conditions, it was possible to establish the most favorable condition and strategy for the recombination of PP into mcDNA, as well as the maximization of its obtaining through scale up to mini bioreactor. Thus, the optimal condition implies the use of 42 °C for fermentation and 30 °C for induction, for 1 h without antibiotic. It was also possible to realize that performing a centrifugation step between fermentation and induction allowed eliminating the fermentation TB medium that had negative effects on mcDNA yield. When these conditions were passed to the bioreactor, the pO_2 that best favored PP yield was applying 60% for 5h and 30% pO_2 for induction, applying 0.01% L-arabinose for 5h.

The ternary systems, HMW-TPP/R8/PP, HMW-TPP/R8-man/PP, 5 kDa-TPP/R8/PP and 5 kDa-TPP/R8-man/PP, were developed and compared with previously studied binary systems, HMW-TPP/PP and 5 kDa-TPP/PP. These systems exhibit adequate characteristics concerning size, PDI, surface charge and morphology, that make them suitable for delivery systems as they have small sizes, positive surface charge, spherical morphology and the ability to encapsulate PP and mcDNA. Regarding stability studies, after incubation with simple medium, supplemented medium and trypsin, all systems under study were able to efficiently condense and protect DNA. When the biocompatibility of systems was evaluated, the cell viability rates were all higher than 80% demonstrating that the systems are biocompatible.

Upon evaluation of confocal microscopy assays, systems without and with R8 or R8-mannose were monitored to understand their influence on target cell recognition and internalization. It was possible to determine that the 5 kDa-TPP/R8-man/PP systems show a higher internalization capacity, being able to transport the DNA into the cells.

The results obtained in this work are very promising and contribute to the evolution of DNA vaccines against possible pandemics. To improve the robustness of these results, it would be interesting to carry out a RT-PCR and real time PCR assays to assess the ability of the systems to

deliver and express the RBD gene, as well to perform Western Blot assays to compare the performance of the systems under study and the correct expression of antigen.

Data from this study open perspectives for the continuation of the research on this topic, suggesting *in vivo* studies; for instance, vaccinating healthy mice to investigate the activation of the immune system by determining the levels of RBD-specific T and B cells to confirm the strong activation of both components of the immune system.

The biotechnology area has contributed greatly to the development and research of new vaccines that are safe and effective. The use of new antigens, adjuvants, vectors, and delivery systems are some of the examples reported on the advancement of this technology. With therapeutic vaccines, new doors will be opened and new possibilities for cures can be implemented. Although the challenge is great, reality may be closer, and the impact will certainly be positive in the fight against new pandemics.

Chapter 6

References

1. Chakraborty C, Sharma AR, Sharma G, Bhattacharya M, Lee SS. SARS-CoV-2 causing pneumonia-associated respiratory disorder (COVID-19): Diagnostic and proposed therapeutic options. Eur Rev Med Pharmacol Sci. 2020;24(7):4016–26.
2. Wang Y, Wang Y, Chen Y, Qin Q. Unique epidemiological and clinical features of the emerging 2019 novel coronavirus pneumonia (COVID-19) implicate special control measures. J Med Virol. 2020;92(6):568–76.
3. Wang D, Hu B, Hu C, Zhu F, Liu X, Zhang J, et al. Clinical Characteristics of 138 Hospitalized Patients with 2019 Novel Coronavirus-Infected Pneumonia in Wuhan, China. JAMA - J Am Med Assoc. 2020;323(11):1061–9.
4. Hui DS, I Azhar E, Madani TA, Ntoumi F, Kock R, Dar O, et al. The continuing 2019-nCoV epidemic threat of novel coronaviruses to global health — The latest 2019 novel coronavirus outbreak in Wuhan, China. Int J Infect Dis. 2020;91(2020):264–6.
5. Wang C, Horby PW, Hayden FG, Gao GF. A novel coronavirus outbreak of global health concern. Lancet. 2020;395(10223):470–3.
6. Chen N, Zhou M, Dong X, Qu J, Gong F, Han Y, et al. Epidemiological and clinical characteristics of 99 cases of 2019 novel coronavirus pneumonia in Wuhan, China: a descriptive study. Lancet. 2020;395(10223):507–13.
7. Coronavirus World Map: Tracking the Global Outbreak. The New York Times. 2022 [cited 2022 May 20].
8. Ganesh B, Rajakumar T, Malathi M, Manikandan N, Nagaraj J, Santhakumar A, et al. Epidemiology and pathobiology of SARS-CoV-2 (COVID-19) in comparison with SARS, MERS: An updated overview of current knowledge and future perspectives. Clin Epidemiol Glob Heal. 2021;10(December 2020):100694.
9. Yin Y, Wunderink RG. MERS, SARS and other coronaviruses as causes of pneumonia. Respirology. 2018;23(2):130–7.
10. Zhou P, Yang X Lou, Wang XG, Hu B, Zhang L, Zhang W, et al. A pneumonia outbreak associated with a new coronavirus of probable bat origin. Nature. 2020;579(7798):270–3.
11. Hulswit RJG, de Haan CAM, Bosch BJ. Coronavirus Spike Protein and Tropism Changes. 1st ed. Vol. 96, Advances in Virus Research. Elsevier Inc.; 2016. 29–57 p.
12. Malik YA. Properties of Coronavirus and SARS-CoV-2. 2020;42(1):3–11.
13. Ceraolo C, Giorgi FM. Genomic variance of the 2019-nCoV coronavirus. J Med Virol. 2020;(February):1–7.
14. Du L, He Y, Zhou Y, Liu S, Zheng BJ, Jiang S. The spike protein of SARS-CoV - A target for vaccine and therapeutic development. Nat Rev Microbiol. 2009;7(3):226–36.
15. Shang J, Ye G, Shi K, Wan Y, Luo C, Aihara H, et al. Structural basis of receptor recognition by SARS-CoV-2. Nature. 2020;581(May).
16. Li W, Zhang C, Kuhn JH, Moore MJ, Luo S, Wong S, et al. Receptor and viral determinants

of SARS-coronavirus adaptation to human ACE2. 2005;24(8):1634–43.
17. Mittal A, Manjunath K, Ranjan RK, Kaushik S, Kumar S, Verma V. COVID-19 pandemic: Insights into structure, function, and hACE2 receptor recognition by SARS-CoV-2. PLoS Pathog. 2020;16(8):e1008762.
18. Chu H, Chan JF-W, Yuen TT-T, Shuai H, Yuan S, Wang Y, et al. Comparative tropism, replication kinetics, and cell damage profiling of SARS-CoV-2 and SARS-CoV with implications for clinical manifestations, transmissibility, and laboratory studies of COVID-19: an observational study. The Lancet Microbe. 2020;1(1):e14–23.
19. Bakhiet M, Taurin S. SARS-CoV-2: Targeted managements and vaccine development. Cytokine Growth Factor Rev. 2021;58(December 2020):16–29.
20. Monteil V, Kwon H, Prado P, Hagelkrüys A, Wimmer RA, Stahl M, et al. Inhibition of SARS-CoV-2 Infections in Engineered Human Tissues Using Clinical-Grade Soluble Human ACE2. Cell. 2020;181(4):905-913.e7.
21. Zou X, Chen K, Zou J, Han P, Hao J, Han Z. Single-cell RNA-seq data analysis on the receptor ACE2 expression reveals the potential risk of different human organs vulnerable to 2019-nCoV infection. Front Med. 2020;14(2):185–92.
22. Sungnak W, Huang N, Bécavin C, Berg M, Queen R, Litvinukova M, et al. SARS-CoV-2 entry factors are highly expressed in nasal epithelial cells together with innate immune genes. Nat Med. 2020;26(5):681–7.
23. Shang J, Wan Y, Luo C, Ye G, Geng Q, Auerbach A, et al. Cell entry mechanisms of SARS-CoV-2. Proc Natl Acad Sci U S A. 2020;117(21).
24. Evans JP, Liu S-L. Role of host factors in SARS-CoV-2 entry. J Biol Chem. 2021;100847.
25. Sami I, Bashir Y, Alshaer W, Ismail S. Biochimie SARS-CoV-2 entry in host cells-multiple targets for treatment and prevention. Biochimie. 2020;175:93–8.
26. Walls AC, Park YJ, Tortorici MA, Wall A, McGuire AT, Veesler D. Structure, Function, and Antigenicity of the SARS-CoV-2 Spike Glycoprotein. Cell. 2020;181(2):281-292.e6.
27. Wrapp D, Wang N, Corbett KS, Goldsmith JA, Hsieh CL, Abiona O, et al. Cryo-EM structure of the 2019-nCoV spike in the prefusion conformation. Science (80-). 2020;367(6483):1260–3.
28. Li T, Huang T, Guo C, Wang A, Shi X, Mo X, et al. Genomic variation, origin tracing, and vaccine development of SARS-CoV-2: A systematic review. Innov. 2021;2(2):100116.
29. Florindo HF, Kleiner R, Vaskovich-Koubi D, Acúrcio RC, Carreira B, Yeini E, et al. Immune-mediated approaches against COVID-19. Nat Nanotechnol. 2020;15(8):630–45.
30. Sette A, Crotty S. Adaptive immunity to SARS-CoV-2 and COVID-19. Cell. 2021;1–20.
31. András Zóka GB. COVID-19 and the human innate immune system. Cell Press. 2021;(April):1671–92.
32. Blanco-Melo D, Nilsson-Payant BE, Liu WC, Uhl S, Hoagland D, Møller R, et al. Imbalanced Host Response to SARS-CoV-2 Drives Development of COVID-19. Cell. 2020;181(5):1036-1045.e9.
33. Kuri-Cervantes L, Pampena MB, Meng W, Rosenfeld AM, Ittner CAG, Weisman AR, et al. Comprehensive mapping of immune perturbations associated with severe COVID-19. Sci

Immunol. 2020;5(49).
34. Wang X, Cao R, Zhang H, Liu J, Xu M, Hu H, et al. The anti-influenza virus drug, arbidol is an efficient inhibitor of SARS-CoV-2 in vitro. Cell Discov. 2020;6(1):4–8.
35. Vankadari N. Arbidol: A potential antiviral drug for the treatment of SARS-CoV-2 by blocking trimerization of the spike glycoprotein. Int J Antimicrob Agents. 2020;56(2):105998.
36. Wang Z, Yang B, Li Q, Wen L, Zhang R. Clinical features of 69 cases with coronavirus disease 2019 in Wuhan, China. Clin Infect Dis. 2020;71(15):769–77.
37. Zoufaly A, Poglitsch M, Aberle JH, Hoepler W, Seitz T, Traugott M, et al. Human recombinant soluble ACE2 in severe COVID-19. Lancet Respir Med. 2020;8(11):1154–8.
38. Wang M, Cao R, Zhang L, Yang X, Liu J, Xu M, et al. Remdesivir and chloroquine effectively inhibit the recently emerged novel coronavirus (2019-nCoV) in vitro. Cell Res. 2020;30(3):269–71.
39. Meyerowitz EA, Vannier AGL, Friesen MGN, Schoenfeld S, Gelfand JA, Callahan M V., et al. Rethinking the role of hydroxychloroquine in the treatment of COVID-19. FASEB J. 2020;34(5):6027–37.
40. Choy KT, Wong AYL, Kaewpreedee P, Sia SF, Chen D, Hui KPY, et al. Remdesivir, lopinavir, emetine, and homoharringtonine inhibit SARS-CoV-2 replication in vitro. Antiviral Res 2020;178(March):104786.
41. Şimşek Yavuz S, Ünal S. Antiviral treatment of covid-19. Turkish J Med Sci. 2020;50(SI-1):611–9.
42. Samudrala PK, Kumar P, Choudhary K, Thakur N, Wadekar GS, Dayaramani R, et al. Virology, pathogenesis, diagnosis and in-line treatment of COVID-19. Eur J Pharmacol. 2020;883(May):173375.
43. Shrestha DB, Budhathoki P, Khadka S, Shah PB, Pokharel N, Rashmi P. Favipiravir versus other antiviral or standard of care for COVID-19 treatment: a rapid systematic review and meta-analysis. Virol J. 2020;17(1):141.
44. Wang Y, Zhang D, Du G, Du R, Zhao J, Jin Y, et al. Remdesivir in adults with severe COVID-19: a randomised, double-blind, placebo-controlled, multicentre trial. Lancet. 2020;395(10236):1569–78.
45. COVID-19 Vaccine Tracker. [cited 2022 May 25]. Available from: https://covid19.trackvaccines.org
46. Burrell CJ, Howard CR, Murphy FA, Burrell CJ, Howard CR, Murphy FA. Chapter 11 – Vaccines and Vaccination. In: Fenner and White's Medical Virology. 2017. p. 155–67.
47. Ganneru B, Jogdand H, Daram VK, Das D, Molugu NR, Prasad SD, et al. Th1 skewed immune response of whole virion inactivated SARS CoV 2 vaccine and its safety evaluation. iScience. 2021;24(4):102298.
48. Xia S, Zhang Y, Wang Y, Wang H, Yang Y, Gao GF, et al. Safety and immunogenicity of an inactivated SARS-CoV-2 vaccine, BBIBP-CorV: a randomised, double-blind, placebo-controlled, phase 1/2 trial. Lancet Infect Dis. 2021;21(1):39–51.
49. Zhang Y, Zeng G, Pan H, Li C, Kan B, Hu Y, et al. Immunogenicity and Safety of a SARS-

CoV-2 Inactivated Vaccine in Healthy Adults Aged 18-59 years: Report of the Randomized, Double-blind, and Placebo-controlled Phase 2 Clinical Trial. 2020.

50. Poland GA, Ovsyannikova IG, Crooke SN, Kennedy RB. SARS-CoV-2 Vaccine Development: Current Status. Mayo Clin Proc. 2020;95(10):2172–88.
51. Vartak A, Sucheck SJ. Recent advances in subunit vaccine carriers. Vaccines. 2016;4(2):1–18.
52. Keech C, Albert G, Cho I, Robertson A, Reed P, Neal S, et al. Phase 1–2 Trial of a SARS-CoV-2 Recombinant Spike Protein Nanoparticle Vaccine. N Engl J Med. 2020;383(24):2320–32.
53. Toback S, Galiza E, Cosgrove C, Galloway J, Goodman AL, et al. Safety, immunogenicity, and efficacy of a COVID-19 vaccine (NVX-CoV2373) co-administered with seasonal influenza vaccines: an exploratory substudy of a randomised, observer-blinded, placebo-controlled, phase 3 trial. Lancet Respir Med. 20222;10(2):167–179.
54. Teng Z, Sun S, Luo X, Zhang Z, Seo H, Xu X, et al. Bi-functional gold nanocages enhance specific immunological responses of foot-and-mouth disease virus-like particles vaccine as a carrier and adjuvant. Nanomedicine Nanotechnology, Biol Med. 2021;33:102358.
55. Wang C, Zheng X, Gai W, Wong G, Wang H, Jin H, et al. Novel chimeric virus-like particles vaccine displaying MERS-CoV receptor-binding domain induce specific humoral and cellular immune response in mice. Antiviral Res. 2017;140(January):55–61.
56. Ward BJ, Gobeil P, Séguin A, Atkins J, Boulay I, Charbonneau PY, et al. Phase 1 randomized trial of a plant-derived virus-like particle vaccine for COVID-19. Nat Med. 2021;27(6):1071–8.
57. Makarkov AI, Vasconcellos E, Pillet S, Riera F, Saxena P, Wolff PG, et al. Efficacy and Safety of a Recombinant Plant-Based Adjuvanted Covid-19 Vaccine. N Engl J Med. 2022;1–13.
58. Borah P, Deb PK, Al-Shar'i NA, Dahabiyeh LA, Venugopala KN, Singh V, et al. Perspectives on RNA Vaccine Candidates for COVID-19. Front Mol Biosci. 2021;8(March):1–18.
59. Hadj Hassine I. Covid-19 vaccines and variants of concern: A review. Rev Med Virol. 2021;(October):1–16.
60. Sadoff J, Le Gars M, Shukarev G, Heerwegh D, Truyers C, de Groot AM, et al. Interim Results of a Phase 1–2a Trial of Ad26.COV2.S Covid-19 Vaccine. N Engl J Med. 2021;384(19):1824–35.
61. Sadoff J, Gray G, Vandebosch A, Cárdenas V, Shukarev G, Grinsztejn B, et al. Final Analysis of Efficacy and Safety of Single-Dose Ad26.COV2.S. N Engl J Med. 2022;386(9):847–60.
62. Flaxman A, Marchevsky NG, Jenkin D, Aboagye J, Aley PK, Angus B, et al. Reactogenicity and immunogenicity after a late second dose or a third dose of ChAdOx1 nCoV-19 in the UK: a substudy of two randomised controlled trials (COV001 and COV002). Lancet. 2021;398(10304):981–90.
63. Falsey AR, Sobieszczyk ME, Hirsch I, Sproule S, Robb ML, Corey L, et al. Phase 3 Safety and Efficacy of AZD1222 (ChAdOx1 nCoV-19) Covid-19 Vaccine. N Engl J Med.

2021;385(25):2348–60.
64. Silveira MM, Moreira GMSG, Mendonça M. DNA vaccines against COVID-19: Perspectives and challenges. Life Sci. 2021;267(December 2020):118919.
65. Sahin U, Muik A, Derhovanessian E, Vogler I, Kranz LM, Vormehr M, et al. COVID-19 vaccine BNT162b1 elicits human antibody and TH1 T cell responses. Nature. 2020;586(7830):594–9.
66. Mulligan MJ, Lyke KE, Kitchin N, Absalon J, Gurtman A, Lockhart S, et al. Phase I/II study of COVID-19 RNA vaccine BNT162b1 in adults. Nature. 2020;586(7830):589–93.
67. Walsh EE, Frenck R, Falsey AR, Kitchin N, Absalon J, Gurtman A, et al. RNA-Based COVID-19 Vaccine BNT162b2 Selected for a Pivotal Efficacy Study. medRxiv Prepr Serv Heal Sci. 2020.
68. Hsieh C, Goldsmith JA, Schaub JM, Divenere AM, Kuo H, Javanmardi K, et al. Structure-based design of prefusion-stabilized SARS-CoV-2 spikes. 2020;1505(September):1501–5.
69. Jackson LA, Anderson EJ, Rouphael NG, Roberts PC, Makhene M, Coler RN, et al. An mRNA Vaccine against SARS-CoV-2 — Preliminary Report. N Engl J Med. 2020;383(20):1920–31.
70. Chalkias S, Schwartz H, Nestorova B, Feng J, Chang Y, et al. Safety and Immunogenicity of a 100 μg mRNA-1273 Vaccine Booster for Severe Acute Respiratory Syndrome Coronavirus-2 (SARS-CoV-2). 2022.
71. Foged C, Sundblad A, Hovgaard L. Targeting Vaccines to Dendritic Cells. 2002;19(3):1–3.
72. Khobragade A, Bhate S, Ramaiah V, Deshpande S, Giri K, Phophle H, et al. Efficacy, safety, and immunogenicity of the DNA SARS-CoV-2 vaccine (ZyCoV-D): the interim efficacy results of a phase 3, randomised, double-blind, placebo-controlled study in India. Lancet. 2022;399(10332):1313–21.
73. Shi B, Zheng M, Tao W, Chung R, Jin D, Ghaffari D, et al. Challenges in DNA Delivery and Recent Advances in Multifunctional Polymeric DNA Delivery Systems. Biomacromolecules. 2017;18(8):2231–46.
74. Hobernik D, Bros M. DNA vaccines—How far from clinical use? Int J Mol Sci. 2018;19(11):1–28.
75. Blum JS, Wearsch PA, Cresswell P. Pathways of Antigen Processing. 2013;31:443–73.
76. Hoffmann M, Kleine-Weber H, Schroeder S, Krüger N, Herrler T, Erichsen S, et al. SARS-CoV-2 Cell Entry Depends on ACE2 and TMPRSS2 and Is Blocked by a Clinically Proven Protease Inhibitor. Cell. 2020;181(2):271-280.e8.
77. Daniel AR, Jan EF, Nebesky M. A Review of Recent Advances Using Tocilizumab in the Treatment of Rheumatic Diseases TOCILIZUMAB : THE FIRST. Rheumatol Ther. 2018;5(1):21–42.
78. Guaraldi G, Meschiari M, Cozzi-lepri A, Milic J, Tonelli R, Menozzi M, et al. Tocilizumab in patients with severe COVID-19: a retrospective cohort study. Lancet Rheumatol. 2020;9913(20):1–11.
79. Castelli V, Cimini A, Ferri C. Cytokine Storm in COVID-19: “When You Come Out of the Storm, You Won’t Be the Same Person Who Walked in.” Front Immunol.

2020;11(September):8–11.
80. Horby P, Lim WS, Emberson J, Mafham M, Bell J, Linsell L, et al. Effect of dexamethasone in hospitalized patients with COVID-19 – Preliminary report. N Engl J Med. 2020;
81. Annamaria P, Eugenia Q, Paolo S. Anti-SARS-CoV-2 hyperimmune plasma workflow. Transfus Apher Sci. 2020;59(5).
82. Joyner MJ, Bruno KA, Klassen SA, Kunze KL, Johnson PW, Lesser ER, et al. Safety Update: COVID-19 Convalescent Plasma in 20,000 Hospitalized Patients. Mayo Clin Proc. 2020;95(9):1888–97.
83. Chen P, Nirula A, Heller B, Gottlieb RL, Boscia J, Morris J, et al. SARS-CoV-2 Neutralizing Antibody LY-CoV555 in Outpatients with Covid-19. N Engl J Med. 2021;384(3):229–37.
84. Zost SJ, Gilchuk P, Case JB, Binshtein E, Chen RE, Nkolola JP, et al. Potently neutralizing and protective human antibodies against SARS-CoV-2. Nature. 2020;584(7821):443–9.
85. Ghanem A, Healey R, Adly FG. Current trends in separation of plasmid DNA vaccines: A review. Anal Chim Acta. 2013;760:1–15.
86. Abdulrahman A, Ghanem A. Recent advances in chromatographic purification of plasmid DNA for gene therapy and DNA vaccines: A review. Anal Chim Acta. 2018;1025:41–57.
87. Ghaffarifar F. Plasmid DNA vaccines: Where are we now? Drugs of Today. 2018;54(5):315–33.
88. Han Y, Liu S, Ho J, Danquah MK, Forde GM. Using DNA as a drug-Bioprocessing and delivery strategies. Chem Eng Res Des. 2009;87(3):343–8.
89. Schleef M. Downstream processing of plasmid DNA. Plasmids Ther Vaccin. 2001;18(September):p 208-214 ST-Downstream processing of plasmid D.
90. Santos T, Pereira P, Queiroz JA, Cruz C, Sousa F. Plasmid production and purification: An integrated experiment-based biochemistry and biotechnology laboratory course. Biochem Mol Biol Educ. 2019;47(6):638–43.
91. Prather KJ, Sagar S, Murphy J, Chartrain M. Industrial scale production of plasmid DNA for vaccine and gene therapy: Plasmid design, production, and purification. Enzyme Microb Technol. 2003;33(7):865–83.
92. Rosano GL, Morales ES, Ceccarelli EA. New tools for recombinant protein production in Escherichia coli: A 5-year update. Protein Sci. 2019;28(8):1412–22.
93. Stadler J, Lemmens R, Nyhammar T. Plasmid DNA purification. J Gene Med. 2004;6(SUPPL. 1):54–66.
94. Ghanem A, Healey R, Adly FG, Galindo J, Barrón BL, Lara AR, et al. Vaccine process technology. Biotechnol Bioeng. 2013;116(3):1337–42.
95. Sousa F, Passarinha L, Queiroz JA. Biomedical application of plasmid DNA in gene therapy: A new challenge for chromatography. Biotechnol Genet Eng Rev. 2009;26(1):83–116.
96. Diogo MM, Queiroz JA, Prazeres DMF. Chromatography of plasmid DNA. J Chromatogr A. 2005;1069(1):3–22.
97. Mairhofer J, Grabherr R. Rational vector design for efficient non-viral gene delivery: Challenges facing the use of plasmid DNA. Mol Biotechnol. 2008;39(2):97–104.

98. Ata-abadi NS, Rezaei N, Dormiani K, Nasr-esfahani MH. Production of Minicircle DNA Vectors Using Site-Specific Recombinases. Vol. 1642. 2017. 325–339 p.
99. Diamantino T, Pereira P, Queiroz JA, Sousa Â, Sousa F. Minicircle DNA purification using a CIM® DEAE-1 monolithic support. J Sep Sci. 2016;39(18):3544–9.
100. Gaspar V, De Melo-Diogo D, Costa E, Moreira A, Queiroz J, Pichon C, et al. Minicircle DNA vectors for gene therapy: Advances and applications. Expert Opin Biol Ther. 2015;15(3):1–27.
101. Kay MA, He CY, Chen ZY. A robust system for production of minicircle DNA vectors. Nat Biotechnol. 2010;28(12):1287–9.
102. Gaspar VM, Maia CJ, Queiroz JA, Pichon C, Correia IJ, Sousa F. Improved minicircle DNA biosynthesis for gene therapy applications. Hum Gene Ther Methods. 2014;25(2):93–105.
103. Almeida AM, Queiroz JA, Sousa F, Sousa A. Minicircle DNA purification: Performance of chromatographic monoliths bearing lysine and cadaverine ligands. J Chromatogr B Anal Technol Biomed Life Sci. 2019;1118–1119(November):7–16.
104. Mayrhofer P, Blaesen M, Shleef M, Jechlinger W. Minicircle-DNA production by site specific recombination and protein–DNA interaction chromatography. J Gene Med. 2008;10:1253–69.
105. Hou XH, Guo XY, Chen Y, He CY, Chen ZY. Increasing the minicircle DNA purity using an enhanced triplex DNA technology to eliminate DNA contaminants. Mol Ther - Methods Clin Dev. 2015;2(1):1–6.
106. Alves CPA, Šimčíková M, Brito L, Monteiro GA, Prazeres DMF. Development of a nicking endonuclease-assisted method for the purification of minicircles. J Chromatogr A. 2016;1443:136–44.
107. Almeida AM, Eusébio D, Queiroz JA, Sousa F, Sousa A. The use of size-exclusion chromatography in the isolation of supercoiled minicircle DNA from Escherichia coli lysate. J Chromatogr A. 2020;1609.
108. Alves CPA, Prazeres DMF, Monteiro GA. Minicircle Biopharmaceuticals–An Overview of Purification Strategies. Front Chem Eng. 2021;2(January):1–15.
109. Almeida AM, Černigoj U, Queiroz JA, Sousa F, Sousa A. Quality assessment of supercoiled minicircle DNA by cadaverine-modified analytical chromatographic monolith. J Pharm Biomed Anal. 2020;180(December).
110. Kafshdooz T, Kafshdooz L, Akbarzadeh A, Hanifehpour Y, Joo SW. Applications of nanoparticle systems in gene delivery and gene therapy. Artif Cells, Nanomedicine, Biotechnol. 2016;44(2):581–7.
111. Suschak JJ, Williams JA, Schmaljohn CS. Advancements in DNA vaccine vectors, non-mechanical delivery methods, and molecular adjuvants to increase immunogenicity. Hum Vaccines Immunother. 2017;13(12):2837–48.
112. Lundstrom K. Viral vectors for COVID-19 vaccine development. Viruses. 2021;13(2).
113. Ura T, Okuda K, Shimada M. Developments in viral vector-based vaccines. Vaccines. 2014;2(3):624–41.
114. Chang J. Adenovirus vectors: Excellent tools for vaccine development. Immune Netw.

2021;21(1):1–11.
115. Perry C, Rayat ACME. Lentiviral vector bioprocessing. Viruses. 2021;13(2):1–46.
116. Rauch S, Jasny E, Schmidt KE, Petsch B. New vaccine technologies to combat outbreak situations. Front Immunol. 2018;9(SEP).
117. Scher G, Schnell MJ. Rhabdoviruses as vectors for vaccines and therapeutics. Curr Opin Virol. 2020;44:169–82.
118. Lundstrom K. Plasmid DNA-based alphavirus vaccines. Vaccines. 2019;7(1).
119. Yin H, Kanasty RL, Eltoukhy AA, Vegas AJ, Dorkin JR, Anderson DG. Non-viral vectors for gene-based therapy. Nat Rev Genet. 2014;15(8):541–55.
120. Ibraheem D, Elaissari A, Fessi H. Gene therapy and DNA delivery systems. Int J Pharm. 2014;459(1–2):70–83.
121. Kotnik T, Rems L, Tarek M, Miklavcic D. Membrane Electroporation and Electropermeabilization: Mechanisms and Models. Annu Rev Biophys. 2019;48:63–91.
122. Paston SJ, Brentville VA, Symonds P, Durrant LG. Cancer Vaccines, Adjuvants, and Delivery Systems. Front Immunol. 2021;12:1–21.
123. Slivac I, Guay D, Mangion M, Champeil J, Gaillet B. Non-viral nucleic acid delivery methods. Expert Opin Biol Ther. 2017;17(1):105–18.
124. Sharma D, Arora S, Singh J, Layek B. A review of the tortuous path of nonviral gene delivery and recent progress. Int J Biol Macromol. 2021;183:2055–73.
125. Sizikov AA, Kharlamova M V., Nikitin MP, Nikitin PI, Kolychev EL. Nonviral locally injected magnetic vectors for in vivo gene delivery: A review of studies on magnetofection. Nanomaterials. 2021;11(5):1–17.
126. Ponti F, Campolungo M, Melchiori C, Bono N, Candiani G. Cationic lipids for gene delivery: many players, one goal. Chem Phys Lipids. 2021;235:105032.
127. Samal SK, Dash M, Vlierberghe S Van, Kaplan DL, Chiellini E, Blitterswijk C van, et al. Cationic polymers and their therapeutic potential. Chem Soc Rev. 2012;41(21):7147–94.
128. Farshbaf M, Davaran S, Zarebkohan A, Annabi N, Akbarzadeh A, Salehi R. Significant role of cationic polymers in drug delivery systems. Artif Cells, Nanomedicine Biotechnol. 2018;46(8):1872–91.
129. Karlsson J, Rhodes KR, Green JJ, Tzeng SY. Poly(beta-amino ester)s as gene delivery vehicles: challenges and opportunities. 2021;17(10):1395–410.
130. Mao S, Sun W, Kissel T. Chitosan-based formulations for delivery of DNA and siRNA. Adv Drug Deliv Rev. 2010;62(1):12–27.
131. Imani R, Emami SH, Faghihi S. Synthesis and characterization of an octaarginine functionalized graphene oxide nano-carrier for gene delivery applications. Phys Chem Chem Phys. 2015;17(9):6328–39.
132. Rizeq BR, Younes NN, Rasool K, Nasrallah GK. Synthesis, bioapplications, and toxicity evaluation of chitosan-based nanoparticles. Int J Mol Sci. 2019;20(22).
133. Mehrabi M, Montazeri H, Dounighi MN, Rashti A, Vakili-Ghartavol R. Chitosan-based nanoparticles in mucosal vaccine delivery. Arch Razi Inst. 2018;73(3):165–76.
134. Chuan D, Jin T, Fan R, Zhou L, Guo G. Chitosan for gene delivery: Methods for

improvement and applications. Adv Colloid Interface Sci. 2019;268:25–38.
135. Boroumand H, Badie F, Mazaheri S, Seyedi ZS, Nahand JS, Nejati M, et al. Chitosan-Based Nanoparticles Against Viral Infections. Front Cell Infect Microbiol. 2021;11(March):1–22.
136. Bravo-Anaya LM, Fernández-Solís KG, Rosselgong J, Nano-Rodríguez JLE, Carvajal F, Rinaudo M. Chitosan-DNA polyelectrolyte complex: Influence of chitosan characteristics and mechanism of complex formation. Int J Biol Macromol. 2019;126:1037–49.
137. Bowey K, Neufeld RJ. Systemic and mucosal delivery of drugs within polymeric microparticles produced by spray drying. BioDrugs. 2010;24(6):359–77.
138. Jhaveri J, Raichura Z, Khan T, Momin M, Omri A. Chitosan nanoparticles-insight into properties, functionalization and applications in drug delivery and theranostics. Molecules. 2021;26(2).
139. NAGPAL K, SINGH SK, MISHRA DN. Chitosan Nanoparticles: A Promising System in Novel Drug Delivery. 2010;58(11):1423–30.
140. Yang R, Li H, Huang M, Yang H, Li A. A review on chitosan-based flocculants and their applications in water treatment. Water Res. 2016;95(2015):59–89.
141. Zhao D, Yu S, Sun B, Gao S, Guo S, Zhao K. Biomedical applications of chitosan and its derivative nanoparticles. Polymers (Basel). 2018;10(4).
142. Langel Ü. Cell-penetrating peptides and transportan. Vol. 13, Pharmaceutics. 2021. 1–31 p.
143. Yokoo H, Oba M, Uchida S. Cell-Penetrating Peptides: Emerging Tools for mRNA Delivery. Pharmaceutics. 2022;14(1):1–13.
144. Böhmová E, Machová D, Pechar M, Pola R, Venclíková K, Janoušková O, et al. Cell-penetrating peptides: A useful tool for the delivery of various cargoes into cells. Physiol Res. 2018;67:s267–79.
145. Neves AR, Sousa A, Faria R, Albuquerque T, Queiroz JA, Costa D. Cancer gene therapy mediated by RALA/plasmid DNA vectors: Nitrogen to phosphate groups ratio (N/P) as a tool for tunable transfection efficiency and apoptosis. Colloids Surfaces B Biointerfaces. 2020;185:110610.
146. Serra AS, Eusébio D, Neves AR, Albuquerque T, Bhatt H, Biswas S, et al. Synthesis and Characterization of Mannosylated Formulations to Deliver a Minicircle DNA Vaccine. Pharmaceutics. 2021;13(5):673.
147. Borrelli A, Tornesello AL, Tornesello ML, Buonaguro FM. Cell penetrating peptides as molecular carriers for anti-cancer agents. Molecules. 2018;23(2).
148. Zhang X, Wang H, Coulter JA, Yang R. Octaarginine-modified gold nanoparticles enhance the radiosensitivity of human colorectal cancer cell line LS180 to megavoltage radiation. Int J Nanomedicine. 2018;13:3541–52.
149. Biswas S, Dodwadkar NS, Deshpande PP, Parab S, Torchilin VP. Surface functionalization of doxorubicin-loaded liposomes with octa-arginine for enhanced anticancer activity. Eur J Pharm Biopharm. 2013;84(3):711-517–25.
150. Koshkaryev A, Piroyan A, Torchilin VP. Bleomycin in Octaarginine-modified Fusogenic Liposomes Results in Improved Tumor Growth Inhibition. Cancer Lett.

2013;334(2):51293–301.
151. Ruseska I, Zimmer A. Internalization mechanisms of cell-penetrating peptides. Beilstein J Nanotechnol. 2020;11:101–23.
152. Futaki S. Membrane-permeable arginine-rich peptides and the translocation mechanisms. Adv Drug Deliv Rev. 2005;57(4 SPEC.ISS.):547–58.
153. Gao Y, Xu Z, Chen S, Gu W, Chen L, Li Y. Arginine-chitosan/DNA self-assemble nanoparticles for gene delivery: In vitro characteristics and transfection efficiency. Int J Pharm. 2008;359(1–2):241–6.
154. Mishra N, Pant P, Porwal A, Jaiswal J, Aquib M. Targeted drug delivery: a review. Am J Pharm Tech Res. 2016;6(1):1–24.
155. Daftarian P, Serafini P, Perez V. APC-Targeted (DNA) Vaccine Delivery Platforms: Nanoparticle Aided. Molecular Vaccines: From Prophylaxis to Therapy - Volume 2. 2014. 753–766 p.
156. Irache JM, Salman HH, Gamazo C, Espuelas S. Mannose-targeted systems for the delivery of therapeutics. Expert Opin Drug Deliv. 2008;5(6):703–24.
157. Apostolopoulos V, Thalhammer T, Tzakos AG, Stojanovska L. Targeting Antigens to Dendritic Cell Receptors for Vaccine Development. J Drug Deliv. 2013;1–22.
158. Hossain MK, Wall KA. Use of dendritic cell receptors as targets for enhancing anti-cancer immune responses. Cancers (Basel). 2019;11(3).
159. Hibbert DB. Experimental design in chromatography : A tutorial review. J Chromatogr B. 2012;910:2–13.
160. Montgomery DC. Design and Analysis of Experiments, Eight Edition.
161. J.L. Myers, A. Well RFL. Research Design and Statistical Analysis. 3rd Ed. Routledge, editor. New York, NY; 2010.
162. Valente JFA, Sousa A, Queiroz JA, Sousa F. DoE to improve supercoiled p53-pDNA purification by O-phospho-L-tyrosine chromatography. J Chromatogr B. 2019;1105:184–92.
163. Hocharoen L, Noppiboon S, Kitsubun P. Toward QbD Process Understanding on DNA Vaccine Purification Using Design of Experiment. Front Bioeng Biotechnol. 2021;9:1–10.
164. Ben Ali R, Ben Ouada S, Leboulanger C, Ammar J, Sayadi S, Ben Ouada H. Bisphenol A removal by the Chlorophyta Picocystis sp.: optimization and kinetic study. Int J Phytoremediation. 2021;23(8):818–28.
165. Ferreira SLC, Bruns RE, da Silva EGP, dos Santos WNL, Quintella CM, David JM, et al. Statistical designs and response surface techniques for the optimization of chromatographic systems. J Chromatogr A. 2007;1158(1–2):2–14.
166. Inoue H, Nojima H, Okayama H. High efficiency transformation of Escherichia coli with plasmids. Gene. 1990;96(1):23–8.
167. Pedro AQ, Oppolzer D, Bonifácio MJ, Maia CJ, Queiroz JA, Passarinha LA. Evaluation of MutS and Mut+ Pichia pastoris Strains for Membrane-Bound Catechol-O-Methyltransferase Biosynthesis. Appl Biochem Biotechnol. 2015;175(8):3840–55.
168. Chang CW, Christensen L V., Lee M, Kim SW. Efficient expression of vascular endothelial

growth factor using minicircle DNA for angiogenic gene therapy. J Control Release. 2008;125(2):155–63.

169. Eusébio D, Almeida AM, Alves JM, Maia CJ, Queiroz JA, Sousa F, et al. The Performance of Minicircle DNA Versus Parental Plasmid in p53 Gene Delivery into HPV-18-Infected Cervical Cancer Cells. Nucleic Acid Ther. 2020;31(1):1–10.
170. Wong EM, Muesing MA, Polisky B. Temperature-sensitive copy number mutants of ColE1 are located in an untranslated region of the plasmid genome. Proc Natl Acad Sci U S A. 1982;79(11 I):3570–4.
171. Carnes AE, Hodgson CP, Williams JA. Inducible Escherichia coli fermentation for increased plasmid DNA production. Biotechnol Appl Biochem. 2006;45(3):155–66.
172. Simcikova M, Prather KLJ, Prazeres DMF, Monteiro GA. On the dual effect of glucose during production of pBAD/AraC-based minicircles. Vaccine. 2014;32(24):2843–6.
173. Chen ZY, He CY, Kay MA. Improved production and purification of minicircle DNA vector free of plasmid bacterial sequences and capable of persistent transgene expression in vivo. Hum Gene Ther. 2005;16(1):126–31.
174. Eriksson, L.; Johansson, E.; Kettaneh-Wold, N.; WikstrÄom C. Design of Experiments, Principles and Applications. J Chemom. 2001;15(5):495–6.
175. Hou XH, Guo XY, Chen Y, He CY, Chen ZY. Increasing the minicircle DNA purity using an enhanced triplex DNA technology to eliminate DNA contaminants. Mol Ther - Methods Clin Dev. 2015;2:14062.
176. Islas-Lugo F, Vega-Estrada J, Alvis CA, Ortega-López J, del Carmen Montes-Horcasitas M. Developing strategies to increase plasmid DNA production in Escherichia coli DH5α using batch culture. J Biotechnol. 2016;233:66–73.
177. Gonçalves GAL, Prather KLJ, Monteiro GA, Carnes AE, Prazeres DMF. Plasmid DNA production with Escherichia coli GALG20, a pgi-gene knockout strain: Fermentation strategies and impact on downstream processing. J Biotechnol. 2014;186:119–27.
178. Borja GM, Meza Mora E, Barrón B, Gosset G, Ramírez OT, Lara AR. Engineering Escherichia coli to increase plasmid DNA production in high cell-density cultivations in batch mode. Microb Cell Fact. 2012;11(40):1–9.
179. Krishna Rao D V., Ramu CT, Rao J V., Narasu ML, Bhujanga Rao AKS. Impact of dissolved oxygen concentration on some key parameters and production of rhG-CSF in batch fermentation. J Ind Microbiol Biotechnol. 2008;35(9):991–1000.
180. Passarinha, L.A., Diogo, M.M., Queiroz, J.A., Monteiro, G.A., Fonseca, L.P., Prazeres DM. Production of ColE1 type plasmid by Escherichia coli DH5α cultured under nonselective conditions. J Microbiol Biotechnol. 2006;16(1):20–4.
181. Guzman LM, Belin D, Carson MJ, Beckwith J. Tight regulation, modulation, and high-level expression by vectors containing the arabinose P(BAD) promoter. J Bacteriol. 1995;177(14):4121–30.
182. Rodolfo C, Eusébio D, Ventura C, Nunes R, Florindo HF, Costa D, et al. Design of Experiments to Achieve an Efficient Chitosan-Based DNA Vaccine Delivery System. Pharmaceutics. 2021 Aug 31;13(9):1369.

183. Zhao X, Li Z, Liu W, Luk KDK, Lu WW. Octaarginine-modified chitosan as a nonviral gene delivery vector : properties and in vitro transfection efficiency. J Nanopart Res. 2011;13:693–702.
184. Albuquerque T, Faria R, Sousa Â, Neves AR, Queiroz JA, Costa D. Polymer-peptide ternary systems as a tool to improve the properties of plasmid DNA vectors in gene delivery. J Mol Liq. 2020;309.
185. Ibrahim YHEY, Regdon G, Kristó K, Kelemen A, Adam ME, Hamedelniel EI, et al. Design and characterization of chitosan/citrate films as carrier for oral macromolecule delivery. Eur J Pharm Sci. 2020;146:105270.
186. Tomaz AF, de Carvalho SMS, Barbosa RC, Silva SML, Gutierrez MAS, de Lima AGB, et al. Ionically crosslinked chitosan membranes used as drug carriers for cancer therapy application. Materials. 2018;11(10):1–18.
187. Loutfy SA, Salaheldin TA, Ramadan MA, Farroh KY, Abdallah ZF, Eloahed TYA. Synthesis, characterization and cytotoxic evaluation of graphene oxide nanosheets: In vitro liver cancer model. Asian Pacific J Cancer Prev. 2017;18(4):955–61.
188. Costa A, Sarmento B, Seabra V. Mannose-functionalized solid lipid nanoparticles are effective in targeting alveolar macrophages. Eur J Pharm Sci. 2018;114:103–13.
189. Hora D. D-Mannose-Modified Iron Oxide Nanoparticles for Stem Cell Labeling. 2007;
190. Ahmed MES, Mohamed HM, Mohamed MI, Kandile NG. Sustainable antimicrobial modified chitosan and its nanoparticles hydrogels: Synthesis and characterization. Int J Biol Macromol. 2020;162:1388–97.
191. Gaspar VM, Sousa F, Queiroz JA, Correia IJ. Formulation of chitosan-TPP-pDNA nanocapsules for gene therapy Applications. Nanotechnology. 2011;22(1).
192. Rodolfo C, Eusébio D, Ventura C, Nunes R, Florindo HF, Costa D, et al. Design of experiments to achieve an efficient chitosan-based DNA vaccine delivery system. Pharmaceutics. 2021;13(9).
193. Conniot J, Scomparin A, Peres C, Yeini E, Pozzi S, Matos AI, et al. Immunization with mannosylated nanovaccines and inhibition of the immune-suppressing microenvironment sensitizes melanoma to immune checkpoint modulators. Nat Nanotechnol. 2019;14(9):891–901.
194. Xing L, Fan YT, Zhou TJ, Gong JH, Cui LH, Cho KH, et al. Chemical modification of Chitosan for efficient vaccine delivery. Molecules. 2018;23(2).
195. Özbaş-turan S, Akbuğa J. Plasmid DNA-loaded chitosan / TPP nanoparticles. Drug Deliv. 2011;18(3):215–22.